Observations of Turbulence and Mixing in the Southeastern Beaufort Sea

by

Benjamin Scheifele

M.Sc., The University of British Columbia, 2013

B.Sc. Physics, St. Francis Xavier University, 2011

A THESIS SUBMITTED IN PARTIAL FULFILLMENT
OF THE REQUIREMENTS FOR THE DEGREE OF

Doctor of Philosophy

in

THE FACULTY OF GRADUATE AND POSTDOCTORAL STUDIES
(Oceanography)

The University of British Columbia
(Vancouver)

February 2020

The following individuals certify that they have read, and recommend to the Faculty of Graduate and Postdoctoral Studies for acceptance, the thesis entitled:

Observations of Turbulence and Mixing in the Southeastern Beaufort Sea

submitted by **Benjamin Scheifele** in partial fulfillment of the requirements for the degree of **Doctor of Philosophy** in **Oceanography**.

Examining Committee:

Stephanie Waterman, University of British Columbia
Supervisor

Susan Allen, University of British Columbia
Supervisory Committee Member

Greg Lawrence
University Examiner

Phil Austin
University Examiner

Ilker Fer, University of Bergen
External Examiner

Additional Supervisory Committee Members:

Jeff Carpenter, Helmholtz Zentrum Geesthacht
Supervisory Committee Member

Bernard Laval, University of British Columbia
Supervisory Committee Member

Abstract

In this thesis, I use a novel set of hydrography and turbulence measurements from the southeastern Beaufort Sea to

i. compare estimates of the turbulent kinetic energy dissipation rate, ε, obtained independently from shear and temperature microstructure measurements;

ii. characterize turbulence and mixing in the Amundsen Gulf region of the southeastern Beaufort Sea; and

iii. describe the characteristics of tracer diffusion in an oceanic flow as it transitions between fully turbulent and nearly-laminar.

I collected the measurements over 10 days in 2015 using an ocean glider measuring temperature, conductivity, and pressure on O(10)-cm scales and shear and temperature on O(1)-mm turbulent scales.

The two independent ε estimates agree within a factor of 2 when ε exceeds 3×10^{-11} W kg^{-1}, but diverge by up to two orders of magnitude at smaller values. I identify the noise floor of the shear measurements as the primary reason for this divergence and, therefore, suggest that microstructure temperature measurements are preferable for estimating ε in low energy environments like the Beaufort Sea.

I find that turbulence is typically weak in Amundsen Gulf: ε has a geometric mean value of 2.8×10^{-11} W kg^{-1} and is less than 1×10^{-10} W kg^{-1} in 68% of observations. Turbulent dissipation varies over five orders of magnitude, is bottom enhanced, and is primarily modulated by the M2 tide. Stratification is strong and frequently damps turbulence, inhibiting diapycnal mixing in up to 93% of observations. However, a small number of strongly turbulent mixing events disproportionately drive net buoyancy fluxes. Heat fluxes are modest and nearly always below 1 W m^{-2}.

Finally, I use the turbulence measurements to demonstrate how tracer diffusion in the ocean transitions continuously between turbulent diffusion and near-molecular diffusion as turbulence weakens and stratification strengthens. I use the buoyancy Reynolds

number, Re_B, to quantify the relative energetic contributions of potential and kinetic energy to the flow dynamics and find that present models for tracer diffusion are accurate to within a factor of 3 when $Re_B > 10$. However, contrary to expectations, I find that significant enhanced tracer diffusivity at turbulent scales remains present when Re_B is below unity.

Lay Summary

This thesis outlines my research about ocean turbulence and the impacts it has on the Canadian sector of the Arctic Ocean. Turbulence is a fluid dynamics phenomenon that is ubiquitous throughout the world's oceans and helps to control their ability to support life by supplying heat, oxygen, and nutrients to ocean organisms. The distributions of these characteristics are particularly important in the Arctic Ocean because modern climate change is quickly driving Arctic ecosystems towards states never seen before in human history. Understanding these changes and making predictions about what the region will be like in future generations relies on a careful understanding of how turbulence modulates the ocean environment. This thesis describes original, previously unpublished research on how to measure ocean turbulence, how it impacts the physical environment in a region of the Beaufort Sea, and on the physical characteristics of turbulent fluid flow in the Arctic Ocean.

Preface

This thesis presents original research that was designed and conducted by me. I defined the research questions, planned and executed the experiment, analyzed the data, and wrote the thesis and the journal articles mentioned in the next paragraph to report the results. The work was, however, also a collaborative effort, and my PhD advisors Drs. Stephanie Waterman and Jeff Carpenter actively contributed with advice at every stage of the project, from the initial definition of the problem to the final writing of the papers and thesis. My use of the pronoun "we" throughout the document reflects this collaboration.

This thesis is written in "paper format". While I wrote it as a record of a single, cohesive research project, each science chapter (Chapters 2–4) may also be read as a self-contained standalone study, suitable for journal publication. This results in some redundancies from chapter to chapter, but the overlap is small and, in each case, the information provided is there to serve the purpose of that specific study. Chapter 2 is published almost verbatim as a peer-reviewed article in *Journal of Geophysical Research: Oceans*[1]. A version of Chapter 3 is presently undergoing peer review for publication in an academic journal. In both cases, as with the thesis, the research and manuscript preparation were conducted primarily (to about 90%) by me and supported Drs. Stephanie Waterman and Jeff Carpenter. Lucas Merckelbach contributed substantially in the collection of the measurements. I led the peer review process for the submission of the material in Chapter 2. For the material in Chapter 3, the peer review-driven modifications (i.e. those changes requested by reviewers after the initial submission) are being completed by Jeff Carpenter and Stephanie Waterman; these contributions will amount to about 35% of the material in the final re-submitted document.

The project described by this thesis was defined within the broad mandate of the Canadian Arctic GEOTRACES Program, and the field work was conducted in collaboration

[1]B. Scheifele, S. N. Waterman, L. Merckelbach, and J. R. Carpenter. Measuring the Dissipation Rate of Turbulent Kinetic Energy in Strongly Stratified, Low-Energy Environments: A Case Study From the Arctic Ocean. *Journal of Geophysical Research: Oceans*, 19:1817–22, Aug. 2018

with ArcticNet and the Canadian Coast Guard on the GEOTRACES Cruise Leg 15b. Lucas Merckelbach contributed extensively to the design and execution of the field work; he also provided the flight model and scripts to extract the glider data. Rockland Scientific Inc. provided scripts to process the microstructure shear data, which I modified slightly; Barry Ruddick and Jeff Carpenter provided scripts to process the microstructure temperature data, which I modified heavily to suit the purposes of this study.

Table of Contents

Abstract . . . iii

Lay Summary . . . v

Preface . . . vi

Table of Contents . . . viii

List of Tables . . . xi

List of Figures . . . xii

List of Acronyms . . . xx

List of Mathematical Symbols . . . xxii

Acknowledgements . . . xxvi

Dedication . . . xxvii

1 Introduction . . . **1**
- 1.1 Project Overview . . . 1
- 1.2 Research Questions . . . 3
- 1.3 Background . . . 4
  - 1.3.1 Ocean Mixing and Turbulence . . . 4
  - 1.3.2 Turbulence Measurements from Gliders . . . 7
  - 1.3.3 The Dissipation Rate of Turbulent Kinetic Energy . . . 8
  - 1.3.4 Shear Microstructure . . . 9
  - 1.3.5 Temperature Microstructure . . . 10
  - 1.3.6 The Osborn Model for Mixing . . . 11
  - 1.3.7 Amundsen Gulf . . . 12

2 Measuring the Dissipation Rate of Turbulent Kinetic Energy in Strongly Stratified, Low Energy Environments . . . 14
2.1 Motivation . . . 14
2.2 Measurements . . . 16
2.2.1 Measurement Platform: Slocum Glider . . . 16
2.2.2 Shear and Temperature Microstructure . . . 16
2.2.3 Location, Local Hydrography, and Sampling Strategy . . . 17
2.3 Data Processing . . . 19
2.3.1 Glider Velocity Estimates . . . 19
2.3.2 Shear Microstructure . . . 21
2.3.3 Temperature Microstructure . . . 22
2.4 Comparison of Results from Temperature and Shear Microstructure . . . 24
2.4.1 Spatial Cross Sections . . . 24
2.4.2 Mean Vertical Profiles . . . 26
2.4.3 Distributions of ε_U and ε_T . . . 28
2.4.4 One-to-one comparison of ε_U and ε_T . . . 30
2.5 Discussion . . . 31
2.5.1 The Effect of Sensor Limitations . . . 32
2.5.2 Turbulence Spectra in Stratified Low Energy Flows . . . 34
2.5.3 Understanding Uncertainty for Small ε . . . 36
2.5.4 Implications for Interpreting Microstructure Measurements . . . 38
2.6 Conclusions . . . 40

3 Turbulence and Mixing in the Arctic Ocean's Amundsen Gulf . . . 42
3.1 Introduction . . . 42
3.2 Measurements and Data Processing . . . 44
3.2.1 Sampling Strategy . . . 44
3.2.2 Turbulence Measurements and Data Processing . . . 45
3.2.3 Arithmetic vs. Geometric Averaging . . . 47
3.3 Hydrography . . . 47
3.4 Turbulence and Mixing . . . 49
3.4.1 Turbulent Dissipation Rates . . . 49
3.4.2 The Influence of Stratification . . . 53
3.4.3 Diffusivity Estimates . . . 54
3.4.4 Vertical Heat Fluxes . . . 57
3.5 Discussion: Mixing Processes . . . 58
3.5.1 Tidal Mixing . . . 58
3.5.2 Double Diffusion . . . 61
3.5.3 Pacific Water Mesoscale and Smaller Features . . . 62
3.6 Conclusions . . . 64

4 Enhanced Heat Fluxes in a Marginally Turbulent Flow 66
4.1 Introduction 66
4.2 Methods 68
4.2.1 Measurements and ε Estimates 68
4.2.2 Osborn Model 70
4.2.3 Temperature Variance Method: The Osborn-Cox Model 71
4.2.4 Idealized Turbulence: Isotropy 72
4.2.5 Other Diffusivity Models 73
4.2.6 Mixing Efficiency 74
4.3 Results 75
4.3.1 Diffusivity Estimates 75
4.3.2 Mixing Efficiency 77
4.4 Summary and Discussion 79
4.4.1 Enhanced Heat Fluxes 79
4.4.2 Applicability of the Osborn Model 81
4.4.3 Mixing Efficiency in High Stratification 82

5 Conclusion 84
5.1 Goals and Representativeness of the Thesis 84
5.1.1 Observing weak turbulence in strong stratification 85
5.1.2 Turbulent mixing in the Arctic Ocean's Amundsen Gulf 87
5.1.3 Enhanced heat fluxes in strongly stratified, weakly turbulent environments 88
5.2 The Bigger Picture: Looking Ahead 89

Bibliography 92

Appendix 102
A.1 Quality Control Measures for Dissipation Rate Estimates 102
A.2 Comparison of Results from Upcasts and Downcasts 105
A.3 Nasmyth and Batchelor Spectra 106

List of Tables

Table 2.1 Mean $\pm$ one standard deviation of glider-flight variables from all up- and downcasts of the mission. θ is the measured pitch, α_a the estimated angle of attack, γ the estimated glide angle, and $\mathcal{U}$ the estimated speed through water. Only data coincident with at least one viable ε estimate (see Appendix A.1) are included. 20

Table 2.2 Statistical parameters of the ε_U and ε_T distributions shown in Figure 2.5. Given, from left to right, are the number, N, of observations; mode; geometric mean; median; first and third quartiles, P_{25} and P_{75}; arithmetic mean; and geometric standard deviation factor, σ_g. The quantities N and σ_g are dimensionless and unscaled. All other quantities are scaled by a factor of 10^{-11} W kg^{-1}. 29

Table 3.1 Properties of the hydrographic layers. Layers are defined by their absolute salinity, S_A. Ranges given for depth, conservative temperature, T, density anomaly, σ, and stratification, N^2, are for the central 90% of data. The layer labels are SML: Surface Mixed Layer; CH: Cold Halocline; PW: Pacific Water Layer; WH: Warm Halocline; AW: Atlantic Water Layer. 48

Table 3.2 Select statistics of ε and K_ρ observed in (top) all the data; (middle) all data except that within the turbulent patch; and (bottom) data only from within the turbulent patch. The turbulent patch is defined as the region inside the white rectangle in Figures 3.4 and 3.7, between $s =$ 52–81 km on the horizontal axis. 52

Table A.1 Quality control parameters, as defined in the text. Percentages are the fraction of measurements flagged by each condition. 102

List of Figures

Figure 1.1 The glider's 10 day path in the Amundsen Gulf along which it measured 348 microstructure profiles in summer 2015. Shown are the start and end points/dates, as well as the location of four intermediate waypoints. The light-blue line indicates approximately the north-eastern boundary beyond which it was unsafe to operate the glider because of the possibility of sea ice. 2

Figure 1.2 (a) Example measured shear spectrum (Φ, black line) with a fitted empirical Nasmyth spectrum (blue line). The upper end of the inertial subrange can be seen to the left of the "viscous rolloff", indicated by the purple shading. Yellow shading indicates the viscous subrange where viscosity begins to remove kinetic energy from the turbulent flow. The Kolmogorov wavenumber is shown by the vertical dashed line. The dissipation rate estimate ε_U is also given (the subscript U indicates a velocity shear-derived estimate). (b) Example measured temperature gradient spectrum (Ψ, black line) with a fitted theoretical Batchelor spectrum (blue line). The dissipation rate estimate ε_T (subscript T indicates a temperature gradient-derived estimate) is indicated. The Batchelor wavenumber is shown by the vertical dashed line. 10

Figure 2.1 (a) The measurement location at the entrance to the Amundsen Gulf in the southeastern Beaufort Sea. The glider path is shown by the line inside the dashed black rectangle. Bathymetry contours are drawn at 1000 m intervals beginning at 200 m. (b) Enlarged view of the area inside the dashed rectangle indicated in panel a, showing the glider path and the local bathymetry. Selected waypoints along the path are numbered consecutively and indicated by squares for reference when reading Figures 2.2 and 2.3. Contours are drawn at 75 m intervals beginning at 50 m. In both panels, colour indicates water depth (m); bathymetry data are from IBCAO 3.0 (Jakobsson et al., 2012). Mean vertical profiles of (c) conservative temperature, (d) in-situ density anomaly, and (e) buoyancy frequency are also shown; these are horizontally averaged over all casts where the glider's maximum dive depth exceeded 325 m. 18

Figure 2.2 Cross sections of the turbulent dissipation rate, ε, in $\log_{10}$ space, derived from microstructure measurements of (a) shear and (b) temperature. The panels are drawn using the same colour scale. Grey shading indicates the bathymetry, black shading discarded or unavailable data (see Section 2.2.3 and the Appendix). Small white lines along the horizontal axis indicate the locations of individual profiles. The breaks in the horizontal axis, labelled 1–4, correspond to the waypoints shown in Figure 2.1b. Magenta rectangles with solid white lines indicate regions of enhanced dissipation discussed in the text. The magenta rectangle with dashed white line in panel (b) indicates the signature of the mesoscale eddy discussed in the text. 25

Figure 2.3 Cross section of the ratio $\varepsilon_U/\varepsilon_T$ in $\log_{10}$ space. Shading, panel division, magenta rectangles, and annotations as in Figure 2.2. 26

Figure 2.4 (a) Average vertical profiles of the dissipation rates ε_U and ε_T, obtained from shear and temperature microstructure and calculated using a trimmed geometric mean in 25 m vertical bins. Shading indicates the 95% confidence interval for the mean as indicated by the geometric standard error. (b) The ratio of the average vertical profiles of ε_U and ε_T, highlighting disagreement by a factor of 5 or greater between 75–175 m depth. 27

Figure 2.5 Histograms showing the distributions of all (a) ε_U and (b) ε_T observations. The interquartile range (IQR) is indicated by the darker shading; the mode, arithmetic and geometric means, and median are marked in both panels according to the legend in (a). The labels N and σ_g indicate the total number of observations in each histogram and the geometric standard deviation factor respectively. Histograms are calculated over 100 logarithmically spaced bins. (c) Quantile-quantile plot demonstrating the goodness of fit of the histograms to idealized lognormal distributions. For each set of data, deciles are marked by grey-shaded circles, and the squared linear correlation coefficient, R^2, is indicated. 28

Figure 2.6 Scatter plot comparison of the two coincident dissipation rate estimates ε_U and ε_T. Identical agreement and agreement within factors of 2 and 5 are indicated as labelled. Bin averages are calculated perpendicular to the one-to-one line (see text). Our empirical estimate of the ε_U noise floor (3×10^{-11} W kg^{-1}) is indicated by the horizontal dotted line. Purple shading indicates where both estimates of ε simultaneously lie above 3×10^{-11} W kg^{-1} and also delineates the region where bin averages agree within a factor of 2. 31

Figure 2.7 Sample coincident shear (a-f: Φ) and temperature gradient (g-l: Ψ) spectra (black) for 6 orders of magnitude of ε, as determined by the temperature measurements. Bold indicates the wavenumbers explicitly included for integration; the remaining variance is estimated as described in Sections 2.3.2 and 2.3.3. For Ψ, bold also indicates the wavenumber range used for the MLE Batchelor fit (see Section 2.3.3).Shear spectra have the accelerometer signal removed (Section 2.3.2) and temperature gradient spectra have the empirically-determined noise spectra removed (Section 2.3.3). Nasmyth (a-f) and Batchelor (g-l) reference spectra (grey) are also drawn. Batchelor spectra are those determined by the MLE fitting algorithm which are used to estimate k_B (Section 2.3.3). 33

Figure 2.8 Median nondimensionalized shear (a-d) and temperature gradient (e-h) spectra in bold, for regimes of Re_B as indicated. Also shown are the 25th and 75 percentile of data (thin solid line) as well as nondimensionalized reference spectra (dashed line): Nasmyth for shear and Batchelor for temperature gradient. The total number of spectra used in each calculation is indicated by N. Shear spectra with $\varepsilon_U < 10^{-10}$ W kg^{-1} are excluded. 35

Figure 2.9 Root-mean-square error between Ψ and Ψ_B, as defined in the text, visualized as a function of (a) buoyancy Reynolds number, and (b) dissipation rate. It quantifies the degree of divergence between observed temperature gradient and theoretical Batchelor spectra. Large open faced markers are bin averages. Regressions to subsets of the bin averages are shown in each panel; the subsets are those on either side of the datum marked by the circle (inclusive). 37

Figure 2.10 Histogram of the ratio $\varepsilon_U/\varepsilon_T$, highlighting the large number of coincident measurements where the shear-derived values overestimated the temperature-derived ones in our dataset. Agreement by factors of 5, 10, and 100 is indicated by dashed lines. The histogram is calculated over 50 logarithmically spaced bins. 38

Figure 3.1 (a) Map of the southeastern Beaufort Sea, showing the location of Amundsen Gulf to the east of the Canadian Beaufort Shelf. The glider path is shown by the thin black line inside the black rectangle. (b) Enlarged view of the region given by the black rectangle in panel (a), showing the path of the glider. The start and end locations of the track are shown by the large white rectangles; four intermediate waypoints are shown by the small white rectangles and numbered consecutively. The color on the glider's track-line is water temperature along the 1026.15 kg m^{-3} isopycnal, using the same colour scale as shown in Figure 3.11, indicating the location and spatial scale of the warm-core eddy discussed in the text (Section 3.5.3). The white circle is the location of ArcticNet mooring CA08. Bathymetry data are from IBCAO 3.0 (Jakobsson et al., 2012). . . 43

Figure 3.2 (a) Arithmetic mean profile and spatial cross section of conservative temperature. (b) Geometric mean profile and spatial cross section of stratification. For the mean profiles, grey shading indicates the range of the central 90% of data; alternating coloured background shading indicates the approximate depth ranges of the hydrographic layers defined in the text (PW, WH, and AW are labelled). For the spatial sections, the horizontal axis is broken and consecutively labelled 1–4 at the waypoints marked in Figure 3.1, indicating where the glider changed direction. White rectangle in (a) indicates the mesoscale eddy discussed in the text. 48

Figure 3.3 Histograms of (a) the turbulent dissipation rate, ε, and (b) the buoyancy Reynolds number, Re_B. For each, the number in the top right indicates the percentage of data that fall within the axis limits; the remaining data are zero-valued and cannot be displayed on a logarithmic axis. The interquartile range for each set, including zero-valued data, is the span between the two dash-dotted lines. For ε, the geometric and arithmetic mean values are also indicated (GM and AM, respectively). For Re_B, the approximate critical value $Re_B^* = 10$ is indicated by the yellow line. 50

Figure 3.4 Mean vertical profiles and horizontal cross sections of (a) ε, and (b) Re_B. Waypoints are indicated as in Figure 3.2. For each, the geometric mean profile is given in 25 m bins (blue); for ε, the arithmetic mean profile is also given (black). In both cross sections, the white rectangle between waypoints 2 and 3 identifies the patch of enhanced turbulence discussed in the text. In the Re_B cross section, red pixels indicate where a turbulent diapycnal flux is expected; grey pixels indicate a predicted absence of turbulent diapycnal mixing. The approximate critical value $Re_B^* = 10$ is indicated in the Re_B mean profile by the vertical yellow line. 52

Figure 3.5 The three repeat ε transects (left vertical axis) over the continental shelf slope. The horizontal axis is the distance from Waypoint 3 shown in Figure 3.1b. Thick lines are 2.5 km geometric mean bin-averages of ε; coloured markers in the background are individual geometric mean cast-averages. The quasi-vertical dash-dotted lines connect peaks and troughs that appear to be stationary between the three ε transects, as discussed in the text. The bathymetry is shown with grey shading in the background (right vertical axis) for reference. 53

Figure 3.6 Histograms of (a) the diapycnal mixing coefficient, K_ρ, of density and (b) the vertical heat flux, F_H. Positive K_ρ indicate down-gradient density diffusion; negative K_ρ indicate up-gradient density diffusion. For F_H, the green shaded area indicates the region between the 5th and 95th percentiles. 55

Figure 3.7 Arithmetic mean vertical profiles, in 25-m bins, and horizontal cross sections of (a) the diapycnal mixing coefficient, K_ρ, of density and (b) the vertical heat flux, F_H. For the cross sections, the horizontal axis, waypoint markers, and white rectangle identifying the turbulent patch are as in Figure 3.4. The K_ρ cross section depicts the absolute value. 56

Figure 3.8 (a) Power density spectrum of ε, constructed using Welch's method and 4 day segments of data. Grey shading indicates the 95% confidence interval. The M2 and inertial frequencies are indicated. (b) The ε time series used to construct the power density spectrum. The series is made from the geometric cast-averages of ε for all depths greater than 100 m and is interpolated to a 15 minute grid. Variability on scales smaller than 2 hours has been removed. 59

Figure 3.9 (a) Depth-averaged current velocity components U and V, measured by ArcticNet mooring CA08 between depths 100–170 m. The grey shading indicates the period of the glider deployment. (b) Power density spectra of the above U and V records, with 95% confidence intervals. (c) Polar histograms with current speeds of the above U and V records, decomposed into high frequency and residual components. High frequencies are defined as those greater than 1.3 cpd and are dominated by the M2 tide. The approximate orientation of the Amundsen Gulf's major axis, azimuth 305°, is indicated in each histogram by the yellow line. The percentage on each histogram's perimeter is the tick label for the radial axis (Relative Occurrence). . 60

Figure 3.10 Geometric mean vertical profile and horizontal cross section of the density ratio, R_ρ. In the cross section, data are discretized into three regimes: susceptible to double diffusion (red: $R_\rho \leq 7$), marginally susceptible (yellow: $7 < R_\rho \leq 10$), and not susceptible (purple: $R_\rho > 10$). The approximate critical value $R_\rho = 10$ is shown in the mean profile by the yellow vertical line. 62

Figure 3.11 (a) An enlarged view of the temperature cross section of the cold halocline and Pacific Water layers, highlighting the eddy as well as smaller, O(1) km, temperature anomalies. The dashed white lines correspond, from left to right, to the three T-S lines shown in the lower three panels. (b) T-S diagrams for the three vertical profiles indicated in the upper panel. Grey dots are all the data shown in the upper panel. Dotted lines are density contours. 63

Figure 4.1 (a) Distribution of Re_B from microstructure data collated in Waterhouse et al. (2014), between the surface mixed layer and 1000 m depth, for the following experiments: Fieberling, NATRE, BBTRE 1996, BBTRE 1997, GRAVILUCK, LADDER, TOTO, DIMES-West, DIMES-DP. (b) Distribution of halocline averaged Re_B from a finescale parameterization of ε using CTD data presented in Chanona et al. (2018). (c) Map showing the locations of the data used in the histograms; red indicates microstructure data presented in Waterhouse et al. (2014), and blue indicates finescale data presented in Chanona et al. (2018). 67

Figure 4.2 Histograms for the measurements used in this study of (a) turbulent dissipation rate, ε, (b) squared buoyancy frequency, N^2, (c) buoyancy Reynolds number, Re_B, and (d) gradient density ratio, R_ρ. There are $\mathrm{N} = 13,190$ data. 69

Figure 4.3 (a) Scatterplot of the nondimensionalized net temperature diffusivity, K_T/κ_T, as a function of buoyancy Reynolds number, Re_B. White symbols indicate mode, arithmetic mean, and geometric mean in logarithmically spaced Re_B bins. Models from Osborn (1980, modified), Shih et al. (2005), and Bouffard and Boegman (2013) are shown for reference, all normalized by κ_T^{mol} to facilitate comparison with K^*. The three red data points are select—but in no way remarkable—points for which the raw temperature microstructure records are shown below. The three turbulence regimes proposed by Ivey et al. (2008)—molecular, transitional, and energetic—are indicated by the background shading—purple, white, and orange, respectively. (b) The ratio of the net temperature diffusivity (Equation 4.6) to the net diffusivity calculated from the modified Osborn model (Equation 4.5). Symbols as in panel a, excepting the arithmetic mean which is omitted here because it is not informative. (c) The microstructure temperature records used to calculate the three select data points (red) in panels a and b. Each record represents 40 s of measurement, spanning an along-path distance Δx, a vertical distance Δz, and a temperature difference ΔT between the first and last measurements. For each 40-s segment of measurement, one temperature gradient spectrum is calculated by averaging spectra from 19 half-overlapping 4-s subsegments (Section 4.2.3). 76

Figure 4.4 (a) Histogram of flux coefficient estimates for the subset of data where $Re_B > 10$. Dash-dotted lines indicate percentiles 5, 25, 75, and 95. The red triangle indicates the canonical value proposed by Osborn (1980). N indicates the number of data points. (b) Flux coefficient plotted as a function of Re_B. Large open-faced symbols are the median and geometric mean values in geometrically-spaced bins. Error bars indicate the geometric standard error in the mean, calculated from two geometric standard deviations. (c) As in panel a, but for mixing efficiency, R_f. (d) As in panel b, but for R_f and with arithmetic mean values and standard errors in place of geometric ones. 78

Figure A.1 Comparison of results from individual (a,b) shear probes and (c,d) temperature probes. Bin averages are calculated as in Figure 2.6. Agreement within a factor of 5 is indicated in all panels by the dashed lines. 104

Figure A.2 Overview of select results, separated by upcast and downcast. For each of ε_U and ε_T, we show the histograms (a,e), averaged vertical profiles (b,f), and selected spectra (c–d,g–h) separated in this manner. The spectra shown are those corresponding to dissipation rates within a factor of 1.1 of 10^{-9} W/kg. Thick black lines depict the median of the selected spectra at each wavenumber. 105

List of Acronyms

AM	Arithmetic mean
AW	Atlantic Water, as in Atlantic Water layer
BB	Diffusivity model proposed by Bouffard and Boegman (2013)
CA08	ArcticNet mooring in central Amundsen Gulf
CH	Cold halocline
CTD	Conductivity-Temperature-Depth profiler
FFT	Fast Fourier Transform
FP07	Fast response microstructure thermistor produced by RSI
GM	Geometric mean
GPS	Global Positioning System
IBCAO	International Bathymetric Chart of the Arctic Ocean
IQR	Interquartile range
ITP	Ice-Tethered Profiler
M2	Principal lunar semi-diurnal tidal constituent
MLE	Maximum Likelihood Estimator
PW	Pacific Water, as in Pacific Water layer
Q-Q	Quantile-quantile, as in quantile-quantile plot
QC	Quality control
RSI	Rockland Scientific International Inc.
SKIF	Diffusivity model proposed by Shih et al. (2005)

SML Surface mixed layer

SPM-38 Microstructure airfoil shear probe produced by RSI

TEOS-10 Thermodynamic Equation of Seawater - 2010

TKE Turbulent Kinetic Energy

List of Mathematical Symbols

Units used in this thesis are given in brackets. These are common to physical oceanography and typically, but not always, comply with the International System of Units.

Glider variables

α_{a}	Angle of attack [°], measured positive upward relative to the glide angle γ
A	Constant in Merckelbach et al. (2010) hydrodynamic flight model
C_{D_1}	Constant in Merckelbach et al. (2010) hydrodynamic flight model
x	Distance coordinate along the glider's path through water [m]
C_{D_0}	Drag coefficient in Merckelbach et al. (2010) hydrodynamic flight model
γ	Estimated glide angle [°], measured positive upward from the horizontal
θ	Glider pitch [°], measured positive upward from the horizontal
$\mathcal{U}$	Glider speed through water along the direction of travel [m s^{-1}]
$\mathcal{W}$	Glider vertical speed through water [m s^{-1}]
s	Horizontal along-track distance coordinate [m]
t	Time coordinate [s]
z	Vertical coordinate [m]

Data Processing

q_B	Batchelor constant in the theoretical Batchelor spectrum [–]
k_B	Batchelor wavenumber [cpm]

Ψ_{B}	Batchelor form for the temperature gradient power spectrum [K^2 cpm]
$\hat{s}$	Calibration constant for shear probes [–]
χ_{obs}	Component of χ obtained by integrating Ψ between k_l and k_u [$\mathrm{K}^2\ \mathrm{m}^{-1}$]
Ψ_{ns}	Empirically determined temperature gradient noise spectrum [K^2 cpm]
Φ_N	Empirical Nasmyth power spectrum for shear variance [$(\mathrm{s}^2\ \mathrm{cpm})^{-1}$]
f	Frequency [Hz]
χ_{hw}	High-wavenumber correction term for χ [$\mathrm{K}^2\ \mathrm{m}^{-1}$]
k_ν	Kolmogorov wavenumber [cpm]
k_l	Lower integration limit in k-space [cpm]
χ_{lw}	Low-wavenumber correction term for χ [$\mathrm{K}^2\ \mathrm{m}^{-1}$]
Φ^*	Nondimensionalized shear power spectrum [–]
Ψ^*	Nondimensionalized temperature gradient power spectrum [–]
$\hat{k}$	Radian wavenumber [m^{-1}], where $\hat{k} = 2\pi k$
Ψ_{r}	Raw, i.e. uncorrected, temperature gradient power spectrum [K^2 cpm]
Φ	Shear power spectrum [$(\mathrm{s}^2\ \mathrm{cpm})^{-1}$]
k_1	Smallest nonzero wavenumber [cpm]
Ψ	Temperature gradient power spectrum [K^2 cpm]
Λ	Temperature power spectrum [$\mathrm{K}^2\ \mathrm{cpm}^{-1}$]
k_u	Upper integration limit in k-space [cpm]
E_p	Voltage across piezoelectric beam in response to trans-axial force [V]
k	Wavenumber [cpm]

Seawater and sea ice properties

S_A	Absolute salinity [$\mathrm{g\ kg}^{-1}$]
N	Buoyancy frequency [s^{-1}]
T	Conservative temperature [°C]

f	Coriolis parameter [s^{-1}]
ρ_i	Density of sea ice [kg m^{-3}]
U	Eastward component of current velocity [m s^{-1}]
β	Haline contraction coefficient of seawater [$(g/kg)^{-1}$]
ν	Kinematic viscosity of seawater [m^2 s^{-1}]; may also be interpreted as the molecular diffusivity of momentum
l_o	Latent heat of melting sea ice [J kg^{-1}]
$\overline{T}_{AW}$	Mean temperature of Atlantic Water layer [°C]
T_o	Melting temperature of sea ice [°C]
V	Northward component of current velocity [m s^{-1}]
σ	Potential density anomaly [kg m^{-3}], defined $\rho - 1000$ kg m^{-3}
ρ	Potential density of seawater [kg m^{-3}]
Pr	Prandtl number (for temperature) [–], equal to $\nu/\kappa_T^{\mathrm{mol}}$
c_p	Specific heat capacity of seawater [J $(kg\ K)^{-1}$]
E	Thermal energy sequestered in the Atlantic Water layer [J m^{-2}]
α	Thermal expansion coefficient of seawater [K^{-1}]

Statistics

σ_g	Geometric standard deviation factor [–]
N	Number of data points [–]
ξ_{rms}	Root-mean-square error [–]
R^2	Squared linear correlation coefficient [–]

Turbulence and Mixing

$\mathcal{B}$	Buoyancy flux [kg m^{-1} s^{-3}]
Re_B	Buoyancy Reynolds number [–], equal to $\varepsilon/\nu N^2$
C	Cox number [–]

Re_B^* Critical value for Buoyancy Reynolds number, $Re_B^* = 10$

χ Dissipation rate of thermal gradient variance [$\mathrm{K^2\ s^{-1}}$]

ε Dissipation rate of turbulent kinetic energy [$\mathrm{W\ kg^{-1}}$ *or* $\mathrm{m^2\ s^{-3}}$]

ε_T Dissipation rate of turbulent kinetic energy estimate derived from temperature microstructure measurements [$\mathrm{W\ kg^{-1}}$]

ε_U Dissipation rate of turbulent kinetic energy estimate derived from velocity shear microstructure measurements [$\mathrm{W\ kg^{-1}}$]

Γ Flux coefficient [–] in the Osborn (1980) model, defined as $R_f/(1-R_f)$

Γ_o Flux coefficient, canonical value, 0.2, from Osborn (1980)

R_f Flux Richardson number [–]; may also be interpreted as the efficiency of turbulent mixing [–]

$R_{f\mathrm{o}}$ Flux Richardson number, canonical value, 0.17, from Osborn (1980)

g Gravitational acceleration [$\mathrm{m\ s^{-2}}$]

R_ρ Gradient density ratio [–], to quantify susceptibility to double diffusion

L_K Kolmogorov length scale [m]

$\kappa_\rho^{\mathbf{mol}}$ Molecular diffusivity of density in seawater [$\mathrm{m^2\ s^{-1}}$]

$\kappa_S^{\mathbf{mol}}$ Molecular diffusivity of salinity in seawater [$\mathrm{m^2\ s^{-1}}$]

$\kappa_T^{\mathbf{mol}}$ Molecular diffusivity of temperature in seawater [$\mathrm{m^2\ s^{-1}}$]

K_ρ Net diffusivity of density [$\mathrm{m^2\ s^{-1}}$]

K_T Net diffusivity of temperature [$\mathrm{m^2\ s^{-1}}$]

K^* Nondimensionalized temperature diffusivity [–]

L_O Ozmidov length scale [m]

$\mathcal{P}$ Production rate of turbulent kinetic energy [$\mathrm{kg\ m^{-1}\ s^{-3}}$]

$\kappa_\rho^{\mathbf{turb}}$ Turbulent diffusivity of density in seawater [$\mathrm{m^2\ s^{-1}}$]

$\kappa_T^{\mathbf{turb}}$ Turbulent diffusivity of temperature in seawater [$\mathrm{m^2\ s^{-1}}$]

u' Turbulent velocity component perpendicular to the direction of travel [$\mathrm{m\ s^{-1}}$]

F_H Vertical heat flux [$\mathrm{W\ m^{-2}}$]

Acknowledgments

An honest and heartfelt thank you to my advisors Stephanie Waterman and Jeff Carpenter for supporting me, believing in me, and guiding me through my PhD. In addition, Professors Susan Allen, Rich Pawlowicz, and Tara Ivanochko have been important role models who helped instil in me a passion for oceanography and for teaching. Thank you also to my friends and fellow grad students in *the Waterhole*; Tara Howatt deserves a special mention for tirelessly listening to me vent about my academic struggles and failures, and for celebrating with me and sharing in my successes.

It goes without saying that I could not be here, at the end of this PhD-road, without the family, friends, and colleagues who walked beside me on the journey. Your generosity, patience, and kindness inspire me. You know who you are, and I hope that you each see a little bit of yourself reflected in the work presented here. My accomplishments are yours as much as they are mine.

For the preservation of our natural world. May it remain beautiful for generations to come.

Ad maiorem Dei gloriam.

Chapter 1

Introduction

1.1 Project Overview

This thesis was initially motivated by the central theme of what is now its third chapter, a study of the turbulence and mixing characteristics in Amundsen Gulf, in the southeastern Beaufort Sea, using a series of original and tightly resolved ocean microstructure measurements from an ocean glider. Direct observations of turbulent mixing in the Beaufort Sea are rare by any measure, but ours are the first to have been collected here with a robotic platform that allows for the high spatial and temporal resolution required to observe the stochastic nature of ocean turbulence. Because turbulence in the ocean is inherently patchy and intermittent, characterizing it from field observations requires many densely spaced measurements that can accurately represent the rare but important energetic mixing events that dominate tracer fluxes. Proposing to use an autonomous ocean glider to carry out these measurements provided us with a way to overcome this challenge and so, with the prospect of an exciting and novel series of measurements, we set out to plan, organize, and execute the necessary field work. We used the glider to measure both shear and temperature microstructure in Amundsen Gulf and, in so doing, collected what is—to our knowledge—the single largest set of ocean turbulence measurements in the Canadian Arctic to date. The field campaign was overwhelmingly successful, though as we began to analyze the measurements, it quickly became clear that the novelty of the data we had collected opened a wholly new set of questions. Largely, these were questions that we hadn't previously realized needed asking but without which we wouldn't be able to do justice to the original research aims of the project. Those questions could be broadly grouped into two major categories which then became the topics of what are now Chapters 2 and 4 of this thesis.

The first of these topics—the need for which became painfully obvious during the early

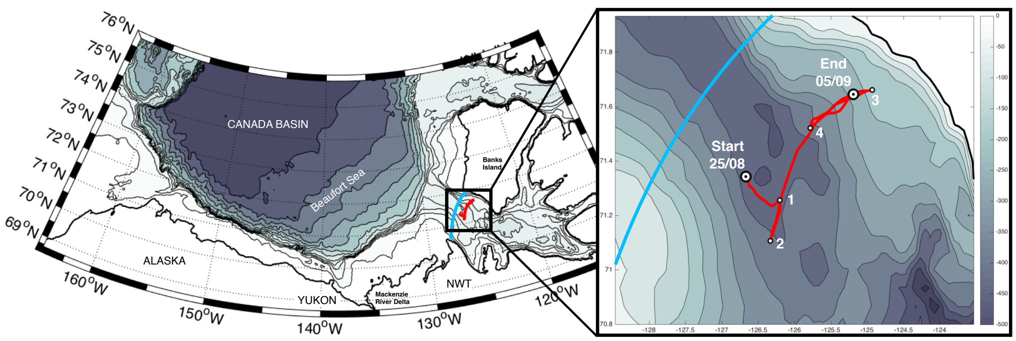

Figure 1.1 – The glider's 10 day path in the Amundsen Gulf along which it measured 348 microstructure profiles in summer 2015. Shown are the start and end points/dates, as well as the location of four intermediate waypoints. The light-blue line indicates approximately the north-eastern boundary beyond which it was unsafe to operate the glider because of the possibility of sea ice.

stages of the analysis—was understanding why the results we obtained from the shear and temperature measurements were not the same. The results agreed well when turbulence was reasonably energetic, but when it became weaker, the dissipation rate estimates we derived from the two types of measurement differed by as much as two orders of magnitude. This difference was not something that could be relegated to the surprisingly ubiquitous black box of "uncertainties typical to microstructure measurements" often invoked for ocean turbulence data; rather, it was substantial enough that it had a meaningful impact on the final interpretation of the measurements and, we felt, it could not be ignored or averaged away[1]. It needed to be explained. In addition, the coming decade is almost certain to see an expansion in the number and scope of Arctic Ocean microstructure studies (Carmack et al., 2015), and since the divergence—which we determined was largely a result of sensor limitations—was noticeable only because of the Beaufort Sea's uncharacteristically-weak turbulence, we concluded that sorting out the reasons for the large difference between the shear- and temperature-derived results, and reporting those publicly, was an important and worthwhile endeavour. That endeavour became the study that is now Chapter 2, the conclusions of which, we hope, will help inform the future collection and interpretation of microstructure measurements in weakly turbulent environments.

The second important thing we noticed very early in the analysis was that density strati-

[1]This is not intended to sound irreverent. Consider, as an example, the following assessment by Mike Gregg, one of the early pioneers of microstructure measurement: *An interesting dichotomy exists between the kinematical models of mixing and the analysis of microstructure data. The kinematical models predict that all mixing occurs as short-lived overturns formed when the superposition of random internal wave motions causes the Richardson number to drop below 1/4. On the other hand, measurements of temperature microstructure are interpreted with a model based on the assumption of steady, homogeneous turbulence. Those of us who examine oceanic data have long recognized this incongruity, hoping that it all works out in the averaging. This, however, has yet to be demonstrated.* (Gregg, 1987, Section 7)

fication in the environment we were working in was very clearly a dominant contributor to the turbulence dynamics. In one sense this was obviously a problem, and it would prove to plague the interpretation of our measurements throughout the project because the processing of turbulence measurements relies very explicitly on the assumption that the smallest, viscous-scale, turbulent eddies are isotropic and, therefore, unaltered by buoyancy effects. However, it also led to one of the most fascinating findings of the project, which is that turbulent-scale variance in the temperature field (and the associated enhanced heat flux) never fully vanished in any of our observations even when models based on laboratory and numerical studies predicted that it should do so given the relatively strong density stratification. We observed a meaningful turbulent heat flux in environmental conditions in which present models predict only vanishing tracer fluxes, which was both surprising and exciting. The observation of turbulent heat fluxes in such weakly turbulent, strongly stratified conditions highlights the limitations of present turbulence models that are used to interpret microstructure measurements and make predictions about tracer fluxes. Given that much of the global ocean pycnocline is characterized by similar strong-stratification-and-weak-turbulence conditions, this observation has the potential to impact how we conceptualize mixing in the ocean well beyond only in the relatively small, localized region of our measurements. The discussion of this observation and its potential implications is now presented in Chapter 4.

1.2 Research Questions

Given the context in Section 1.1, and with the liberty of retroactive motivation, we can usefully define the science topics of this project in the following three subsets, each with its own series of research questions:

i. Observing weak turbulence in strong stratification

- Estimates of the turbulent kinetic energy (TKE) dissipation rate, ε, are foundational to quantifying oceanic diffusivity. However, when turbulence is very weak, microstructure sensors function at their operational limit. Do sensor limitations hinder the ability to formulate meaningful ε estimates in these conditions?

- If sensor limitations do impact the ability to measure ε when turbulence is weak, as it is in much of the Beaufort Sea, in what conditions and to what extent do they do so? And, what is the impact of those limitations on the interpretation of the measurements?

- How are uncertainties in ε estimates impacted when turbulence is weak and stratification is strong and the assumption of isotropic, homogeneous, steadily forced turbulence becomes increasingly intractable?

ii. Turbulent mixing in the Arctic Ocean's Amundsen Gulf

- What are the turbulence and mixing characteristics in the Amundsen Gulf region of the Beaufort Sea? Can we develop statistical metrics of ε and turbulent diffusivity, K_ρ, and describe their spatial and temporal variability?
- What is the magnitude of vertical heat fluxes associated with turbulent mixing in Amundsen Gulf? Is it significant when compared to mean heat budget estimates of the region and in light of recent increases in sea ice loss?
- What physical mechanisms are responsible for the observed turbulence and mixing characteristics in this region?

iii. Enhanced heat fluxes in strongly stratified, weakly turbulent environments

- Can we observe the transition between turbulent and molecular diffusion in the real ocean when turbulence weakens and stratification remains strong?
- How do predictions of turbulent mixing from models compare to our observations of tracer variance when turbulence is weak and stratification is strong?
- How efficient is turbulent mixing in our observations, and how does this efficiency compare to the canonical value of 20%?

1.3 Background

This section provides a high-level overview of our understanding of ocean turbulence, how we measure it, how it relates to ocean mixing, and why we care about it in Amundsen Gulf. It is useful for context but, depending on the reader's background, not essential for understanding the main objectives of this thesis and can be skipped if the research results are the reader's primary aim.

1.3.1 Ocean Mixing and Turbulence

Ocean mixing is, along with advection, one of the primary mechanisms by which tracers are redistributed throughout the world oceans. It is directly linked to global biological production because it contributes to the availability of heat, nutrients, and oxygen in ocean ecosystems (e.g. Sarmiento et al., 2004), and it acts as a control on global climate patterns because it facilitates the meridional overturning circulation and the maintenance of the ocean thermocline (Lumpkin and Speer, 2007). As summarized concisely by Munk and Wunsch (1998), “without deep mixing, the ocean would turn, within a few thousand years, into a stagnant pool of cold salty water”.

Away from boundaries like the sea bottom, the continental margins, or the air-sea interface, irreversible mixing in the ocean appears to be driven primarily through turbulence that is created when internal gravity waves become dynamically unstable and break (MacKinnon et al., 2017). These internal waves typically come from one of three sources:

i. barotropic ocean tides that are forced over rough or anomalous topography, creating “internal tides” that radiate upwards from the sea floor with a frequency characteristic of the barotropic forcing, often that of the dominant diurnal or semidiurnal tidal constituent (e.g. Garrett and Kunze, 2007);

ii. winds that force inertial oscillations in the surface mixed layer, from which “near-inertial” internal waves propagate downwards at frequencies near the Earth’s inertial frequency (e.g. Alford, 2003; Plueddemann and Farrar, 2006); or

iii. low frequency flows that are forced over rough or anomalous topography, continually creating internal “lee waves” in their wake (e.g. MacKinnon, 2013; Nikurashin and Ferrari, 2013).

Modern process studies of ocean mixing tend to focus on the characteristics and effects of one of these processes, often with the goal of parameterizing the process in global ocean and climate models since the phenomena themselves occur on scales smaller than model grid scales. A comprehensive review of recent advancements in our knowledge of each process is given by MacKinnon et al. (2017).

The most complete collection of ocean mixing rate estimates to date, by Waterhouse et al. (2014), reports globally averaged diapycnal diffusivities of $O(10^{-4})$ m^2 s^{-1} below 1000 m depth and $O(10^{-5})$ m^2 s^{-1} above 1000 m depth. The variability is large—typical average diffusivities range between $O(10^{-6})$–$O(10^{-2})$ m^2 s^{-1}—but the globally averaged values are consistent with the estimates put forward by Lumpkin and Speer (2007) required to support the global overturning circulation. Temporal variability in ocean mixing averages appears to occur mostly at seasonal and tidal frequencies, consistent with variability in generating mechanisms driven by winds and tides (e.g. Whalen et al., 2012; Dosser and Rainville, 2016). The spatial geography of mixing is complicated, but there is clear evidence that mixing is substantially increased in regions with complex or steep topography, such as along the continental slope margins or over mid-ocean ridges (Polzin et al., 1997; Waterhouse et al., 2014; Rippeth et al., 2015). It is commonly thought that these regions therefore contribute disproportionately to large-scale water mass transformations, though specific regional sampling is often still too sparse to describe the regional mixing geography in detail. Regional downscaling of ocean mixing observations continues to inform ongoing research questions, including those of Chapter 3 of this thesis.

Despite the general lack of regional resolution, we have in the last decade accumulated sufficient measurements to begin to see global patterns in ocean mixing rates (Whalen et al., 2012; Waterhouse et al., 2014), in large part due to the utility of autonomous sampling systems (specifically, the Argo and Ice-Tethered-Profiler systems). However, the vast majority of these diffusivity estimates rely on parameterizations of fine scale (i.e. O(1)–O(10) m) measurements to characterize the effects of centimetre-scale turbulence (Polzin et al., 2014). It is this smaller-scale turbulence that is ultimately responsible for creating the irreversible mixing that defines water mass transformations, so it is essential that the fine scale estimates always be compared to measurements of ocean turbulence which can be related directly to the rates of tracer diffusion (as described in Sections 1.3.3–1.3.6). This is the primary way in which we validate the effectiveness of the more easily employed fine scale parameterizations of turbulent mixing.

The fundamental techniques used to measure ocean turbulence were developed in the 1970s and early 1980s (see Lueck et al. (2002) for a review) and, though gradually improved with newer iterations, have remained largely unchanged since that time. The theoretical underpinnings behind the interpretation of those measurements (as outlined by Osborn and Cox (1972) and Osborn (1980)) have also remained largely the same, with the notable exception that there has been a recent renewed interest in developing a better understanding of the efficiency of turbulent mixing (the proportion of turbulent kinetic energy converted to potential energy through mixing). This efficiency was traditionally considered to be a constant 20% based on theoretical and laboratory results compiled by Osborn (1980), but it has now become exceedingly clear that this quantity is variable in the real ocean and dependent on the time evolution of the turbulence (Gregg et al., 2018).

Traditionally, ocean turbulence measurements have been prohibitively difficult to collect on a large scale because traditional free-falling microstructure profilers are expensive and tedious to operate and because microstructure probes break easily and, in the case of shear probes, are prone to contamination from vibrational noise (Lueck et al., 2002). Logistic difficulties are further amplified in the Arctic Ocean because of its remoteness and harsh environmental conditions and by the presence of sea ice. As a result, only a relatively small number of researchers have measured turbulence in the Arctic Ocean—notable studies from the western Arctic include Padman and Dillon (1987); Rainville and Winsor (2008); Bourgault et al. (2011); Shroyer (2012); Shaw and Stanton (2014); Rippeth et al. (2015). However, it has recently been demonstrated that autonomous ocean gliders are exceptional platforms for microstructure (i.e. turbulence) measurements, on par with the best free falling profilers (Fer et al., 2014; Peterson and Fer, 2014). Further, because they do not require continued manual labour or ship time, they are able to collect turbulence measurements at a much higher spatial density, and in worse sea conditions, than can be practically collected from traditional profilers lowered into the ocean from the side of a ship.

The high density of measurements available from a glider also naturally addresses concerns that arise from two fundamental problems inherent in turbulence measurements: the patchiness and intermittency of turbulent overturns. It has long been established (e.g. Gregg, 1987) that turbulence is a temporally intermittent process that occurs in isolated patches in space. As a result, turbulent variables such as the turbulent components of shear variance (Section 1.3.4) and temperature variance (Section 1.3.5) are lognormally distributed in the ocean (Gibson, 1987); consequently, turbulent variables need to be sampled at a high temporal and spatial resolution if the mean properties of the sample distributions need to reflect those of the underlying population distributions (as they do when, e.g., characterizing mean mixing rates). One important function of this present thesis is to demonstrate that gliders help to alleviate concerns related to under-sampling because, unlike traditional ship-based platforms, gliders can measure turbulence continually over many days or weeks and with a tightly resolved spatial resolution.

1.3.2 Turbulence Measurements from Gliders

We opted to use a Slocum G2 ocean glider as the platform for our turbulence measurements. Gliders are autonomous underwater vehicles that propel themselves by adjusting their density relative to that of the ambient seawater, allowing the positive or negative buoyancy to accelerate them vertically through the water column. Horizontal motion comes from hydrodynamic lift that is created by the body and wings of the instrument as moves it vertically, resulting in a characteristic vertical zig-zag profiling pattern similar to that of traditional ship-based *tow-yo* profiles. A nominal glide angle is about 25° from the horizontal, with a typical profiling speed of about 35 cm s^{-1}. The heading between pre-programmed waypoints is maintained with a small digital tail-fin.

Because glider propulsion requires no moving parts except at the turnaround points at the tops and bottoms of profiles, gliders have proven to be ideal platforms for turbulence measurements, which tend to be sensitive to mechanical vibrations. Gliders can resolve exceptionally small turbulence signals without vibrationally-induced noise contamination, resulting in a measurement quality that is comparable to that from traditional free-falling vertical microstructure profilers (Fer et al., 2014). This capability is one of the reasons we are able to address the first set of research questions of this thesis where we compare the very low-end of measurable turbulence signals from shear and temperature probes; without a vibration-free platform, the lower limit of the measurements would not be available to us because it would be masked by vibrational noise.

While gliders are becoming standardized technology—they are now well into their second decade of use for oceanographic science—the collection of microstructure measurements from gliders is still relatively novel. For Slocum gliders, the first proof-of-concept for including a self-contained microstructure measurement package, known as a *MicroRider* and produced by *Rockland Scientific International Inc.*, was published by Wolk et al. (2009). The first published field study using a MicroRider and Slocum glider was by Fer et al. (2014); since then, the same configuration has been used for various applications in studies by Peterson and Fer (2014); Palmer et al. (2015); Schultze et al. (2017); St Laurent and Merrifield (2017), and Merckelbach et al. (2019).

1.3.3 The Dissipation Rate of Turbulent Kinetic Energy

The TKE dissipation rate, ε, is the most common quantitative proxy for "turbulence intensity" in oceanographic observations. Formally, it is the rate at which viscous friction within the interior of a fluid removes kinetic energy from a flow. Because kinematic viscosity becomes a dominant force only at small scales, the rate at which it dissipates energy is a measure of dissipative-scale fluid motion. That rate is defined as

$$\varepsilon \equiv 2\nu \left\langle s_{ij} s_{ij} \right\rangle, \tag{1.1}$$

written using index notation[2] and brackets $\langle\rangle$ to denote an ensemble average. The factor ν is the kinematic viscosity, and the term s_{ij} is the strain-rate tensor:

$$s_{ij} = \frac{1}{2}\left(\frac{\partial u_i'}{\partial x_j} + \frac{\partial u_j'}{\partial x_i}\right) \tag{1.2}$$

where u_i' and x_i are components of the 3-dimensional turbulent-velocity and position vectors, respectively[3]. In the field, usually only one or two of the nine strain-rate tensor components are measured at any given time, so in practice oceanographers typically assume that all perpendicular velocity derivatives in (1.2) are equal—i.e. we assume isotropy—and the summation in (1.1) collapses to a single term (Taylor, 1935), giving the simplified relation:

$$\varepsilon = (15\,\nu/2)\left\langle (\partial u'/\partial z)^2 \right\rangle. \tag{1.3}$$

[2] sum repeated indices: $s_{ij}s_{ij} = s_{11}s_{11} + s_{12}s_{12} + s_{13}s_{13} + s_{21}s_{21} + s_{22}s_{22} + \ \dots$

[3] for example, $s_{13} = \partial u/\partial z + \partial w/\partial x$

In this example, we are representing ε with the horizontal velocity component u' and the vertical coordinate z, but since the flow is assumed isotropic, any pair of perpendicular velocity and space coordinates may be used in their stead. The rate ε has units m^2 s^{-3} or W kg^{-1} and varies in the ocean by over 10 orders of magnitude, typically in the range O(10^{-11}) to O(10^{-2}) W kg^{-1}.

1.3.4 Shear Microstructure

From Equation 1.3, the variance of turbulent-scale velocity shear is linearly proportional to the TKE dissipation rate, so the problem of estimating ε reduces to measuring $\partial u'/\partial z$. We do this following the traditional approach of Osborn and Crawford (1980), using an airfoil shear probe made from a piezoelectric beam that produces a voltage, E_p, in response to a small trans-axial force. With knowledge of the profiling speed, $\mathcal{U}$, force measurements are transformed into $\partial u'/\partial z$ estimates according to

$$\frac{\partial u'}{\partial z} = \frac{1}{\hat{s}\mathcal{U}^2}\frac{\mathrm{d}E_p}{\mathrm{d}t}, \tag{1.4}$$

where $\hat{s}$ is a manufacturer-determined calibration constant. A comprehensive review of the history and requirements of microstructure probes is given in Lueck et al. (2002).

In practice, the calculation of the shear signal variance is always done in Fourier space by integrating power density spectra of small subsets of the shear measurements. Performing the calculation in Fourier space has two distinct advantages: *i.* it allows one to exclude components of the signal at wavenumbers contaminated by measurement noise, electronic or otherwise (e.g. Goodman et al., 2006), and *ii.* it allows comparison to a "universal" shape of turbulence shear spectra, which can provide insight into the nature of the measurement and/or the flow (Figure 1.2a). For example, in reference to this second point, shear spectra in fully developed turbulence are anticipated to exhibit an *inertial subrange* where kinetic energy is passed inviscidly from larger, more energetic eddies to small viscous eddies that dissipate energy (whose wavenumber range is known as the *dissipative subrange*). The integration of the power density spectra occurs over a mix of the inertial and dissipative subranges, as available: a larger portion of the inertial subrange is typically resolved in energetic turbulence while more of the viscous subrange is usually resolved in weak turbulence. Details about our variance calculation are given in Section 2.3.2; for greater detail about the subranges of turbulence spectra, the reader is referred to (Shroyer et al., 2017).

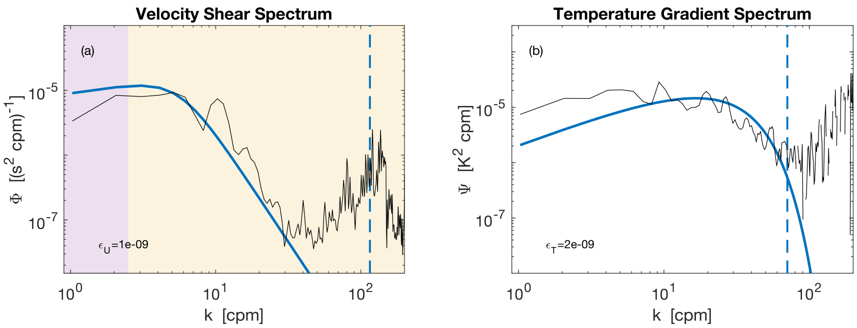

Figure 1.2 – (a) Example measured shear spectrum (Φ, black line) with a fitted empirical Nasmyth spectrum (blue line). The upper end of the inertial subrange can be seen to the left of the "viscous rolloff", indicated by the purple shading. Yellow shading indicates the viscous subrange where viscosity begins to remove kinetic energy from the turbulent flow. The Kolmogorov wavenumber is shown by the vertical dashed line. The dissipation rate estimate ε_U is also given (the subscript U indicates a velocity shear-derived estimate). (b) Example measured temperature gradient spectrum (Ψ, black line) with a fitted theoretical Batchelor spectrum (blue line). The dissipation rate estimate ε_T (subscript T indicates a temperature gradient-derived estimate) is indicated. The Batchelor wavenumber is shown by the vertical dashed line.

1.3.5 Temperature Microstructure

The dissipation rate ε can also be estimated from microstructure measurements of temperature (or any other tracer), though the connection is less direct than it is for the shear measurements. Batchelor (1959) used an advection-diffusion balance for temperature to derive a theoretical spectrum for temperature gradients in the vicinity of the dissipative scale,

$$k_B = \frac{\varepsilon}{\nu(\kappa_T^{\mathrm{mol}})^2}, \tag{1.5}$$

where κ_T^{mol} is the molecular diffusivity of temperature. The scale k_B is known as the Batchelor wavenumber and quantifies the length scale at which the sharpening of temperature gradients by turbulent shear is balanced by the softening of those gradients through the molecular diffusion of heat.

This spectrum can be written analytically (Appendix A.3) and is a function of ε and the dissipation rate of temperature variance, χ. Therefore, if we can observe the power density spectrum of temperature gradients, we can determine an estimate of ε by fitting the theoretical spectrum to the observed spectrum (Figure 1.2b). The fitting procedure is computationally expensive and contains a degree of ambiguity because it takes place in two dimensions (ε and χ) but has been optimized by Ruddick et al. (2000) and appears to produce accurate estimates of ε.

The dissipation rate χ is the rate at which molecular thermal diffusion smoothes microscale gradients of temperature and reduces the variance of those gradients. It is linearly proportional to that variance and is formally defined as

$$\chi \equiv 2\kappa_T^{\mathrm{mol}} \left\langle (\nabla T')^2 \right\rangle . \tag{1.6}$$

In addition, it is possible to derive estimates of the local vertical heat flux from measurements of temperature microstructure using the method developed by (Osborn and Cox, 1972). In this model, the rate of temperature diffusion is directly related to the variance in the turbulent-scale temperature gradients, and the turbulent temperature diffusivity is given by

$$\kappa_T^{\mathrm{turb}} = \kappa_T^{\mathrm{mol}} \frac{3\left\langle (\partial T'/\partial z)^2 \right\rangle}{(\Delta T/\Delta z)^2} , \tag{1.7}$$

assuming isotropy in the temperature gradients at turbulent scales.

1.3.6 The Osborn Model for Mixing

For most applications, the dissipation rate ε is uninteresting by itself; typically, oceanographers care about it because they are interested in the diapycnal diffusivities of density, temperature, or other tracers, since these are the physical quantities needed to model the distribution of ocean properties. Osborn (1980) used the turbulent kinetic energy equation to relate the turbulent diffusivity of density, $\kappa_\rho^{\mathrm{turb}}$, to ε via the relation

$$\kappa_\rho^{\mathrm{turb}} = \left(\frac{R_f}{1 - R_f} \right) \frac{\varepsilon}{N^2} . \tag{1.8}$$

Here, N is the buoyancy frequency and R_f is the flux Richardson number. To arrive at Equation 1.8, Osborn assumed steady-state and neglected all divergence terms, balancing the production, $\mathcal{P}$, of TKE with a loss to thermal energy by viscous dissipation and a loss to potential energy by a buoyancy flux, $\mathcal{B}$:

$$\mathcal{P} = -\rho\varepsilon + \mathcal{B} , \tag{1.9}$$

where ρ is the density of seawater. The buoyancy flux is defined $\mathcal{B} = -g \left\langle u_3' \rho' \right\rangle$, where g is the gravitational acceleration. Defining R_f as the efficiency by which turbulence produces a buoyancy flux, $R_f = \mathcal{B}/\mathcal{P}$, and using the definitions $K_\rho \equiv -\left\langle \rho' u_3' \right\rangle / (\partial\rho/\partial z)$ and $N^2 \equiv -g(\partial\rho/\partial z)/\rho$, this balance leads directly to Equation 1.8 without further assumptions. Based on theoretical work and then-current laboratory experiments, Osborn recommended using $R_f = 0.17$ for a mixing efficiency.

1.3.7 Amundsen Gulf

The Amundsen Gulf is a large embayment in the southeastern Beaufort Sea, directly adjacent to the Canadian Arctic Archipelago. It is about 250 km east of the Mackenzie River's delta and heavily influenced by its outflow in the spring and summer (Carmack and MacDonald, 2002). It is also the site of the Cape Bathurst polynya, the largest recurring polynya in the Beaufort Sea and part of the larger panarctic circumpolar flaw lead system (Barber et al., 2010). These factors make the Amundsen Gulf a regionally important oceanographic environment and endow it with a unique ecological, social, and economic significance within the larger Beaufort Sea.

Polynyas are notoriously and disproportionately important to the ecology of Arctic regions because the perennial open water results in uncharacteristically long growing seasons and unusually high primary productivity (Stirling, 1980; Tremblay et al., 2002). The success in primary productivity is passed to higher trophic levels and supports large populations of fish, seabirds, and mammals; the Amundsen Gulf in particular is known to be the site of some of the largest aggregates of animals—polar cod, ringed seals, polar bears, beluga and bowhead whales—found anywhere in the Arctic (e.g. Harwood and Stirling, 1992; Stirling, 2002; Asselin et al., 2011; Geoffroy et al., 2011). This ecological success also makes the Amundsen Gulf region important to the cultural identities of local indigenous societies. These have hunted for subsistence along the broader Canadian Beaufort Shelf for nearly a millennium and continue to do so sustainably to the present day (McGhee, 1988; Harwood et al., 2002), though recent climate change is driving the physical and ecological environments to a "new normal" state (Serreze and Barry, 2011; Jeffries et al., 2013) and introducing uncertainty about socioeconomic adaptability and the loss of cultural identity in northern communities (Berkes and Jolly, 2001; Ford et al., 2006, 2007; Post et al., 2009; Adger et al., 2013).

Additionally, the decrease in summer sea ice that results from modern climate change begets an increased interest in the economic role of the Amundsen Gulf region. The Amundsen Gulf is the Northwest Passage's western entrance to the Canadian Arctic Archipelago, which became fully navigable for the first time in 2007 (Cressey, 2007) and may become a major future commercial shipping lane as summer sea ice continues to decrease (Prowse et al., 2009; Khon et al., 2010). The first commercial bulk cargo ship transited the Northwest Passage in September 2013 (McGarrity and Gloystein, 2013), and it appears likely that shipping traffic throughout the region will expand rapidly in the coming decades (Prowse et al., 2009; Miller and Ruiz, 2014). For comparison, the Northeastern Passage along the northern Russian coast, which is losing sea ice and becoming navigable at a quicker rate than its western counterpart, has seen a 20% exponential increase in shipping traffic year-over-year between 2009–2013 (Miller and

Ruiz, 2014); it is likely that the Northwest Passage will see a similar rise in shipping traffic as it becomes increasingly ice-free.

Each of these factors—the ecological, social, and economic reasons for the significance of the Amundsen Gulf—are inherently dependent on the physical oceanography of the region. Ocean mixing, in particular, is a primary control mechanism on the biological production potential of the region because it at least partially determines the rate at which nutrients are supplied to the surface mixed layer from deeper waters (Bourgault et al., 2011). In order to predict the ecological response of the region to future changes in climate forcing, it is important that the science community has a comprehensive understanding of the regional geography and intensity of ocean mixing at present. We cannot model potential future changes to the oceanographic environment if we do not understand its current state (Carmack and MacDonald, 2002; Rainville et al., 2011). Likewise, ocean mixing is an important driver of local heat fluxes in the water column that directly contribute to the integrated heat budget and rate-of-loss of surface sea ice in the Arctic Ocean. If we wish to predict future contributions of ocean heat to regional sea ice loss, we first need a grounded, quantitative understanding of heat fluxes in the region presently, without which we cannot predict future changes to the regional sea ice pack (Carmack et al., 2015).

Chapter 2

Measuring the Dissipation Rate of Turbulent Kinetic Energy in Strongly Stratified, Low Energy Environments

2.1 Motivation

The purpose of this study is to examine the agreement between measures of the turbulent kinetic energy (TKE) dissipation rate, ε, derived from measurements of shear and temperature microstructure in a stratified “low energy” environment, i.e. a stratified environment where the amount of turbulent kinetic energy in the flow field is unusually small. It was motivated when, in an attempt to quantify turbulent mixing in the Beaufort Sea thermocline, we discovered that results from the two measurements diverged strongly at low ε. Where TKE dissipation rate estimates from shear measurements frequently clustered near a clearly defined lower limit, estimates from temperature measurements distributed to much lower values that were often multiple orders of magnitude smaller. We noted that this discrepancy may have serious implications for how shear microstructure measurements from the Arctic Ocean are interpreted. This study is therefore dedicated to describing the divergence we observed and discussing its causes with the goal of informing the collection and interpretation of microstructure measurements in the Arctic Ocean or similar stratified low energy environments.

The western Arctic Ocean, where we collected our measurements, is known to be an exceptionally low energy, and highly stratified, ocean environment with some of the lowest estimates of oceanic turbulence in the world (e.g. Guthrie et al., 2013; Lincoln et al., 2016). Only a relatively small number of microstructure measurements from this region exist to date (e.g. Padman and Dillon, 1987; Rainville and Winsor, 2008; Bourgault et al., 2011; Shroyer, 2012; Shaw and Stanton, 2014; Rippeth et al., 2015), but this number is certain to increase in the coming years owing to increased interest in constraining oceanic heat budgets in the Arctic (Carmack et al., 2015). Constraining these budgets requires knowledge of turbulent mixing rates in the ocean which are obtained most directly from microstructure measurements; we demonstrate here why this is a challenging endeavour and why special considerations are needed when interpreting those measurements in stratified low energy environments. Our present study is therefore timely since turbulent mixing estimates from microstructure measurements have become a key component in estimating heat fluxes through the Beaufort Sea thermocline.

Both shear and temperature microstructure measurements are frequently used to estimate the dissipation rate ε, a quantity that characterizes the intensity of turbulent flows and can range over more than 10 orders of magnitude in the ocean (Gregg, 1999; Lueck et al., 2002). Ours is not the first study to compare estimates of ε from coincident shear and temperature microstructure measurements: similar comparisons were performed by Oakey (1982), Kocsis et al. (1999), and Peterson and Fer (2014). These three studies all found excellent agreement, generally within a factor of 2, between shear- and temperature-derived estimates. Our study, however, is distinct because we focus on comparing ε estimates at the very low end of reported values where shear probes in particular operate at their lower sensitivity limit. The three previous comparative studies examined primarily dissipation rates in excess of 10^{-10} W kg^{-1}. We will demonstrate that it is necessary to resolve dissipation rates lower than this in the Beaufort Sea, that ε estimates from shear and temperature measurements no longer agree at these small values, and that this disagreement can lead to serious biases in the resulting mixing rate estimates in low energy environments. In addition, we will demonstrate the way in which turbulence spectra diverge systematically from commonly used reference shapes when turbulence becomes weak and stratification becomes strong. We attribute this divergence to a breakdown of the assumption that turbulence in the flow is stationary, homogeneous, and isotropic.

2.2 Measurements

2.2.1 Measurement Platform: Slocum Glider

The platform for our microstructure measurements was the 1000 m-rated Slocum G2 ocean glider *Comet*, one of the gliders also used by Schultze et al. (2017). The glider samples autonomously in a vertical sawtooth pattern, surfacing at predetermined intervals to update its GPS-fix, send low-resolution flight and hydrography data, and receive updated sampling instructions from an onshore pilot. For a detailed review of the operation and utility of gliders, see Rudnick (2016).

The glider's onboard sensors include an SBE-41 (pumped) Seabird CTD measuring *in situ* conductivity, pressure, and temperature; a three-dimensional compass module measuring heading, pitch, and roll; and an altimeter measuring height-above-bottom. The turbulence measurements are taken with a specialized, externally mounted instrument, described in Section 2.2.2. A moveable weight that controls the pitch of the glider was set to fixed positions and only moved during inflections at the top and bottom of profiles to avoid mechanical vibrations that affect the quality of turbulence measurements mid-profile (Fer et al., 2014).

The first published use of gliders as a platform for microstructure measurements is in the proof-of-concept study by Wolk et al. (2009). Gliders have since successfully demonstrated their utility for microstructure measurements in studies by Fer et al. (2014), Peterson and Fer (2014), Palmer et al. (2015), and Schultze et al. (2017). These have shown that gliders are suitable low-noise platforms providing microstructure measurements of comparable quality to those obtained from free-falling profilers.

Gliders are able to provide continuous measurements during a deployment, yielding a spatial and temporal coverage in oceanic microstructure fields that is often unattainable from ship-based profiling, especially in inclement weather. The high density and large number of measurements obtained from *Comet* is an important feature for our study because it allows us to calculate robust statistical measures of turbulence metrics which are critical to interpreting microstructure measurements (Gibson, 1987); these have been largely unavailable from previous studies in the western Arctic Ocean where microstructure measurements are sparse.

2.2.2 Shear and Temperature Microstructure

Comet is equipped with an externally mounted turbulence package ("MicroRider") carrying two airfoil velocity shear (SPM-38) and two fast-response temperature (FP07) probes. The shear probes are of the design by Osborn (1974) and sense transverse forces in a direction perpendicular to the direction of travel (Osborn and Crawford, 1980; Lueck et al., 2002). The probes are oriented such that each measures a distinct shear component, orthogonal to that measured by the other (as in Fer et al., 2014). The temperature probes are sensitive thermistors with response times of $\sim$10 ms and sensitivities better than 0.1 mK (Sommer et al., 2013b). The microstructure probes extend beyond the nose of the glider by $\sim$17 cm, outside of the radius of flow deformation caused by the glider's motion (Fer et al., 2014). We do not install a probe guard in order to minimize the potential for contamination of the flow in the immediate vicinity of the measurement.

Besides shear and temperature, the MicroRider also measures pressure, pitch, roll, and transverse accelerations. Shear, temperature, and acceleration are sampled at 512 Hz, the other channels at 64 Hz. The MicroRider is produced by Rockland Scientific International (RSI); it is the same model used in the four glider-microstructure studies referenced in the previous section.

2.2.3 Location, Local Hydrography, and Sampling Strategy

The measurement location was the Amundsen Gulf on the southeastern margin of the Beaufort Sea (Figure 2.1a). Circulation in the region is complex and highly variable in space and time; it is strongly influenced by surface wind stress, complex local bathymetry, submesoscale frontogenesis, and the intermittent presence of mesoscale eddies (Williams and Carmack, 2008, 2015; Sévigny et al., 2015). Barotropic tidal amplitudes can be regionally large but are locally small where the glider was deployed because of the presence of a local amphidrome (Kowalik and Matthews, 1982; Kulikov et al., 2004). The presence of sea ice is seasonal; during our campaign, the southern edge of fragmented sea ice was coincident with the mouth of the Amundsen Gulf, prohibiting us from guiding the glider north towards the central Beaufort Sea as initially planned. The Amundsen Gulf was consequently selected for the measurement locale to mimic as closely as possible the hydrographic characteristics of the wider Beaufort Sea while minimizing the risk of collisions with sea ice floes.

The basin depth in Amundsen Gulf is $\sim$450 m (Figure 2.1b), well below the typical Beaufort Sea shelf-break depth of $\sim$75 m and deep enough to extend across the entire range of the thermocline separating Atlantic- and Pacific-sourced water masses. As a result, the hydrography of the region largely reflects that of the broader Beaufort Sea (Figure 2.1c–2.1e). A 10 m thick brackish surface lens, resulting from summer sea ice melt and the nearby Mackenzie River's freshwater inflow, caps a near-surface pycnocline that extends to 25 m depth and has a potential density anomaly σ that ranges between 22–24.5 kg m^{-3}. Between $\sim$25–200 m, the signatures of cold Pacific-sourced water

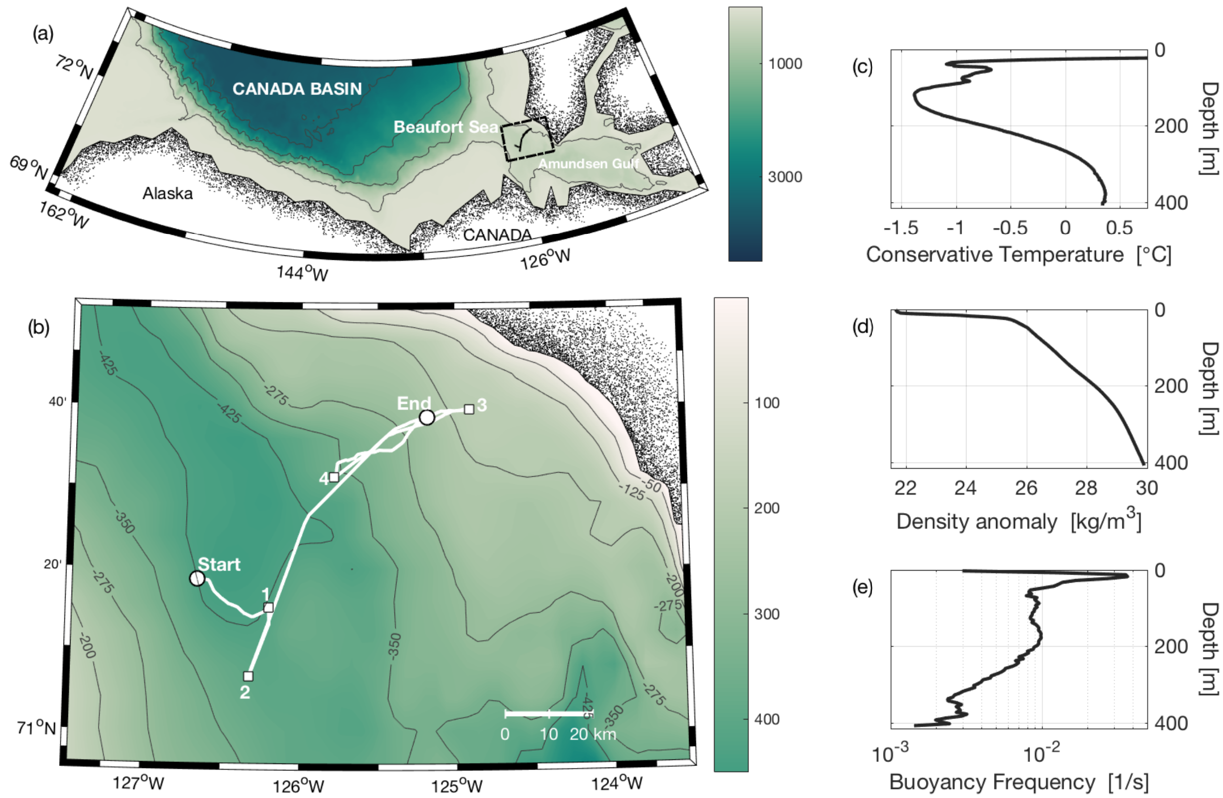

Figure 2.1 – (a) The measurement location at the entrance to the Amundsen Gulf in the south-eastern Beaufort Sea. The glider path is shown by the line inside the dashed black rectangle. Bathymetry contours are drawn at 1000 m intervals beginning at 200 m. (b) Enlarged view of the area inside the dashed rectangle indicated in panel a, showing the glider path and the local bathymetry. Selected waypoints along the path are numbered consecutively and indicated by squares for reference when reading Figures 2.2 and 2.3. Contours are drawn at 75 m intervals beginning at 50 m. In both panels, colour indicates water depth (m); bathymetry data are from IBCAO 3.0 (Jakobsson et al., 2012). Mean vertical profiles of (c) conservative temperature, (d) in-situ density anomaly, and (e) buoyancy frequency are also shown; these are horizontally averaged over all casts where the glider's maximum dive depth exceeded 325 m.

dominate the mean temperature profile leading to a temperature minimum of -1.4 °C at 120 m depth; a spatially complex submesoscale temperature structure is notably visible in this layer and modifies the mean profile between $\sim$40–110 m depth. A prominent thermocline characteristic of the Beaufort Sea extends from 125 m to the temperature maximum associated with the warm core of Atlantic-sourced water (Williams and Carmack, 2015; Rudels, 2015) at 375 m depth. Stratification is strong throughout the water column, with buoyancy frequency N of O(10^{-2}) s^{-1} in the near-surface pycnocline and O(10^{-3}) s^{-1} elsewhere.

The glider sampled continuously between August 25 – September 4, 2015, following the path outlined in Figure 2.1. It measured 348 quasi-vertical profiles over a total path length of 186 km, remaining in the deeper central Amundsen Gulf for the first 4.5 days and partially crossing the continental shelf slope three times during the remainder of the mission. The glider dove to a fixed depth of 300 m during the first 3 days; after this, it dove to within 15 m of the local bottom.

2.3 Data Processing

Processing microstructure measurements from a glider is similar to processing ones from a free falling profiler, but with added complications. Estimating the speed of the microstructure probes through water requires specialized procedures, as does screening the data for corrupt measurements. Because measuring turbulence from gliders is still a novel technique, we outline here in detail the steps we take to go from microstructure measurement to dissipation rate estimate, including our procedure for estimating the glider's velocity underwater. The quality control criteria we use to flag and discard suspect measurements, a comparison of TKE dissipation rate results from up- and downcasts, and a brief description of Nasmyth and Batchelor reference spectra are provided in the Appendix.

Throughout the text, the symbol ε is used for the TKE dissipation rate generally, ε_U for dissipation rate estimates obtained from velocity shear measurements, and ε_T for dissipation rate estimates obtained from temperature measurements. All wavenumbers are defined cyclicly, with units cpm. Note the cyclic wavenumber is related to the radian wavenumber $\hat{k}$, which has units m^{-1}, through the relation $k = \hat{k}/2\pi$. The kinematic viscosity, ν, of seawater is evaluated locally using TEOS-10 (McDougall and Barker, 2011) because it varies by more than 20% in our measurements. We use $\kappa_T^{\mathrm{mol}} = 1.44 \times 10^{-7}$ m^2/s for the molecular diffusion coefficient of temperature and $q_B = 3.4$ for the Batchelor constant; the latter is required when evaluating the Batchelor spectrum (Section 2.3.3), and a sensitivity analysis for this parameter is presented in the Appendix Section A.3. Measurements from the MicroRider's clock, pressure sensor, and temperature probes are prone to low-frequency drift; thus, the low-frequency response from each of these channels is corrected to measurements from the glider. Note that unless otherwise stated, we average quantities that span many orders of magnitude using the geometric mean, and we use the term "trimmed mean" to refer to an average calculated over the central 90% of data.

2.3.1 Glider Velocity Estimates

The processing of microstructure measurements to obtain dissipation rates is heavily reliant on accurate knowledge of the speed, $\mathcal{U}$, with which the probes travel through water. Unfortunately, there is no direct measurement of the glider's speed underwater: the

	θ [°]	α_a [°]	γ [°]	$\mathcal{U}$ [cm s^{-1}]
upcasts	21.8 ± 1.0	-4.7 ± 0.2	26.4 ± 0.9	41 ± 4
downcasts	-21.3 ± 0.8	4.8 ± 0.1	-26.0 ± 0.6	25 ± 4

Table 2.1 – Mean $\pm$ one standard deviation of glider-flight variables from all up- and downcasts of the mission. θ is the measured pitch, α_a the estimated angle of attack, γ the estimated glide angle, and $\mathcal{U}$ the estimated speed through water. Only data coincident with at least one viable ε estimate (see Appendix A.1) are included.

glider pitch, θ, and rate-of-change of pressure are known, but this is not enough information to directly obtain $\mathcal{U}$ because the glider travels with an unknown and variable angle of attack, α_a, which in our experience is usually in the range $1^\circ < |\alpha_\mathrm{a}| < 10^\circ$.

Studies by Fer et al. (2014), Peterson and Fer (2014), and Palmer et al. (2015) use a hydrodynamic flight model developed by Merckelbach et al. (2010) to estimate $\mathcal{U}$. The model assumes a steady state balance of drag, buoyancy, and lift forces to optimize estimates of $\mathcal{U}$ and a drag coefficient C_{D_0}. The angle of attack is then obtained numerically from the implicit relation

$$\alpha_\mathrm{a} = -\left(\frac{C_{D_0} + C_{D_1}\alpha_\mathrm{a}^2}{A\tan\gamma}\right) \tag{2.1}$$

where $\gamma = \theta - \alpha_\mathrm{a}$ is the glide angle, and C_{D_1} and A are constants optimized for Slocum gliders in Merckelbach et al. (2010).

In contrast to this approach, we follow the method of Schultze et al. (2017) and use the steady state model of Merckelbach et al. (2010) to obtain the angle of attack, but then use the measured pitch and pressure to estimate $\mathcal{U}$ dynamically using

$$\mathcal{U} = \frac{\mathcal{W}}{\sin\gamma}, \tag{2.2}$$

where $\mathcal{W}$ is the glider's vertical velocity estimated from the measured rate-of-change of pressure. We found that this quasi-dynamic estimate of $\mathcal{U}$ leads to more consistent results between profiles of ε from up- and downcasts. Note that angles are measured positive upwards, θ and γ relative to the horizontal, α_a relative to the glide angle γ.

Mean and standard deviation values of selected glider flight characteristics separated by up- and downcasts are summarized in Table 2.1 to enable comparison with previous studies. For the most part, the values presented are not remarkable and are similar to ones previously reported, albeit with marginally larger angles of attack. One exception is the relatively large discrepancy in $\mathcal{U}$ between up- and downcasts. The discrepancy arises because of the strong near-surface stratification in the Beaufort Sea, resulting in asymmetric dive and climb rates over most of the water column; however, we do not see a significant systematic effect on the dissipation rate results (see Appendix A.2), and we do not differentiate between up- and downcasts from here on.

2.3.2 Shear Microstructure

The procedure we use to process the shear measurements uses code provided by RSI and is based on recommendations outlined in their documentation. We provide an overview here; a comprehensive rationale for the algorithm and detailed review of recommended procedures is available in RSI's Technical Note 028 (Lueck, 2016).

We calculate the dissipation rate from the viscosity and the variance of the turbulent velocity shear according to $\varepsilon_U = 7.5\nu \left\langle (\partial u'/\partial x)^2 \right\rangle$, assuming isotropic flow. Here, angled brackets indicate averaging, x represents the glider's along-path coordinate, and u' represents either of the two perpendicular turbulent velocity components. As discussed in Section 2.5.3, the isotropy assumption is problematic when energetics are weak and stratification is strong, and it leads to increased uncertainty in the observed dissipation rates, but it is necessary to make the assumption because we measure only two of the nine strain rate tensor components.

We estimate the variance from the measured shear record in half-overlapping 40 s segments. Each of these is further subdivided into 19 half-overlapping 4 s subsegments which are detrended, cosine-windowed (in a variance-preserving manner), and transformed into shear power spectra using a fast Fourier transform (FFT). These 19 spectra are averaged to create one "observed" shear power spectrum, Φ, for each 40 s segment of shear measurement. Coherent acceleration signals measured by the MicroRider are removed from Φ using the algorithm proposed by Goodman et al. (2006). Frequencies, f, are transformed to wavenumbers, k, using the glider's mean speed, $\overline{\mathcal{U}}$, over the 40 s and assuming Taylor's frozen turbulence hypothesis, i.e. $\Phi(k) = \overline{\mathcal{U}}\Phi(f)$ and $k = f/\overline{\mathcal{U}}$.

The 4 s length of the subsegments passed to the FFT sets the scale for the largest wavelength (smallest wavenumber) included in the shear spectrum $\Phi(k)$; it is identical to the FFT length chosen by Fer et al. (2014) and Schultze et al. (2017). Given the average glider speeds in Table 2.1, a typical FFT calculation includes along-path wavelengths as large as 164 cm on upcasts and 100 cm on downcasts, resolving the low wavenumber transition between the inertial and viscous ranges of the turbulence spectrum (Lueck et al., 2002). The choice of 40 s for the total averaging length, corresponding on average to 16.4 m on upcasts and 10 m on downcasts, is larger than the 12 s averaging length used in the above mentioned studies; it is a heuristic choice and a compromise which trades a decrease in the spatial resolution of the observations in favour of an increase in the statistical confidence of individual ε_U estimates (Lueck, 2016).

We numerically integrate each $\Phi(k)$, calculating ε_U according to

$$\varepsilon_U = 7.5\nu \int_0^{k_u} \Phi(k)\mathrm{d}k. \tag{2.3}$$

Here, k_u is an upper integration limit, chosen to exclude large wavenumbers at which electronic noise dominates the measurement. To choose k_u, we fit a third-order polynomial to $\Phi(k)$ in order to isolate the location of the spectral minimum which typically indicates the onset of noise domination, but we constrain k_u to be at least 7 cpm. Note that in a low-energy environment most of the variance is at low wavenumbers: 90% of the variance lies below 7 cpm when $\varepsilon = 10^{-10}$ W kg^{-1} (Gregg, 1999).

To account for unresolved variance, we calculate the fraction, P, of the integral of the nondimensionalized empirical Nasmyth spectrum (Nasmyth, 1970; Oakey, 1982) that is resolved below the nondimensionalized integration limit $k_u/(\varepsilon_U/\nu^3)^{1/4}$. We then scale up ε_U by a factor of $1/P$ and iterate the correction procedure until the change in ε_U in successive iterations is less than 2%.

We further correct for a small integration underestimate that occurs between the origin and the first non-zero wavenumber k_1. The Nasmyth spectrum rises approximately as $k^{1/3}$ and so its integral to k_1 is proportional to $(3/4)k_1^{4/3}$; trapezoidal integration between $k = 0$ and k_1, however, is proportional only to $(1/2)k_1^{4/3}$. We correct by adding the term $7.5\nu(1/4)k_1\Phi_N(k_1)$, where $\Phi_N(k_1)$ is the value of the Nasmyth spectrum at k_1. Note that the two correction procedures described here are both standard features implemented in the provided RSI codes.

There are two distinct shear probes (Section 2.2.2), yielding two independent, simultaneous ε_U estimates. When both estimates pass quality control, we average them; when only one passes quality control, we use that single estimate for the analysis presented in Section 2.4. Note that, on average, we do not see a meaningful difference between results from the two shear probes (see Appendix A.1).

2.3.3 Temperature Microstructure

The dissipation rate ε_T may be estimated from temperature microstructure measurements by determining the Batchelor wavenumber, defined $k_B = (1/2\pi)\left(\varepsilon_T/\nu(\kappa_T^{\mathrm{mol}})^2\right)^{1/4}$, and inverting to yield

$$\varepsilon_T = \nu(\kappa_T^{\mathrm{mol}})^2(2\pi k_B)^4. \tag{2.4}$$

We determine the Batchelor wavenumber by fitting the theoretical Batchelor spectrum (Batchelor, 1959) to observed power spectra of temperature gradients using the procedure outlined below, which is modelled on descriptions by Ruddick et al. (2000), Steinbuck et al. (2009), and Peterson and Fer (2014).

We first calculate a temperature power spectrum, Λ, from the temperature measurements for each of the same half-overlapping 40 s segments that we used to calculate the shear spectra. Each spectrum is again the average of 19 spectra calculated from half-overlapping, detrended and cosine windowed 4 s subsegments. Values of Λ at high frequencies, where the temperature probes' temporal response is inadequate, are corrected using the transfer function proposed by Sommer et al. (2013b). Like shear spectra, temperature spectra are transformed from frequency to wavenumber space using $\overline{\mathcal{U}}$ and Taylor's frozen turbulence hypothesis.

From each Λ, we next calculate a "raw" one-dimensional temperature gradient power spectrum, Ψ_r, using the variance preserving transformation

$$\Psi_\mathrm{r} = (2\pi k)^2 \Lambda \,. \tag{2.5}$$

From each of these we then subtract a probe-specific noise spectrum:

$$\Psi = \Psi_\mathrm{r} - \Psi_\mathrm{ns} \,, \tag{2.6}$$

where Ψ_ns is the noise spectrum, empirically determined for each probe by averaging the 1% of raw spectra with the least observed variance. We refer to Ψ as the "observed" temperature gradient spectrum. Note the temperature gradients are defined with respect to the along-glider path coordinate.

We next estimate the rate, χ, of destruction of temperature gradient variance (Osborn and Cox, 1972) from the observed temperature gradient spectra. Following Steinbuck et al. (2009), we iteratively calculate

$$\chi = \chi_\mathrm{lw} + \chi_\mathrm{obs} + \chi_\mathrm{hw} = 6\kappa_T^\mathrm{mol} \left(\int_0^{k_l} \Psi_\mathrm{B} \mathrm{d}k + \int_{k_l}^{k_u} \Psi \mathrm{d}k + \int_{k_u}^{\infty} \Psi_\mathrm{B} \mathrm{d}k \right), \tag{2.7}$$

on each iteration subsequently fitting the Batchelor spectrum, Ψ_B, to the observed spectrum as described below. The term χ_obs is the component of χ that comes from integrating the observed spectrum between wavenumbers k_l and k_u. At wavenumbers outside this range, the observed spectrum is not reliable and we instead integrate Ψ_B to obtain the correction terms χ_lw and χ_hw. Note the correction terms are unavailable and thus set to zero for the first iteration. The factor of 6 arises from assuming isotropic flow.

We fit the Batchelor spectrum between wavenumbers k_l and k_u on each iteration using the maximum likelihood procedure described by Ruddick et al. (2000). This procedure minimizes a cost function to choose the best fit from a family of Batchelor curves which are constructed using constant χ but variable k_B. For the upper limit k_u we choose the intersection between Ψ_r and $2\Psi_{ns}$. The lower limit k_l is the smallest available non-zero wavenumber k_1 on the first iteration, and on subsequent iterations is the greater of k_1 and $3k_*$, where $k_* = 0.04k_B(\kappa_T^{mol}/\nu)^{1/2}$ represents the top of the convective subrange (Luketina and Imberger, 2001). We implement three iterations, enough for k_B estimates to converge (Steinbuck et al., 2009), and then calculate ε_T from Equation 2.4.

There are two distinct thermistors (Section 2.2.2), yielding two independent, simultaneous ε_T estimates. As with the shear-derived estimates, when both pass quality control (see Appendix A.1), we average; when only one passes, we use the single estimate for our analysis.

2.4 Comparison of Results from Temperature and Shear Microstructure

Here we present ε estimates derived from our coincident microstructure measurements of shear and temperature, demonstrating how the two estimates agree on average within a factor of two when $\varepsilon > 3 \times 10^{-11}$ W kg^{-1} but diverge for smaller dissipation rates. We demonstrate that this divergence leads to inconsistencies between statistical metrics that describe the two sets of observations. Using evidence presented in Sections 2.4.3 and 2.4.4, and in anticipation of the discussion presented in Section 2.5.1, we attribute differences between the ε_U and ε_T datasets to the effects of the ε_U noise floor. With this foreknowledge, our description of these differences can be interpreted as a case study that demonstrates the degree by which the ε_U noise floor influences the ability of the shear measurements to characterize the dissipation rate in a stratified, low energy environment.

2.4.1 Spatial Cross Sections

A qualitative comparison of the dissipation rates derived from shear and temperature microstructure measurements is generally favourable. This can be seen in spatial cross sections of ε_U and ε_T (Figure 2.2). Both fields exhibit obvious variability over at least three orders of magnitude and indicate the same coherent patches of enhanced turbulence superimposed on a less turbulent background. In both fields, these patches are characterized by dissipation rates O(10^{-9}) W kg^{-1}. They have a spatial coherence on scales O(10)–O(100) m vertically and O(10) km horizontally. Three easily identifiable examples, seen in both panels, are between approximately (i) 10–20 km at depths 105–305 m, in the central Amundsen Gulf; (ii) 52–81 km at depths 155–400 m, at the edge of the shelf-slope; and (iii) 161–183 km within a 75 m band above the sea floor, on the

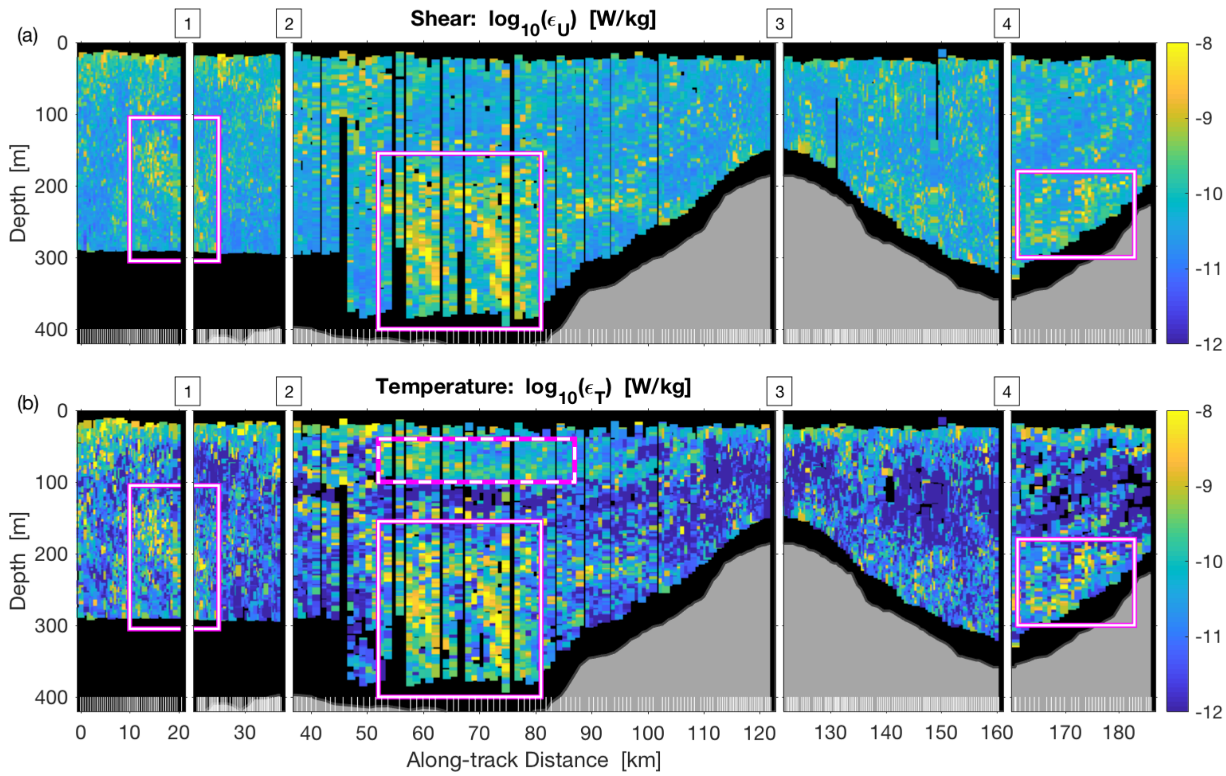

Figure 2.2 – Cross sections of the turbulent dissipation rate, ε, in $\log_{10}$ space, derived from microstructure measurements of (a) shear and (b) temperature. The panels are drawn using the same colour scale. Grey shading indicates the bathymetry, black shading discarded or unavailable data (see Section 2.2.3 and the Appendix). Small white lines along the horizontal axis indicate the locations of individual profiles. The breaks in the horizontal axis, labelled 1–4, correspond to the waypoints shown in Figure 2.1b. Magenta rectangles with solid white lines indicate regions of enhanced dissipation discussed in the text. The magenta rectangle with dashed white line in panel (b) indicates the signature of the mesoscale eddy discussed in the text.

shelf slope. These are indicated in the figure with magenta rectangles. The qualitative similarity between the two independently derived estimates is encouraging and suggests that temperature and shear probes may be used to qualitatively identify the same regions of enhanced turbulence.

Figure 2.2, however, also reveals an immediate difference between the observed ε_U and ε_T fields: these indicate markedly different background states, easily seen in the figure because the images in the two panels are drawn with the same colour scale. The ε_U field from the shear measurements indicates a background of O(10^{-11}) W kg^{-1}, imaged as a turquoise-blue colour. There appears to be no obvious variability below $\varepsilon_U \sim 5 \times 10^{-11}$ W kg^{-1}. The ε_T field from the temperature measurements, on the other hand, suggests a lower background value of O(10^{-12}) W kg^{-1}, as indicated by the frequent darker blue colours. Additional structure not seen in the ε_U observations is apparent in the ε_T field at dissipation rates between 1×10^{-12} and 5×10^{-11} W kg^{-1}. An example

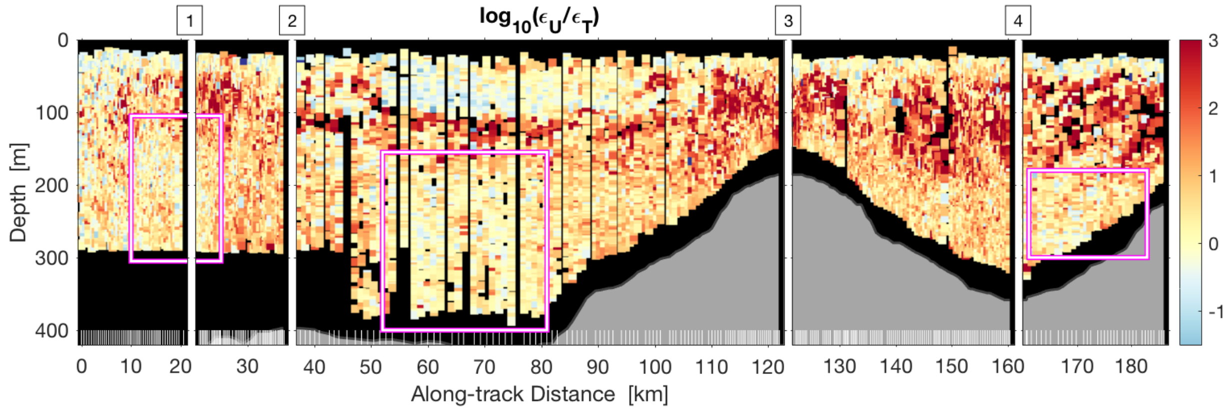

Figure 2.3 – Cross section of the ratio $\varepsilon_U/\varepsilon_T$ in $\log_{10}$ space. Shading, panel division, magenta rectangles, and annotations as in Figure 2.2.

of this phenomenon may be seen by looking at the dissipation rate signature of what appears to be a mesoscale eddy whose presence can be identified in the temperature and density fields (not shown) at depths 40–100 m between 52–87 km: it carries an obvious signature of enhanced dissipation in the ε_T field (Figure 2.2b, dashed magenta box), but in the ε_U field (Figure 2.2a) no such signature can be identified.

The magnitude of the discrepancy between the two fields is apparent when visualizing a cross section of the ratio $\varepsilon_U/\varepsilon_T$ (Figure 2.3). The discrepancy is largest, at times larger than a factor of 10^3, in a band approximately at 50–150 m depth and between 100 km and the end of the glider track. Comparing with Figure 2.2, this region tends to coincide with the region where ε_T is smallest. The discrepancy is less pronounced, however, in the three patches of enhanced turbulence identified in Figure 2.2; here, the ratio $\varepsilon_U/\varepsilon_T$ tends to unity.

2.4.2 Mean Vertical Profiles

We find, on average, more than an order of magnitude difference between ε_U and ε_T where dissipation rates are smallest. This can be seen in Figure 2.4a, in which the observed dissipation rate fields are horizontally averaged in 25 m vertical bins to create mean vertical profiles of ε_U and ε_T. In both profiles, the lowest dissipation rates are found between 100–125 m depth where, on average, $\varepsilon_U = 4 \times 10^{-11}$ W kg^{-1} while $\varepsilon_T = 3 \times 10^{-12}$ W kg^{-1}; there is a factor of 13 disagreement between the two. This disagreement is statistically significant: in this depth bin, the respective interquartile range (IQR) for each dataset is $\varepsilon_U = 2 \times 10^{-11}$–$8 \times 10^{-11}$ W kg^{-1} and $\varepsilon_T = 3 \times 10^{-13}$–$3 \times 10^{-11}$ W kg^{-1}, indicating little overlap between the two measurement distributions. The geometric standard deviation factors σ_g are 2.4 for ε_U and 13.4 for ε_T, reflecting the substantial horizontal variability seen in Figure 2.2 and the relatively larger range

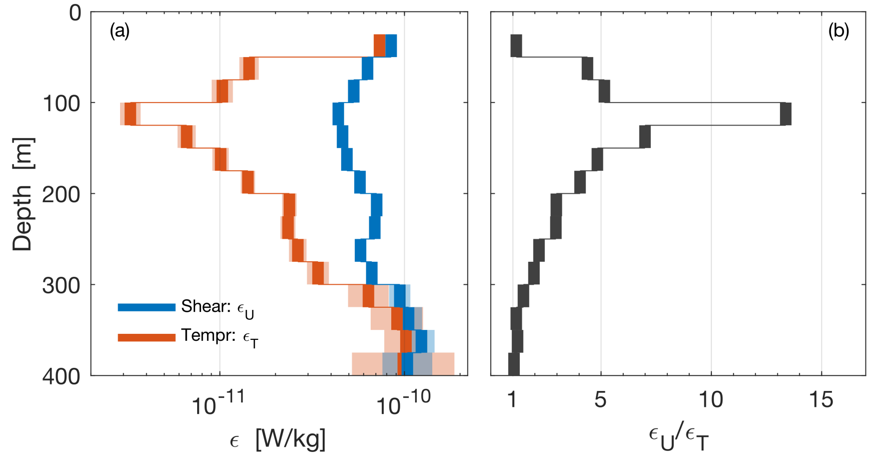

Figure 2.4 – (a) Average vertical profiles of the dissipation rates ε_U and ε_T, obtained from shear and temperature microstructure and calculated using a trimmed geometric mean in 25 m vertical bins. Shading indicates the 95% confidence interval for the mean as indicated by the geometric standard error. (b) The ratio of the average vertical profiles of ε_U and ε_T, highlighting disagreement by a factor of 5 or greater between 75–175 m depth.

of ε_T values. Despite the variability, the estimates of the mean values are robust: the 95% confidence intervals indicated by the geometric standard error (Kirkwood, 1979) are $\varepsilon_U = 4 \times 10^{-11}$–$5 \times 10^{-11}$ W kg^{-1} and $\varepsilon_T = 3 \times 10^{-12}$–$4 \times 10^{-12}$ W kg^{-1} respectively.

The discrepancy between the depth-binned mean profiles is less dramatic in the rest of the water column, and the two profiles qualitatively have a similar shape. Both exhibit small dissipation rates below 10^{-10} W kg^{-1} in the shallowest available bin (25–50 m), decreasing further to their distinct minima between 100–125 m, and then gradually increasing with depth to maximum mean values near 10^{-10} W kg^{-1} as they approach the sea bed. Disagreement between the mean values, imaged in Figure 2.4b, is a factor of 5 or greater between 75–175 m depth and smaller everywhere else. Whenever both mean values are simultaneously at least 3×10^{-11} W kg^{-1}, the agreement between them is better than a factor of 2, highlighting that the divergence between ε_U and ε_T occurs only at very low dissipation rates.

Note that our measurements tend to exhibit small ε relative to measurements from other regions of the global ocean which often exhibit typical averaged values of O(10^{-9}) W kg^{-1} and higher (Waterhouse et al., 2014). This incongruity, however, is not surprising: small dissipation rates are anticipated in the western Arctic Ocean where turbulence is thought to be exceptionally low because of limited energy input and seasonal sea ice cover (Rainville and Woodgate, 2009). Microstructure measurements from the western Arctic are very sparse, but those that do exist (Section 2.1) have so far indicated typical background dissipation rates of O(10^{-10}) W kg^{-1}.

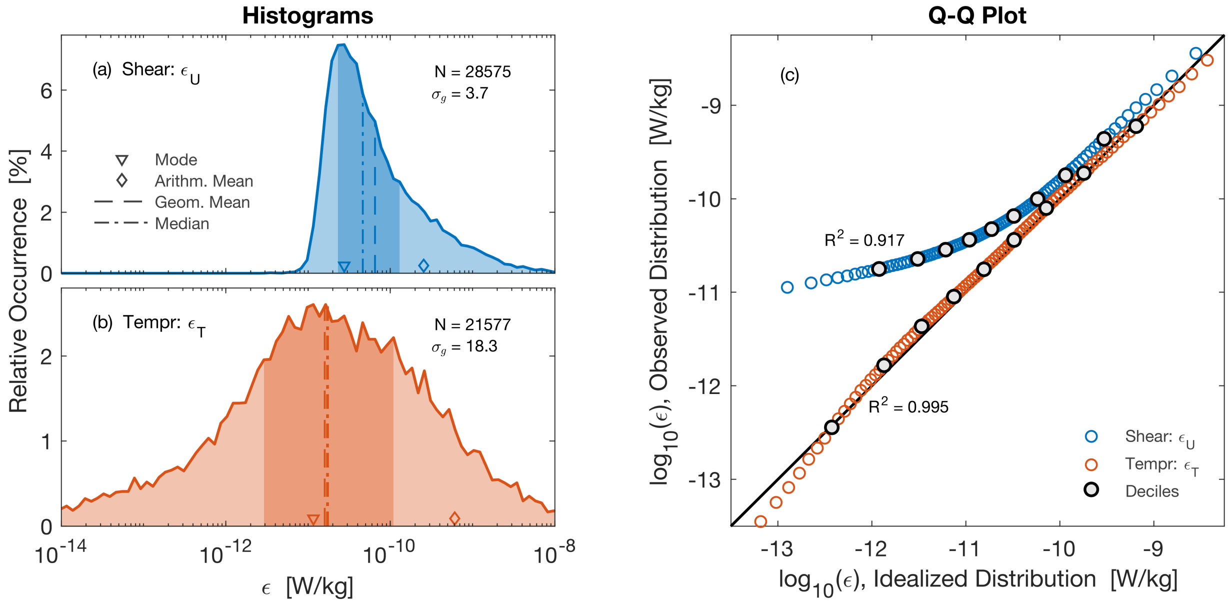

Figure 2.5 – Histograms showing the distributions of all (a) ε_U and (b) ε_T observations. The interquartile range (IQR) is indicated by the darker shading; the mode, arithmetic and geometric means, and median are marked in both panels according to the legend in (a). The labels N and σ_g indicate the total number of observations in each histogram and the geometric standard deviation factor respectively. Histograms are calculated over 100 logarithmically spaced bins. (c) Quantile-quantile plot demonstrating the goodness of fit of the histograms to idealized lognormal distributions. For each set of data, deciles are marked by grey-shaded circles, and the squared linear correlation coefficient, R^2, is indicated.

2.4.3 Distributions of ε_U and ε_T

The histograms of all ε_U and ε_T observations (Figure 2.5a,b) provide further insight into the discrepancies between the two datasets. The histograms have markedly different shapes despite being constructed from coincident sets of measurement. Most notably, the distribution of ε_T observations is nearly symmetric with only small negative skew (skewness, $s_g = -0.2$) in $\log_{10}$ space, while the ε_U distribution is skewed positive and more heavily ($s_g = 1.2$). Statistical properties that can be used to further compare the distributions are tabulated in Table 2.2 and indicated in Figure 2.5a,b. Of note are the larger geometric mean and median ε_U values, reflecting the relative absence of very small ε_U observations; the separation between the median and geometric mean of ε_U, reflecting the skewness of that distribution; and the wider interquartile range of ε_T, reflecting the larger variability of the ε_T observations.

The distributions may be further contrasted using a quantile-quantile (Q-Q) plot (Figure 2.5c) to quantify how similar each distribution is to an idealized lognormal one — the more linear the plot, the greater the similarity. From this visualization, it is clear that the distribution of ε_T observations can be described as lognormal over all ε except below the second decile (2×10^{-12} W kg^{-1}). In contrast, the distribution of ε_U observations

Table 2.2 – Statistical parameters of the ε_U and ε_T distributions shown in Figure 2.5. Given, from left to right, are the number, N, of observations; mode; geometric mean; median; first and third quartiles, P_{25} and P_{75}; arithmetic mean; and geometric standard deviation factor, σ_g. The quantities N and σ_g are dimensionless and unscaled. All other quantities are scaled by a factor of 10^{-11} W kg^{-1}.

	N	Mode	G. Mean	Median	P_{25}	P_{75}	A. Mean	σ_g
ε_U	28575	2.7	6.5	4.6	2.5	13	25	3.7
ε_T	21577	1.2	1.6	1.7	0.27	12	61	18.3

may be described as lognormal only above the seventh decile (1×10^{-10} W kg^{-1}). The strong positive curvature in the Q-Q plot for ε_U below the seventh decile indicates that there is substantially less weight on the left side of the observed distribution relative to an idealized lognormal one. The slight negative curvature in the Q-Q plot for ε_T below the second decile indicates a small trend in the opposite direction, i.e. a marginally heavier tail on left side relative to an idealized lognormal distribution. The squared linear correlation coefficients of the Q-Q plots are $R^2 = 0.917$ for ε_U and $R^2 = 0.995$ for ε_T, confirming the qualitative impression that the ε_U observations deviate more strongly from an idealized lognormal distribution.

We attribute the discrepancy in the shapes of the ε_U and ε_T histograms primarily to the sensitivity limit of the shear probes, which imposes an artificial lower limit (or "noise floor") on the ε_U observations. This noise floor will skew the histogram of ε_U observations positive by distributing samples that would otherwise be recorded as smaller values within a narrow range around the lower limit. Given the distinctive peak in the ε_U histogram and the extremely rapid rolloff to the left of the peak, we simply use the mode to approximate the noise floor as 3×10^{-11} W kg^{-1}. The ε_U observations that fall below this estimate of the noise floor are in the range $(1 \le \varepsilon_U < 3) \times 10^{-11}$ W kg^{-1} (Figure 2.5a); we attribute this statistical scatter to errors in the data processing which may, in part, arise because of uncertainty surrounding the characteristics of weakly turbulent, strongly stratified flows (Section 2.5.2). The range of values below the noise floor suggests uncertainty here within a factor of 3, implying that the effects of the noise floor begin to skew the ε_U distribution at $\sim 9 \times 10^{-11}$ W kg^{-1}. This is consistent with the trend in the Q-Q plot (Figure 2.5c) where the shape of the ε_U histogram begins to diverge from that of the ε_T histogram at dissipation rates below $\sim 1 \times 10^{-10}$ W kg^{-1}.

Previous studies using loosely-tethered profilers often cite a noise floor of O(10^{-10}) W kg^{-1} for shear-derived observations (e.g. Gregg, 1999; Wolk et al., 2002; Shroyer, 2012; Fer, 2014; Lincoln et al., 2016), though two glider-based studies that incorporated microstructure shear measurements both quote 5×10^{-11} W kg^{-1} for the noise floor (Wolk et al., 2009; Fer et al., 2014). The presence of an ε_U noise floor has practical ramifications for the interpretation of microstructure shear measurements; these are particularly important to consider in low energy environments, and we discuss them further in Section 2.5.4.

2.4.4 One-to-one comparison of ε_U and ε_T

A simple scatter plot of the coincident ε_U and ε_T observations (Figure 2.6) elucidates how the agreement between the two varies over the range of the observed dissipation rates. If one considers only observations where the two ε estimates are simultaneously greater than our empirical estimate of the ε_U noise floor (3×10^{-11} W kg^{-1}, Section 2.4.3), the agreement between the two sets of observations is encouraging. This subset of data is indicated in Figure 2.6 by the purple-shaded region. Here, the "cloud" of individual measurements largely scatters around the one-to-one line: 88% of these 8,064 observation pairs agree within a factor of 5, and 53% agree within a factor of 2. More importantly, the bin averages that are shown (defined below) always agree within a factor of 2. This level of agreement is consistent with the factor of 2 agreement in the mean vertical profiles (Figure 2.4) whenever those averages indicate $\varepsilon > 3 \times 10^{-11}$ W kg^{-1} in both estimates. Statistical agreement within a factor of 2 is comparable to the best agreement seen in other studies (e.g. Kocsis et al., 1999; Peterson and Fer, 2014).

When at least one of the ε estimates is less than 3×10^{-11} W kg^{-1}, statistical disagreement between the shear- and temperature-derived dissipation rates becomes concerning. Here, only 22% of the 16,842 observation pairs agree within a factor of 5, and only 6% agree within a factor of 2. The data diverge systematically from the one-to-one line: as the ε_T estimates continue to decrease, the ε_U estimates asymptote to a lower limit of approximately 2×10^{-11} W kg^{-1}, marginally below but still consistent with our estimate of the ε_U noise floor. The bin averages indicate the same pattern as the individual measurements: below $\varepsilon_T = 1 \times 10^{-11}$ W kg^{-1} they exhibit disagreement greater than a factor of 5, and, even in this averaged sense, suggest disagreement greater than two orders of magnitude when ε_T is less than 2×10^{-13} W kg^{-1}.

Note that averaged measures like bin averages are more appropriate than individual measurements when evaluating the agreement between ε estimates because we expect substantial statistical scatter (within about an order of magnitude) in these estimates. This scatter is, in part, attributed to uncertainties surrounding the validity of the isotropy, homogeneity, and stationarity assumptions inherent in the data processing (see Section 2.5.2). The bin averages shown in Figure 2.6 are averages calculated from the trimmed mean in logarithmically-spaced bins that lie perpendicular to the one-to-one line, i.e. in a coordinate system rotated 45° clockwise from that shown. Defining the bins in this manner helps minimize biases in the average by assuming roughly equal uncertainty in both variables, similar in principle to a bivariate least-squares minimization (Ricker,

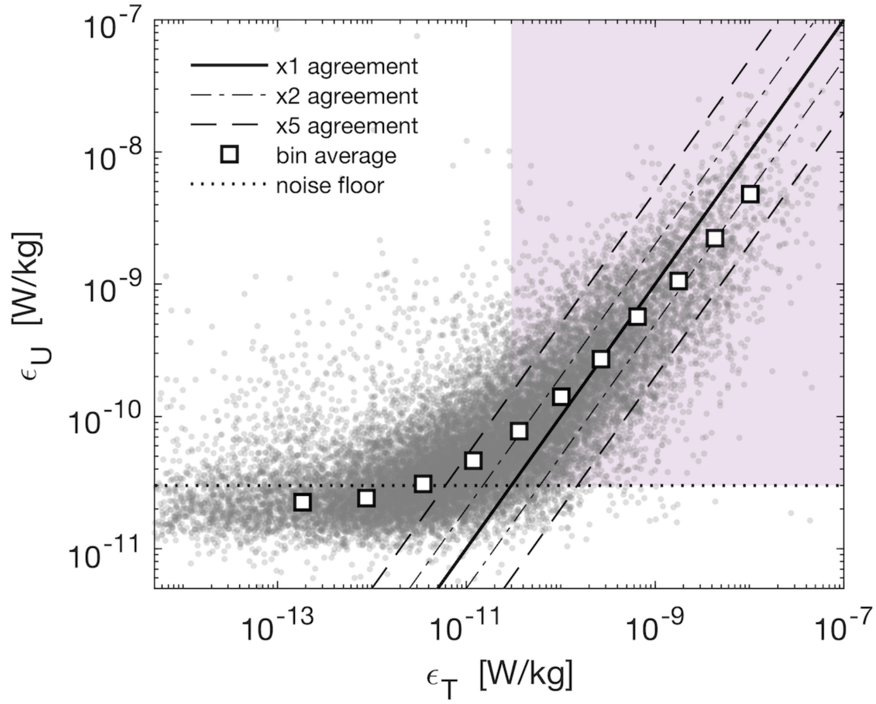

Figure 2.6 – Scatter plot comparison of the two coincident dissipation rate estimates ε_U and ε_T. Identical agreement and agreement within factors of 2 and 5 are indicated as labelled. Bin averages are calculated perpendicular to the one-to-one line (see text). Our empirical estimate of the ε_U noise floor (3×10^{-11} W kg^{-1}) is indicated by the horizontal dotted line. Purple shading indicates where both estimates of ε simultaneously lie above 3×10^{-11} W kg^{-1} and also delineates the region where bin averages agree within a factor of 2.

1973).

2.5 Discussion

Measuring turbulence parameters to estimate the turbulent dissipation rate comes with unique challenges in low energy environments like the Beaufort Sea, and our results in Section 2.4 demonstrate that the two most common means of directly estimating the dissipation rate can yield divergent results that disagree by multiple orders of magnitude at low ε. Our results suggest that most of this discrepancy can be attributed to the noise floor of the shear-derived estimates, but fundamental questions about the nature of marginally turbulent, strongly stratified flows also introduce uncertainty into the observations. And, more pragmatically, our results highlight questions about how to correctly process and interpret shear microstructure measurements in such environments since it appears that the majority (about 70%, Figure 2.5c) of ε_U estimates are skewed by the effects of the noise floor. We address these topics in the following discussion: in Section 2.5.1, we look more closely at the effect of sensor limitations on the measurements and the observed spectra; in Section 2.5.2 we discuss averaged observed spectral shapes;

in Section 2.5.3 we examine uncertainties that arise from the (potentially unjustified) assumptions needed for the processing of microstructure measurements; and in Section 2.5.4 we discuss practical implications, i.e. in which circumstances the difference between ε_U and ε_T matters and in which circumstances it can be safely ignored.

2.5.1 The Effect of Sensor Limitations

We propose that the systematic divergence between ε_U and ε_T that is obvious in Figures 2.5 and 2.6 at small dissipation rates is primarily a result of the effects of the noise floor of the ε_U estimates. This low-end divergence is then responsible for the large discrepancies seen in the spatial cross sections (Figures 2.2 and 2.3) and mean vertical profiles (Figure 2.4) of ε_U and ε_T. This interpretation is consistent with the known sensitivity limitations of microstructure shear probes (Osborn and Crawford, 1980) and previous empirical estimates of the ε_U noise floor (Section 2.4.3).

Assuming vibrations from the measurement platform do not contaminate the measured signal, the noise floor of an ε_U estimate is set by the lower limit of a shear probe's ability to detect hydrodynamic transverse forces and distinguish these from electronic measurement noise. Hydrodynamic forces from small-scale velocity shear below this detection limit may still act on the probe, but the signal is either not recorded or is masked by the instrument's electronic noise. As a result (Section 2.3.2), any variance $\left\langle(\partial u'/\partial x)^2\right\rangle$ that exists below the probe's detection limit will yield an ε_U estimate at (or near) the level of the noise floor, irrespective of what the true dissipation rate at the instant of the measurement may be. If the true dissipation rate is below the level of the noise floor in a large proportion of the measurement realizations, this behaviour will lead to an artificially skewed measurement distribution and a "pile-up" of observations against a lower limit, i.e. a distinct peak in the distribution near the noise floor and a rapid rolloff towards smaller—unresolved—values, as can be seen in the distribution of our ε_U observations (Figure 2.5a).

The manifestation of the noise floor can also be seen in the observed shear spectra when these are compared to the simultaneously observed temperature gradient spectra. Figure 2.7 depicts six representative pairs of observed shear and temperature gradient spectra, distributed over six consecutive orders of magnitude of ε (as suggested by the temperature-derived estimates). Each column of panels shows the two coincidently observed spectra $\Phi(k)$ and $\Psi(k)$, defined in Sections 2.3.2 and 2.3.3. Following panels g–l from right to left, the Batchelor fit to the temperature gradient spectra (Section 2.3.3) indicates continually decreasing ε_T, as labelled in each panel. The shear spectra indicate a similar ε-trend over the four larger orders of magnitude (panels c–f): as anticipated, the peak of the observed shear spectrum moves downwards and to the left as ε decreases,

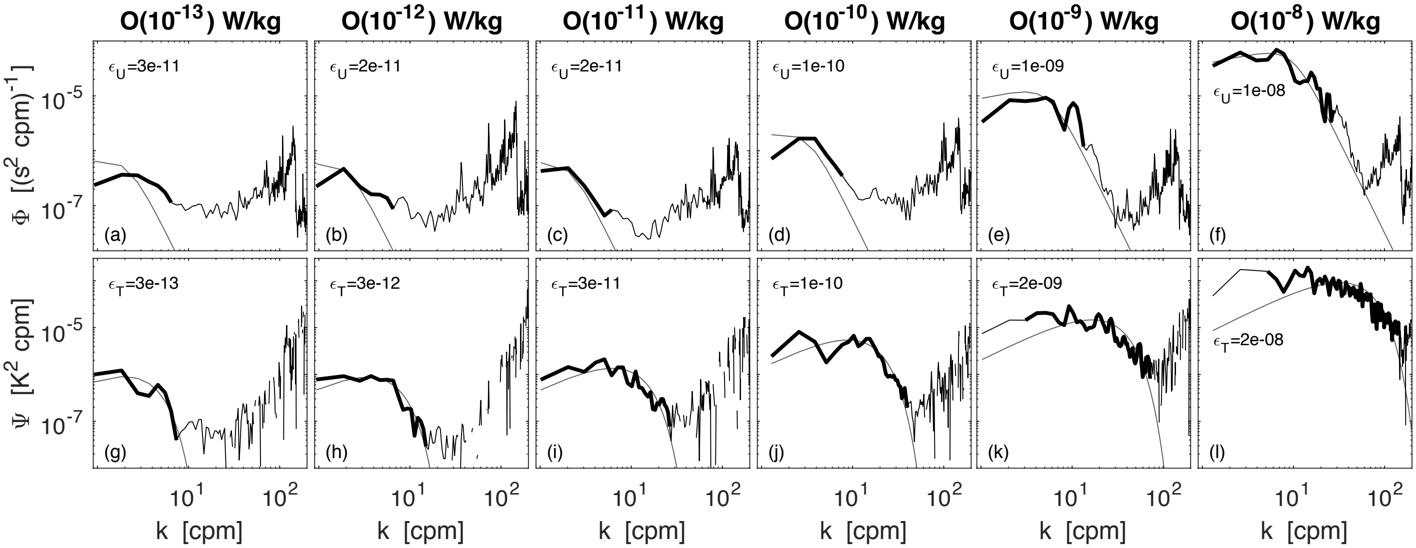

Figure 2.7 – Sample coincident shear (a-f: Φ) and temperature gradient (g-l: Ψ) spectra (black) for 6 orders of magnitude of ε, as determined by the temperature measurements. Bold indicates the wavenumbers explicitly included for integration; the remaining variance is estimated as described in Sections 2.3.2 and 2.3.3. For Ψ, bold also indicates the wavenumber range used for the MLE Batchelor fit (see Section 2.3.3).Shear spectra have the accelerometer signal removed (Section 2.3.2) and temperature gradient spectra have the empirically-determined noise spectra removed (Section 2.3.3). Nasmyth (a-f) and Batchelor (g-l) reference spectra (grey) are also drawn. Batchelor spectra are those determined by the MLE fitting algorithm which are used to estimate k_B (Section 2.3.3).

and the integral of the spectrum (Section 2.3.2) indicates decreasing ε_U, as labelled. However, below O(10^{-11}) W kg^{-1} (panels a–b) the spectrum runs into a spectral "floor" and does not decrease any further. Here, the integral of $\Phi(k)$ no longer reflects the shear variance or any true physical quantity; instead, it saturates at a lower limit that indicates the available precision of ε_U, which, as anticipated, is in the vicinity of our empirical estimate of the noise floor 3×10^{-11} W kg^{-1} (Section 2.4.3).

So far, we have focused our discussion on limitations of the shear measurements. Of course limitations also exist on the measurement of temperature microstructure, but these are of a different nature than those which affect the shear measurements, and they tend to be less problematic in our study. Sensitivity limitations are not a concern for microstructure thermistors in the way they are for shear probes since the FP07 thermistors easily respond to within better than 0.1 mK (Sommer et al., 2013b) which is approximately the smallest temperature scale we need observe (e.g. Figure 2.7g). The relatively slow time response of thermistors is generally a concern (Gregg, 1999), but at small dissipation rates it is possible to adequately account for the slow response using the transfer function proposed by Sommer et al. (2013b) or a similar correction method. At rates greater than $\sim 1 \times 10^{-7}$ W kg^{-1}, the effects of the slow response time can no longer be adequately corrected and temperature-derived estimates will tend to systematically underestimate the true dissipation rate (Peterson and Fer, 2014), but this limitation is not a concern in our observations since fewer than 0.1% of our ε_T estimates are above this cutoff value. A more relevant concern for our temperature-derived estimates is the potential uncertainty that surrounds the characteristics of turbulent eddies and the resulting turbulence spectra when turbulent energetics are weak and stratification is strong, as is the case in the setting for our measurements. This is the topic of the following two sections.

2.5.2 Turbulence Spectra in Stratified Low Energy Flows

Our observations suggest that the shape of shear and temperature gradient spectra deviate systematically from Nasmyth and Batchelor reference spectra in stratified low energy flows. Fitted Nasmyth and Batchelor spectra are drawn with the selected observed spectra in Figure 2.7 for reference, exemplifying varying levels of agreement; however, individual observed spectra have limited utility for providing broader physical insight because we anticipate naturally occurring variability in the shapes of individual spectra (e.g. Fer et al., 2014). In order to identify systematic trends in the shapes of turbulence spectra, we bin all observed spectra by buoyancy Reynolds number, $Re_B = \varepsilon/\nu N^2$, and calculate median temperature gradient and shear spectra in each bin (Figure 2.8). The Re_B parameter quantifies the destabilizing effects of turbulent kinetics relative to the stabilizing effects of stratification and viscosity. It is proportional to the ratio of the largest vertical (Ozmidov) scale to the smallest isotropic (Kolmogorov) scale of turbulent eddies, so when $Re_B < 1$ we anticipate that turbulent eddies of all sizes, including the smallest ones on dissipative scales, are modified by stratification and exhibit a degree of anisotropy. Further, modelling results suggest that the characteristics of turbulent structures undergo regime shifts in the vicinity of $Re_B \sim 10$ and $Re_B \sim 100$ (Shih et al., 2005; Ivey et al., 2008), and so combining with the above scaling argument, we use 1, 10, and 100 to delineate the boundaries of our Re_B bins.

To calculate median spectra, individual spectra must first be normalized identically so that the shapes of spectra over varying ε and χ may be compared. To do this, we nondimensionalize shear spectra using

$$\Phi^* = \Phi/(\varepsilon_U^3/\nu)^{1/4} \tag{2.8}$$

and temperature gradient spectra using

$$\Psi^* = \Psi/\left(\frac{\chi\sqrt{q_B/2}}{k_B\kappa_T^{\mathrm{mol}}}\right), \tag{2.9}$$

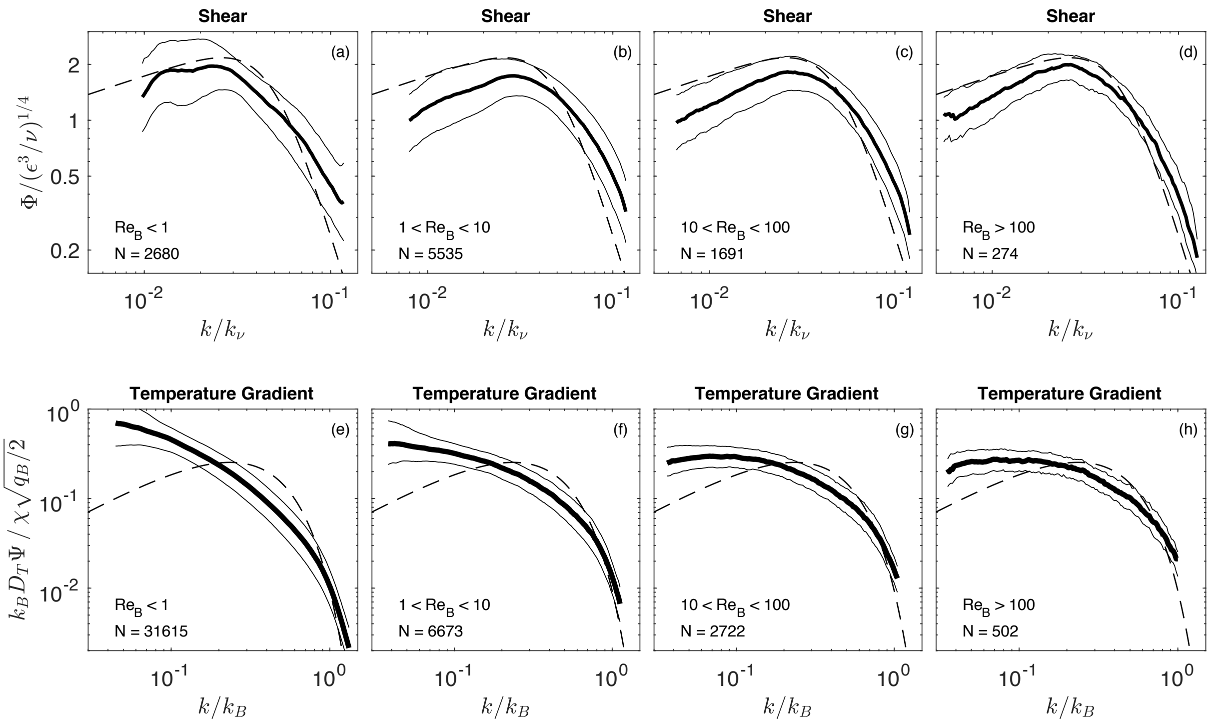

Figure 2.8 – Median nondimensionalized shear (a-d) and temperature gradient (e-h) spectra in bold, for regimes of Re_B as indicated. Also shown are the 25th and 75 percentile of data (thin solid line) as well as nondimensionalized reference spectra (dashed line): Nasmyth for shear and Batchelor for temperature gradient. The total number of spectra used in each calculation is indicated by N. Shear spectra with $\varepsilon_U < 10^{-10}$ W kg^{-1} are excluded.

consistent with schemes used by Oakey (1982) and Dillon and Caldwell (1980). We nondimensionalize wavenumbers using k/k_ν for shear spectra and k/k_B for temperature gradient spectra. The scaling factor k_ν is the Kolmogorov wavenumber defined $(1/2\pi)(\varepsilon_U/\nu^3)^{1/4}$; the remaining variable definitions for Equations 2.8 and 2.9 are given in Section 2.3. For each Re_B bin, we then calculate the median spectral height at each nondimensional wavenumber using all spectra within the bin, creating the median spectra shown in Figure 2.8; we also calculate the interquartile range at each nondimensional wavenumber as a measure of the variability around the median. To exclude artificial effects that may arise because of the ε_U noise floor (Section 2.5.1), we exclude from the calculations any shear spectra where $\varepsilon_U < 1 \times 10^{-10}$ W kg^{-1}.

The systematic modification of the temperature gradient spectra with decreasing Re_B is clearly visible if one follows panels e–h from right to left: there is a clear trend towards less curvature and greater low-wavenumber deviation from the theoretical curve as Re_B decreases. None of the median temperature gradient spectra exhibit a curvature as strong as that predicted by the Batchelor spectrum, but the discrepancy increases with decreasing Re_B, and for the two lowest Re_B bins there is no longer a peak and rolloff delineating distinctive subranges of the spectrum. This behaviour is similar to that seen in measurements taken by Dillon and Caldwell (1980) who, as we do, observed decreasing curvature with smaller turbulence intensities.

The median shear spectra likewise vary systematically with Re_B, indicating increasing deviations from the Nasmyth spectrum as Re_B becomes small (following panels a–d from right to left). The dissipative subrange, to the right of the peak, is not as steep in any of the median spectra as predicted by the Nasmyth shape, and it becomes increasingly more shallow with decreasing Re_B. In addition, the amplitude of the spectrum in the inertial subrange, left of the peak, is overestimated by the Nasmyth spectrum in all median spectra and no longer appears to be well described by a simple power law when $Re_B < 1$. This behaviour is reminiscent of that seen in measurements by Gargett et al. (1984) who found that inertial subranges of shear spectra gradually disappeared when turbulence became weak and stratification became strong.

2.5.3 Understanding Uncertainty for Small ε

The above discussion (Section 2.5.2) highlights the manner in which turbulence spectra are systematically modified away from their reference shapes as Re_B becomes small. We propose that the systematic modification with decreasing Re_B occurs as the characteristics of turbulent eddies in strong stratification increasingly depart from the idealized framework of steady, isotropic turbulence. Evidence for this behaviour can be seen in the distribution of the Re_B parameter which is below unity in 76% of our observations, suggesting that turbulent eddies are frequently anisotropic and modified by the effects of stratification. Further, the Ozmidov scale, $L_O = (1/2\pi)(\varepsilon/N^3)^{1/2}$, has a median value of 0.1 cm, which is exceptionally small and again suggests that even viscous-scale eddies are squashed by the stratification.

These characteristics signal that there is increased uncertainty in the dissipation rate estimates when ε is small and N^2 is large. This is especially true for ε_T estimates where the data processing depends on the ability to determine k_B from Batchelor spectrum fits (Section 2.3.3). One way to characterize the increased uncertainty is to quantify the degree by which observed turbulence spectra and idealized reference spectra diverge. We do this here for the temperature measurements and compare temperature gradient spectra to Batchelor spectra by calculating for each spectrum the root-mean-square error, ξ_{rms}, of $\log_{10}(\Psi/\Psi_{\mathrm{B}})$, defined:

$$\xi_{\mathrm{rms}} = \sqrt{\frac{1}{n}\sum_{i=1}^{n}\log_{10}^{2}\left(\frac{\Psi_i}{\Psi_{\mathrm{B}i}}\right)} = \sqrt{\frac{1}{n}\sum_{i=1}^{n}\left[\log_{10}(\Psi_i) - \log_{10}(\Psi_{\mathrm{B}i})\right]^2}. \tag{2.10}$$

The summation index i runs over all wavenumbers included in the Batchelor fitting

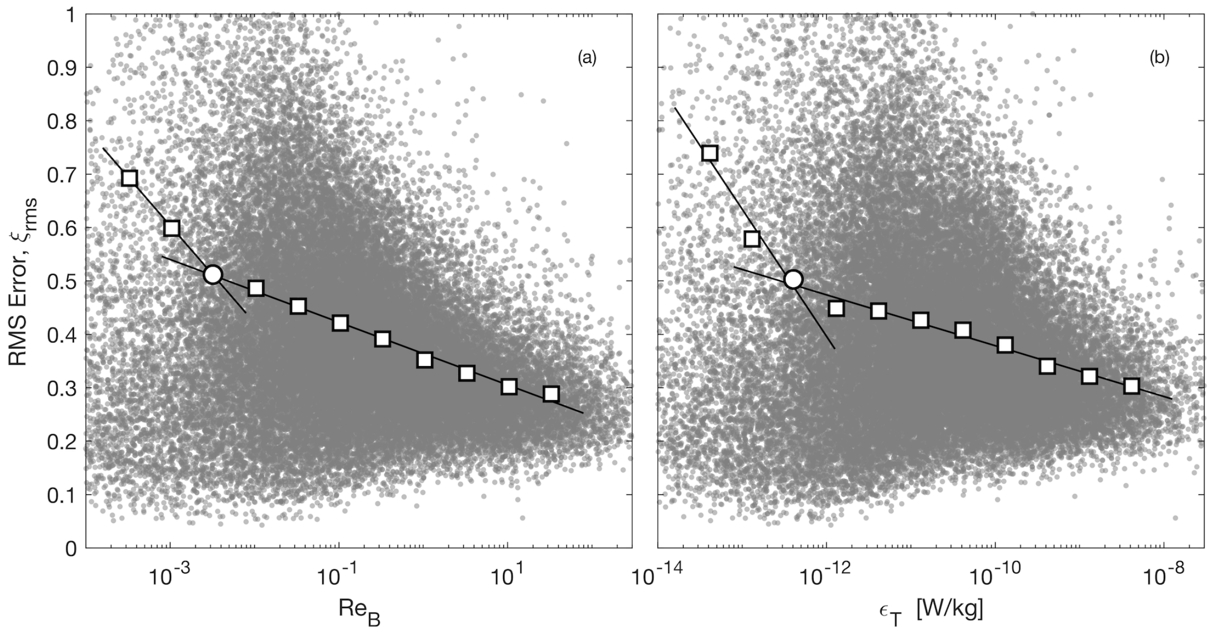

Figure 2.9 – Root-mean-square error between Ψ and Ψ_B, as defined in the text, visualized as a function of (a) buoyancy Reynolds number, and (b) dissipation rate. It quantifies the degree of divergence between observed temperature gradient and theoretical Batchelor spectra. Large open faced markers are bin averages. Regressions to subsets of the bin averages are shown in each panel; the subsets are those on either side of the datum marked by the circle (inclusive).

procedure; n is the number of spectral points included in the fit (Section 2.3.3). We find that averages of ξ_{rms} increase gradually from 0.3 to 0.5 as Re_B estimates decrease from O(10^1) to O(10^{-2}); at smaller Re_B, mean ξ_{rms} increases rapidly to a maximum value of 0.7 (Figure 2.9). A similar, but more pronounced, pattern is visible when ξ_{rms} is visualized as a function of ε_T. The increase in ξ_{rms} is gradual and modest, from 0.3 to 0.45, as ε_T decreases from O(10^{-7}) W kg^{-1} to O(10^{-12}) W kg^{-1}; this behaviour is followed by a sharp increase in ξ_{rms} at smaller ε_T.

Further insight into the confidence of the ε_T values can be gained empirically if we make the assumption that dissipation rates distribute lognormally in the ocean (Baker and Gibson, 1987; Gregg, 1987). Under this assumption, we can use the observed distribution of ε_T (Figure 2.5b) to estimate a lower cutoff below which the application of the steady, isotropic turbulence model becomes problematic and ε_T estimates become unreliable. The distribution of ε_T observations follows the lognormal shape closely over the entire range of data except below the second decile (Figure 2.5c), where the observed distribution is disproportionately heavy. The distortion in the distribution indicates that uncertainties in the data processing statistically skew the ε_T estimates below the second decile; our simple statistical model therefore suggests that the ε_T estimates are reliable and physically meaningful to values as small as $\varepsilon_T \approx 2 \times 10^{-12}$ W kg^{-1}. Below this cutoff, ε_T estimates are unreliable and perhaps not meaningful. Note that a lower cutoff

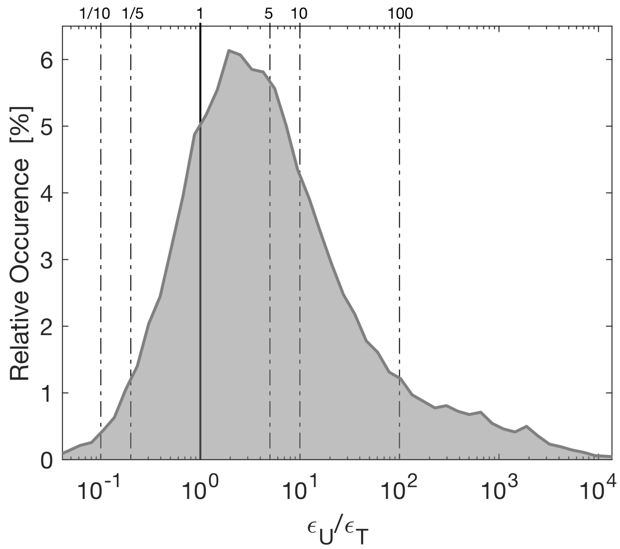

Figure 2.10 – Histogram of the ratio $\varepsilon_U/\varepsilon_T$, highlighting the large number of coincident measurements where the shear-derived values overestimated the temperature-derived ones in our dataset. Agreement by factors of 5, 10, and 100 is indicated by dashed lines. The histogram is calculated over 50 logarithmically spaced bins.

of 2×10^{-12} W kg^{-1} is consistent with the sudden increase in ξ_{rms} that occurs in Figure 2.9b below $\varepsilon_T = O(10^{-12})$ W kg^{-1}.

2.5.4 Implications for Interpreting Microstructure Measurements

In Section 2.4 we demonstrated that there can be a significant difference between dissipation rate estimates derived from coincident measurements of shear and temperature microstructure. The ε_T estimates suggest that the true dissipation rate is below the ε_U noise floor of 3×10^{-11} W kg^{-1} in 58% of our observations. A histogram of the ratio $\varepsilon_U/\varepsilon_T$ (Figure 2.10) demonstrates the severity and the frequency with which the shear probes may overestimate the dissipation rate in low energy environments like the Beaufort Sea. Using ε_T as a reference (and acknowledging the associated uncertainties described in Section 2.5.3), the shear measurements overestimate the dissipation rate by a factor of at least five in 44% of our measurements, by at least one order of magnitude in 31% of our measurements, and by at least two orders of magnitude in 9% of our measurements. This is a level of error that has the potential to alter the interpretation of the shear measurements, as described in the following paragraph. In contrast, the temperature measurements overestimate the dissipation rate relative to ε_U by a factor of at least five in less than 3% of measurements, a degree of mismatch that could safely be neglected in many applications.

The severity with which the bias we found in the shear measurements may alter the interpretation of ε_U estimates depends on the specific goals of a study. If, as in Section

2.4, the utility of the measurements is to characterize the variability and the statistical distribution of dissipation rates, then the potential for biases greater than an order of magnitude cannot be ignored. Without the coincident ε_T estimates to which to compare, the ε_U estimates would lead us to misrepresent the degree of spatial variability (Figures 2.2–2.3), the geometric averages representing "typical" values (Figure 2.4), and the observed distribution and related statistics (Figure 2.5, Table 2.2) of the turbulent dissipation rate here in the Amundsen Gulf. These misrepresentations may then be further propagated into calculations of the mixing rate coefficient K_ρ, which typically rely on the Osborn (1980) model $K_\rho = 0.2\varepsilon/N^2$, leading to similar misrepresentations of the variability, the geometric averages representing typical values, and the distribution and related statistics of K_ρ.

Arithmetic mean values of ε_U, however, are much less sensitive to the bias we describe. This is fortunate, because arithmetic mean values are arguably the appropriate measure to use when estimating bulk buoyancy fluxes and characterizing net water mass transformation from mixing rate estimates (Baker and Gibson, 1987). As noted in Section 2.4, in this study we have tended to use the geometric mean to average dissipation rates. We do this because the geometric mean effectively characterizes the central tendency of lognormally distributed data and more fairly represents "typical" ε realizations (Kirkwood, 1979). In contrast, the arithmetic mean is ineffective at representing typical values of a lognormal-like distribution because it is dominated by a small number of very large values at the high end of the distribution. Further, the arithmetic mean tends to be very sensitive to individual outliers that may exist on the far right-hand-side of the distribution, but this may be problematic because of the large uncertainty in individual ε realizations. However, the disproportionate importance of large values in setting the arithmetic mean also makes it mostly insensitive to errors in small ε estimates. The effect can be seen, for example, when comparing the arithmetic mean of the ε_U and ε_T distributions (Figure 2.5, Table 2.2): in contrast to the geometric mean, the median, and the 25th and 75th percentiles, the arithmetic mean of the ε_T distribution is *greater* than that of the ε_U distribution because of a marginally thicker tail on the right-hand-side of its distribution which more strongly influences its arithmetic mean.

A final subtle point remains to be discussed. When carrying out an analysis using microstructure measurements of shear, it is tempting to simply remove observed ε_U values that sit at or near the estimated noise floor, discarding these as untrustworthy. This approach is viable when only a small number of the observations are near the noise floor; however, in the present study, simply removing data likely to be corrupted by the effects of the noise floor would only exacerbate the bias evident in the ε_U observations. For example, if we remove from the dataset the shear-derived estimates where $\varepsilon_U < 5 \times 10^{-11}$ W kg^{-1}, we increase the positive bias in our sample by removing 53% of the measurements and the entire left half of the ε_U histogram (Figure 2.5). Rather than helping to correct biased averages of ε_U, this change shifts the median from 4.6×10^{-11} to 1.4×10^{-10} W kg^{-1} and the geometric mean from 6.5×10^{-11} to 1.9×10^{-10} W kg^{-1}, in both cases increasing the error in these averaging metrics.

The best practical way to account for the effects of the noise floor in microstructure shear measurements will depend on the goals of each individual study and on the proportion of the observations that are in the vicinity of the noise floor. One approach is to set dissipation rates that appear to be near the noise floor to zero (e.g. see Gregg et al., 2012); this approach is probably justifiable for arithmetic mean calculations since the averaging is dominated by the large ε values, but it is problematic when describing the variability or when calculating a geometric mean to characterize typical ε values. In these situations, it may be more appropriate to fit a lognormal distribution to the part of the observed distribution that resides above the noise floor, but care is required here also since the theoretical conditions for expecting lognormality are strict and often not satisfied in a set of field measurements (Yamazaki and Lueck, 1990). In any case, it is clear that the interpretation of microstructure shear-derived dissipation rate estimates should proceed with caution if the measurements are from a very low energy environment and it appears that a large proportion of the data cluster around a well defined noise floor.

2.6 Conclusions

Care must be taken to understand how measurement limitations may bias microstructure measurements in low energy environments like the Beaufort Sea: this is the central theme of our study. The results we have presented here suggest that microstructure measurements of velocity shear, in particular, are prone to misrepresenting averaged dissipation rates—and, consequently, mixing rates—in such environments because the noise floor of the ε_U estimates artificially biases the majority of the observations. In addition, our measurements suggest that both shear- and temperature-derived dissipation rate estimates may be complicated by further uncertainty when strong stratification modifies the characteristics of turbulence in a weakly energetic, strongly stratified flow; this change in the characteristics can be seen in the systematic modification of the shapes of shear and temperature gradient spectra at low Re_B.

We have documented the discrepancy between the two distinct dissipation rate estimates ε_U and ε_T because we find disagreement large enough to lead to substantial differences in how the two sets of data would be interpreted independently. The temperature-derived estimates were able to resolve smaller dissipation rates than the shear-derived estimates: averages of ε_U began to exhibit biased behaviour below 10^{-10} W kg^{-1} and were not able to resolve rates below 3×10^{-11} W kg^{-1}, while averages of ε_T were reliable to values as low as 2×10^{-12} W kg^{-1} and were characterized by unacceptably large uncertainty below this. Our experience suggests that caution interpreting shear-derived dissipation rate estimates is warranted if a large number of observations cluster at or near an identifiable ε_U noise floor, in our case 3×10^{-11} W kg^{-1}. In the measurements presented here, the temperature-derived estimates suggest that the true dissipation rate lies below this noise floor often enough to fundamentally alter the scientific interpretation of the measurements. Other low energy environments in which the special measurement considerations outlined in this study may be applicable include the wider Canada Basin (Rainville and Winsor, 2008), stratified lakes (Sommer et al., 2013a; Scheifele et al., 2014), the central Baltic Sea (Holtermann et al., 2017), and the abyssal global ocean over smooth topography (Waterhouse et al., 2014).

Chapter 3

Turbulence and Mixing in the Arctic Ocean's Amundsen Gulf

3.1 Introduction

In this study, we present observations of ocean turbulence and mixing in the Beaufort Sea's Amundsen Gulf (Figure 3.1) from a series of CTD and microstructure measurements we collected in summer 2015. Amundsen Gulf is one of the most biologically productive regions of the Arctic Ocean (e.g. Stirling, 1980, 2002; Harwood and Stirling, 1992; Dickson and Gilchrist, 2002; Geoffroy et al., 2011), but modern climate change is rapidly driving the western Arctic to a "new normal" state, and perturbations to regional ecosystem dynamics and services are already being observed (Post et al., 2009; Serreze and Barry, 2011; Jeffries et al., 2013). In light of ongoing changes to the broader physical environment, it is important that the science community continue developing a detailed understanding of the physical oceanography—and in particular of the mixing characteristics—of the western Arctic in order to facilitate studies that will model the environmental and ecological responses to future regional climate change (e.g. Carmack and MacDonald, 2002; Rainville et al., 2011; Carmack et al., 2015).

The Arctic Ocean is probably the most under-sampled of the major ocean basins with respect to mixing (e.g. Waterhouse et al., 2014), and observations of ocean turbulence are notably scarce in the Beaufort Sea. A number of studies over the previous decade have deepened our understanding of mixing rates and mechanisms in the broader Canada Basin (e.g. Rainville and Winsor, 2008; Timmermans et al., 2008a,b; Guthrie et al., 2013; Dosser et al., 2014; Shaw and Stanton, 2014), but, to our knowledge, only four previous studies (Padman and Dillon, 1987; Bourgault et al., 2011; Rippeth et al., 2015; Lincoln et al., 2016) have used microstructure measurements to characterize mixing

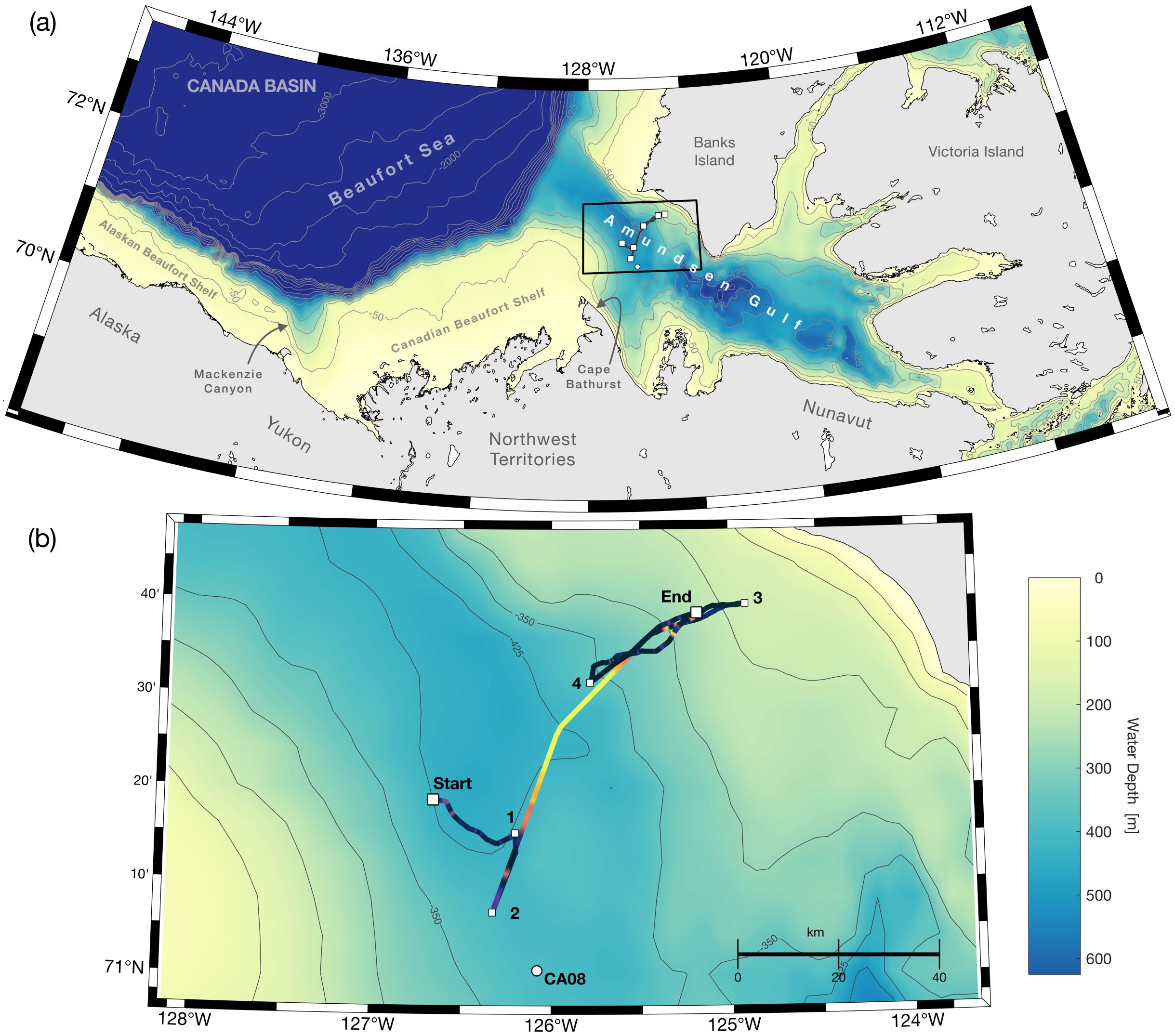

Figure 3.1 – (a) Map of the southeastern Beaufort Sea, showing the location of Amundsen Gulf to the east of the Canadian Beaufort Shelf. The glider path is shown by the thin black line inside the black rectangle. (b) Enlarged view of the region given by the black rectangle in panel (a), showing the path of the glider. The start and end locations of the track are shown by the large white rectangles; four intermediate waypoints are shown by the small white rectangles and numbered consecutively. The color on the glider's track-line is water temperature along the 1026.15 kg m^{-3} isopycnal, using the same colour scale as shown in Figure 3.11, indicating the location and spatial scale of the warm-core eddy discussed in the text (Section 3.5.3). The white circle is the location of ArcticNet mooring CA08. Bathymetry data are from IBCAO 3.0 (Jakobsson et al., 2012).

rates in the Beaufort Sea directly. This scarcity of direct observations limits our understanding of the role of turbulent mixing in the Beaufort Sea because a large number of tightly resolved measurements is needed to accurately characterize turbulence, which tends to be described with lognormally distributed variables that are easily undersampled (Baker and Gibson, 1987; Gregg, 1987). As a result, there remains a pressing need to continue building a broad record of mixing estimates in order to understand current and future basin-scale water mass transformations across the western Arctic (Carmack et al., 2015).

With this study, we contribute to a more comprehensive understanding of the physical environment that underpins the ecology of the southeastern Beaufort Sea by providing a detailed description of the turbulence and mixing characteristics of the region. Using an autonomous ocean glider equipped with a CTD and turbulence sensors, we measure the hydrography and turbulent dissipation rates of kinetic energy and thermal variance and use these measurements to statistically characterize diapycnal mixing rates and heat fluxes. We then discuss the relative importance of tidal mixing, double diffusion, and near-surface mesoscale and smaller processes that may underpin the observed turbulence environment. To our knowledge, this is the first time such a broad characterization of mixing from direct turbulence measurements has been presented for this region and the first time an autonomous instrument has been used to characterize the statistics of turbulence and mixing in the Beaufort Sea.

The remainder of the chapter is structured as follows. In Section 3.2, we describe the CTD and microstructure measurements from the glider and briefly outline the data processing methods. Section 3.3 uses the CTD measurements to describe the relevant hydrographic context. In Section 3.4, we present the primary results of this study, the turbulence, mixing rate, and heat flux observations. Section 3.5 presents a discussion of relevant mixing mechanisms. We synthesize our results in Section 3.6.

3.2 Measurements and Data Processing

3.2.1 Sampling Strategy

We collected CTD and turbulence measurements in Amundsen Gulf using an autonomous 1000-m-rated Teledyne-Webb Slocum G2 ocean glider, fitted with (1) an internally mounted, pumped Seabird CTD measuring conductivity, temperature, and pressure, and (2) an externally mounted turbulence-sensing package measuring shear and temperature microstructure (Section 3.2.2). The measurements used in this study are those first described in Chapter 2, collected continuously over 11 days during the period 25 August –

5 September, 2015.

The 186 km horizontal path of the glider, immediately northwest of the basin sill, is shown in Figure 3.1. The glider spent the first 5 days in the central Gulf, where the water depth exceeds 400 m, and the remaining time on three traverses of the continental shelf near Banks Island. Along this path, the glider collected 348 discrete quasi-vertical measurement profiles, at a nominal glide angle of 26° from the horizontal. The first 112 profiles, in water ∼410 m deep, extend from the near surface to a fixed depth of 300 m; later profiles typically extend to within 15 m of the local bottom, which ranged between 205–430 m depth. The location of each profile is approximated with its mean coordinates, neglecting horizontal translation that occurs over the course of one profile. The mean (standard deviation) distance between consecutive profiles is 536 (357) m.

3.2.2 Turbulence Measurements and Data Processing

The glider carried an externally mounted, self-contained microstructure sensing package known as a *Microrider*, also used in recent studies by Fer et al. (2014), Peterson and Fer (2014), Palmer et al. (2015), and Schultze et al. (2017). The Microrider is manufactured by Rockland Scientific and is factory-installed on the glider. Our configuration of the Microrider had two velocity shear probes and two fast response thermistors, each sampling at 512 Hz, measuring velocity and temperature gradients on scales smaller than 1 cm. All sensors sampled continuously during the deployment, but one of the two shear probes failed after the first three days of measurement.

We derive independent estimates of the turbulent kinetic energy (TKE) dissipation rate, ε, from each of the four microstructure channels. This rate is a measure of how turbulent a flow is and is proportional to the rate of diapycnal mixing in the Osborn (1980) model. We briefly outline below our methodologies to derive ε from the shear and temperature microstructure measurements; a more detailed description of the methods and their limitations is given in Chapter 2.

We calculate the TKE dissipation rate from the measured microstructure shear variance according to

$$\varepsilon_U = 7.5\nu \left\langle \left(\frac{\partial u'}{\partial x} \right)^2 \right\rangle \quad , \tag{3.1}$$

where $\partial u'/\partial x$ is a turbulent-scale shear component measured along the glider's along-path coordinate, x, and ν is the kinematic viscosity of seawater. Angled brackets indicate ensemble averaging, and the subscript $_U$ indicates that this is a shear-derived dissipation rate estimate. We use half-overlapping 40-s segments of measurement to calculate successive ε_U estimates; within each of these segments, we calculate and average 19 shear power spectra from consecutive half-overlapping 4-s subsegments and integrate to obtain the shear variance in the segment. The spatial length encompassed by each 4-s subsegment depends on the glider's speed and has a mean (standard deviation) of 163 cm (15 cm) for upcasts and 100 cm (15 cm) for downcasts.

We calculate the TKE dissipation rate from the temperature microstructure measurements using power spectra of temperature gradient variance, calculated over the same 40-s segments and 4-s subsegments that we used to calculate the shear spectra. We fit a theoretical form for the temperature gradient spectrum—the Batchelor spectrum—to the observed gradient power spectrum using the maximum likelihood estimator method proposed by Ruddick et al. (2000) and later modified by Steinbuck et al. (2009). In this procedure, ε is a variable fitting parameter that is optimized by minimizing the difference between the observed and theoretical spectra (the full procedure is detailed in Section 2.3.3). We refer to this optimized value as ε_T, with the subscript $_T$ indicating a temperature gradient-derived dissipation rate estimate.

Both, ε_U and ε_T estimates, are then subjected to a series of quality control criteria that remove suspect estimates. These routines are designed to flag and remove values where, for example, the glider's flight was not steady, shear probes contacted small marine organisms or debris, Taylor's frozen turbulence hypothesis is violated in the calculation of power spectra, etc. They are detailed in Appendix A.1. Quality control removes 22% of ε_U and 34% of ε_T estimates.

Finally, dual estimates of ε from each set of probes are arithmetically averaged to obtain single ε_U and ε_T values for each 40-s segment. The resulting ε_U and ε_T estimates are combined into a single best ε estimate using the following method. When $\varepsilon_U \geq 1 \times 10^{-10}$ W kg^{-1}, we keep only ε_U because the shear-derived estimate relies more directly on the definition of the dissipation rate and is more reliable in energetic conditions (Gregg, 1999). However, if the ε_U estimate is unavailable because it failed quality control, we keep the coincident ε_T estimate instead, if this is available. If both are available, but they differ by more than a factor of 10, both are discarded. Below 1×10^{-10} W kg^{-1}, ε_U begins to be statistically biased by the noise floor of the shear measurement and is no longer reliable (Chapter 2); for these measurements, we keep only ε_T. However, when $\varepsilon_T < 2 \times 10^{-12}$ W kg^{-1}, this estimate is also no longer reliable (Chapter 2), and we set ε to zero, following the approach used by Gregg et al. (2012). We are left with 22,153 unique ε estimates for the remaining analysis; of these, 4,699 (or 21%) are set to zero.

3.2.3 Arithmetic vs. Geometric Averaging

Turbulence in the ocean is patchy in space and intermittent in time, and the distributions of dissipation rates and mixing coefficients are typically lognormal-like, spanning many orders of magnitude (Baker and Gibson, 1987). Arithmetic and geometric mean values may differ by orders of magnitude in such data, so it is important to distinguish between the two and recognize their distinct physical interpretations (Kirkwood, 1979). Geometric averaging characterizes the central tendency of a lognormally distributed variable, giving a measure of a "typical value" of the distribution. Arithmetic averaging characterizes the integrated cumulative effect of a turbulent process and is disproportionately skewed by a small number of large values on the right-hand side of the distribution. For example, while a geometric mean mixing rate represents a "typical" mixing rate in a well-resolved series of observations, the arithmetic mean rate will more accurately characterize net buoyancy transformations produced by mixing in those observations. We present both geometric and arithmetic mean values throughout this study, as appropriate.

3.3 Hydrography

In Figure 3.2, we present conservative temperature, T, and squared buoyancy frequency, N^2, fields derived from the CTD measurements; for each field, a mean vertical profile and a spatial cross section are shown. The horizontal coordinate in the cross sections is the glider's along-track distance coordinate, s, measured along the two-dimensional track shown in Figure 3.1b. To guide the eye, each cross section is broken into multiple panels at waypoints where the glider changed its direction of travel.

We identify five distinct hydrographic layers, similar to those used to describe layering in the Canada Basin. From shallowest to deepest, these are a warm surface mixed layer (SML); a strongly stratified near-surface "cold halocline" (CH); a cold Pacific Water (PW) layer with water sourced at Bering Strait; an intermediate "warm halocline" (WH) where temperature increases with depth; and a warm Atlantic Water (AW) layer with water sourced from the Atlantic Ocean. We define the boundaries of the layers using their absolute salinity, S_{A}, characteristics, similar to Carmack et al. (1989); the boundaries and hydrographic characteristics of the layers are summarized in Table 3.1. The layering can be seen most easily in the temperature cross section (Figure 3.2a).

Three points about the hydrography stand out as noteworthy for the purposes of this study. First, the amount of heat sequestered below the warm halocline in the warm AW layer is substantial: in the central Gulf, where the water depth is $\sim$425 m, and the AW

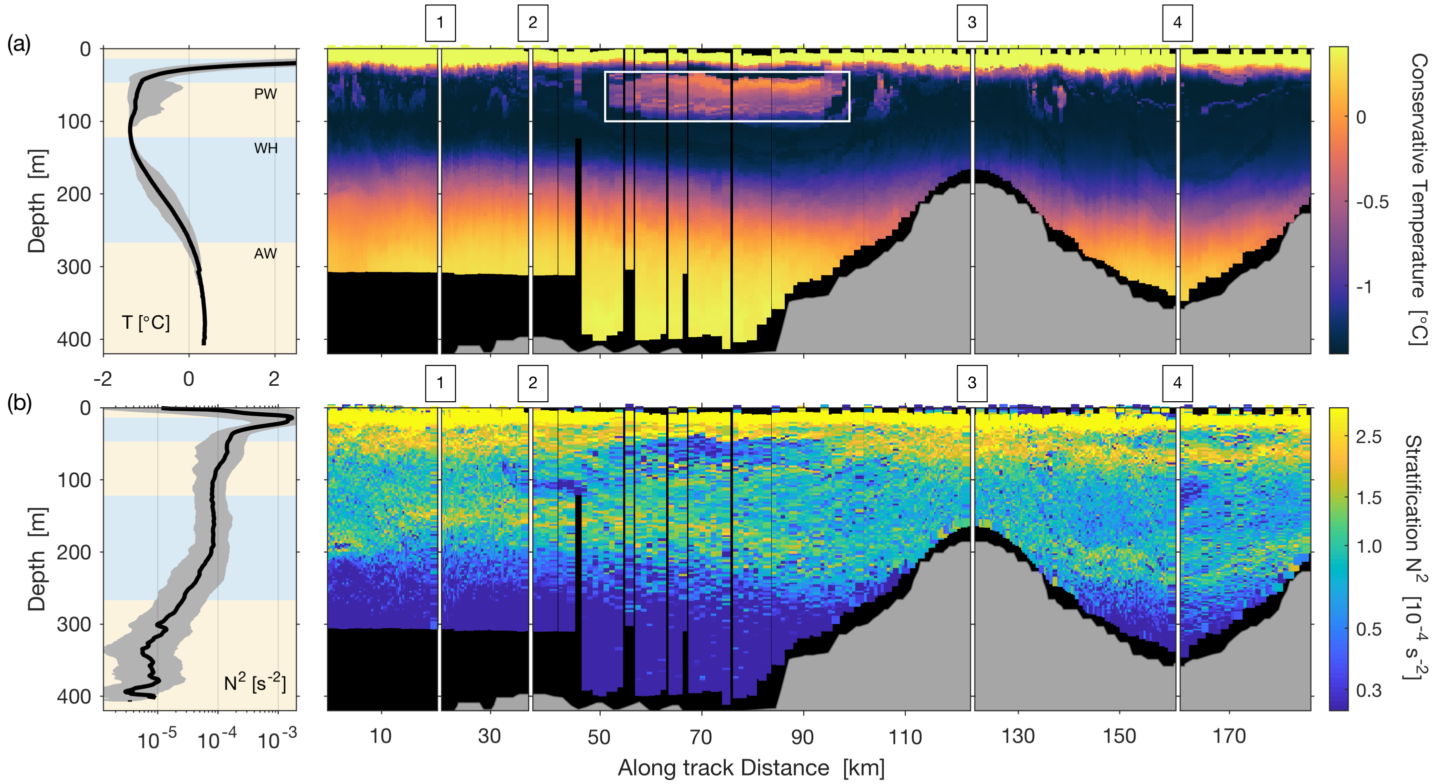

Figure 3.2 – (a) Arithmetic mean profile and spatial cross section of conservative temperature. (b) Geometric mean profile and spatial cross section of stratification. For the mean profiles, grey shading indicates the range of the central 90% of data; alternating coloured background shading indicates the approximate depth ranges of the hydrographic layers defined in the text (PW, WH, and AW are labelled). For the spatial sections, the horizontal axis is broken and consecutively labelled 1–4 at the waypoints marked in Figure 3.1, indicating where the glider changed direction. White rectangle in (a) indicates the mesoscale eddy discussed in the text.

Layer	S_A [g kg^{-1}]	Depth [m]	T [°C]	σ [kg m^{-3}]	N^2 [10^{-4} s^{-2}]
SML	<28.3	[0 14]	[5.9 7.3]	[21.2 22.1]	—
CH	28.3 – 32.0	[12 47]	[−1.2 6.6]	[22.3 25.8]	[0.81 49.9]
PW	32.0 – 33.2	[47 122]	[−1.4 −0.6]	[25.9 27.1]	[0.41 2.45]
WH	33.2 – 34.8	[126 275]	[−1.36 0.07]	[27.3 29.1]	[0.18 1.46]
AW	>34.8	[267 —]	[0.15 0.36]	[29.1 29.8]	[0.03 0.31]

Table 3.1 – Properties of the hydrographic layers. Layers are defined by their absolute salinity, S_A. Ranges given for depth, conservative temperature, T, density anomaly, σ, and stratification, N^2, are for the central 90% of data. The layer labels are SML: Surface Mixed Layer; CH: Cold Halocline; PW: Pacific Water Layer; WH: Warm Halocline; AW: Atlantic Water Layer.

layer is $\Delta z \approx 160$ m thick and has a mean temperature $\overline{T}_{AW} = 0.30$ °C, the sequestered heat, E, is approximately

$$E = \rho c_p \left(\overline{T}_{AW} - T_o\right) \Delta z \approx 2 \times 10^8 \text{ J m}^{-2}, \tag{3.2}$$

relative to the melting temperature of ice, $T_o = 0$ °C. The factors ρ and c_p are the density and specific heat capacity of seawater, respectively. If mixed or advected to the surface, this heat could melt $Z^* = 0.66$ m of sea ice, where $Z^* = E/\rho_i l_o$, $\rho_i = 910$ kg m^{-3} is the density of sea ice, and $l_o = 3.3 \times 10^5$ J kg^{-1} is the latent heat of melting sea ice. This amount of sea ice loss would be a significant fraction of the Amundsen Gulf's mobile winter ice pack, which is typically 0.6–1.9 m thick in late spring (Peterson et al., 2008).

Second, the stratification is strong everywhere in the subsurface relative to that in lower-latitude oceans. Typical values for N^2 in the North Atlantic and North Pacific pycnoclines are O(10^{-6}) s^{-2} (Emery et al., 1984). This benchmark is comparable to the smallest N^2 values we observe in the AW, but is nearly two orders of magnitude smaller than N^2 in the PW layer and is three orders of magnitude smaller than N^2 in the CH. A study by Chanona et al. (2018) recently suggested that stratification is a key controlling feature of the mixing characteristics in many regions of the Beaufort Sea; we will build on these results in Section 3.4 by combining our stratification observations and direct turbulence measurements to demonstrate that density stratification frequently inhibits turbulent mixing in Amundsen Gulf. Note, the stratification we observe in Amundsen Gulf is comparable to that found throughout the Canada Basin, except in the core of the Cold Halocline, where we observe marginally stronger stratification (c.f. Chanona et al., 2018).

Finally, while most of the subsurface appears to be generally uniform in the horizontal, there is substantial horizontal mesoscale and smaller (O(1) km) temperature variability in the PW layer (Figure 3.2a). Most distinctive is the presence of a mesoscale eddy between waypoints 2 and 3. These features, and what they imply for mixing, are discussed further in Section 3.5.3.

3.4 Turbulence and Mixing

3.4.1 Turbulent Dissipation Rates

As is typical for ocean turbulence observations (Gregg, 1987; Lueck et al., 2002), we find an ε distribution (Figure 3.3a) that spans many orders of magnitude with a relatively small number of strongly turbulent events occurring in a less turbulent background flow

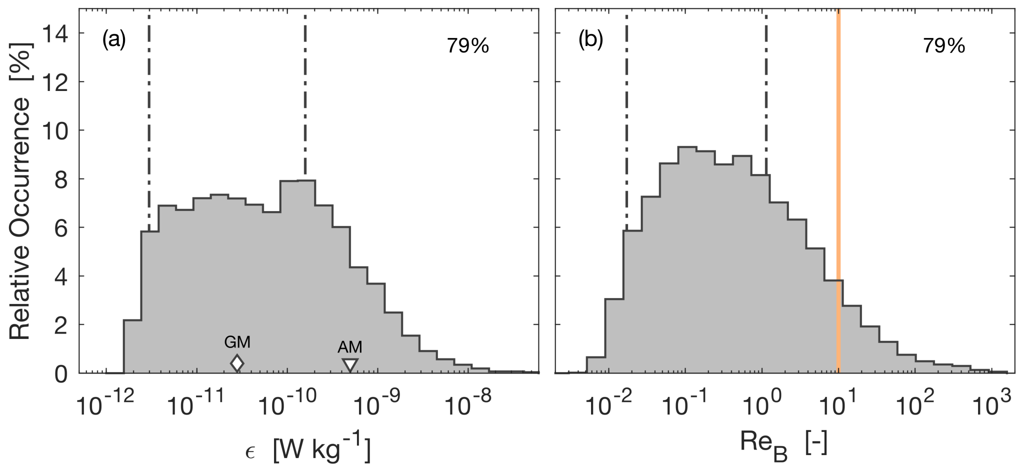

Figure 3.3 – Histograms of (a) the turbulent dissipation rate, ε, and (b) the buoyancy Reynolds number, Re_B. For each, the number in the top right indicates the percentage of data that fall within the axis limits; the remaining data are zero-valued and cannot be displayed on a logarithmic axis. The interquartile range for each set, including zero-valued data, is the span between the two dash-dotted lines. For ε, the geometric and arithmetic mean values are also indicated (GM and AM, respectively). For Re_B, the approximate critical value $Re_B^* = 10$ is indicated by the yellow line.

field. Note that zero-valued ε estimates (21% of the data; Section 3.2.2), representing turbulence too weak for us to observe, are not depicted in Figure 3.3a. Nonzero ε realizations vary over five orders of magnitude, from O(10^{-12}) to O(10^{-8}) W kg^{-1}; however, in 68% of the observations, ε is smaller than 1×10^{-10} W kg^{-1}, a common benchmark for "low turbulence" open ocean dissipation rates (Gregg, 1999; Lueck et al., 2002).

The arithmetic mean dissipation rate in our observations is 4.9×10^{-10} W kg^{-1}, and the geometric mean is 2.8×10^{-11} W kg^{-1}. Note that the geometric mean is defined only for non-zero values, so we set zero-valued estimates to the smallest nonzero value (2.0×10^{-12} W kg^{-1}) for this calculation only. The interquartile range, IQR, of our ε estimates is (3.0 – 160) $\times 10^{-12}$ W kg^{-1}, and the median value is 2.3×10^{-11} W kg^{-1}; only 0.4% of the distribution lies above 1×10^{-8} W kg^{-1}. For comparison, average mid-latitude dissipation rates at depths shallower than 1000 m are commonly O(10^{-10}) or O(10^{-9}) W kg^{-1} (Waterhouse et al., 2014), about one order of magnitude larger than we observe.

The variability of the ε field has a notable spatial structure that can be identified in the mean vertical profile and horizontal cross section of the field (Figure 3.4a). In the vertical, there is an ε minimum in the core of the cold PW layer at $\sim$100 m depth, with larger average dissipation rates near the sea surface and the seafloor. The geometric average of ε is 5×10^{-10} W kg^{-1} at 20 m depth, 1×10^{-11} W kg^{-1} at 110 m depth, and 2×10^{-10} W kg^{-1} at 350 m depth. Laterally, the most obvious source of variability is a prominent near-bottom patch of elevated dissipation at the base of the continental slope, with ε as high as O(10^{-8}) W kg^{-1}. This turbulent patch is found between s = 52–81 km and is identified in Figure 3.4a by a white rectangle.

Dissipation rates in the turbulent patch are anomalously high relative to the rest of the field, but modify the statistics of the full data set only marginally (Table 3.2). For example, the arithmetic mean of ε excluding estimates from within the patch is 4.4×10^{-10} W kg^{-1}, only 10% smaller than the estimate from the whole data set. However, the arithmetic mean of data only from within the patch is 11×10^{-10} W kg^{-1}, an increase by a factor of 2.2 over the mean calculated from the full set of data. For a similar comparison of the geometric mean, mode, median, and IQR see Table 3.2.

Further information about the variability in the ε field is available from the glider's three repeat transects over the continental shelf slope. A comparison of the depth-averaged dissipation rate estimates along the three transects is shown in Figure 3.5, for each of which ε is plotted as a function of distance from the glider's eastern-most waypoint, geometrically averaged in 2.5-km bins. This bin-averaged dissipation rate remained of the same order of magnitude over the 7 days needed to complete the transects—notice that the ε axis in Figure 3.5 is linear, not logarithmic—and varied between (1–5)$\times 10^{-11}$ W kg^{-1}. From the first and last transects, it appears that ε is systematically larger in the central Gulf than it is on the shelf slope, but the second transect doesn't exhibit this pattern; nonetheless, when all transects are averaged together (not shown), the pattern of enhanced ε towards the central Gulf remains. The patch of enhanced ε obvious in Figure 3.4 is situated to the immediate left of the leftmost axis limit in Figure 3.5.

A notable attribute of the ε transects in Figure 3.5 is that the patterns of local maxima and minima appear quasi-stationary across all three transects. The most obvious feature correlating the patterns in the three transects is the peak at 23.8 km, though 7 other peaks or troughs can be traced between transects, indicated in Figure 3.5 by the dash-dotted lines. The stationarity of these features indicates that they may be the result of interactions between local topography and the flow field—either tides, internal waves, or the local background flow—but we would need higher resolution topography measurements and more information about the immediate flow to verify this hypothesis. Note that it is impossible to truly decouple time and space variability in measurements taken by a glider; here, we have treated the ε observations primarily as a spatial series in order to highlight what appear to be primarily geographic features, but we will discuss temporal variability and its implications in Section 3.5.1.

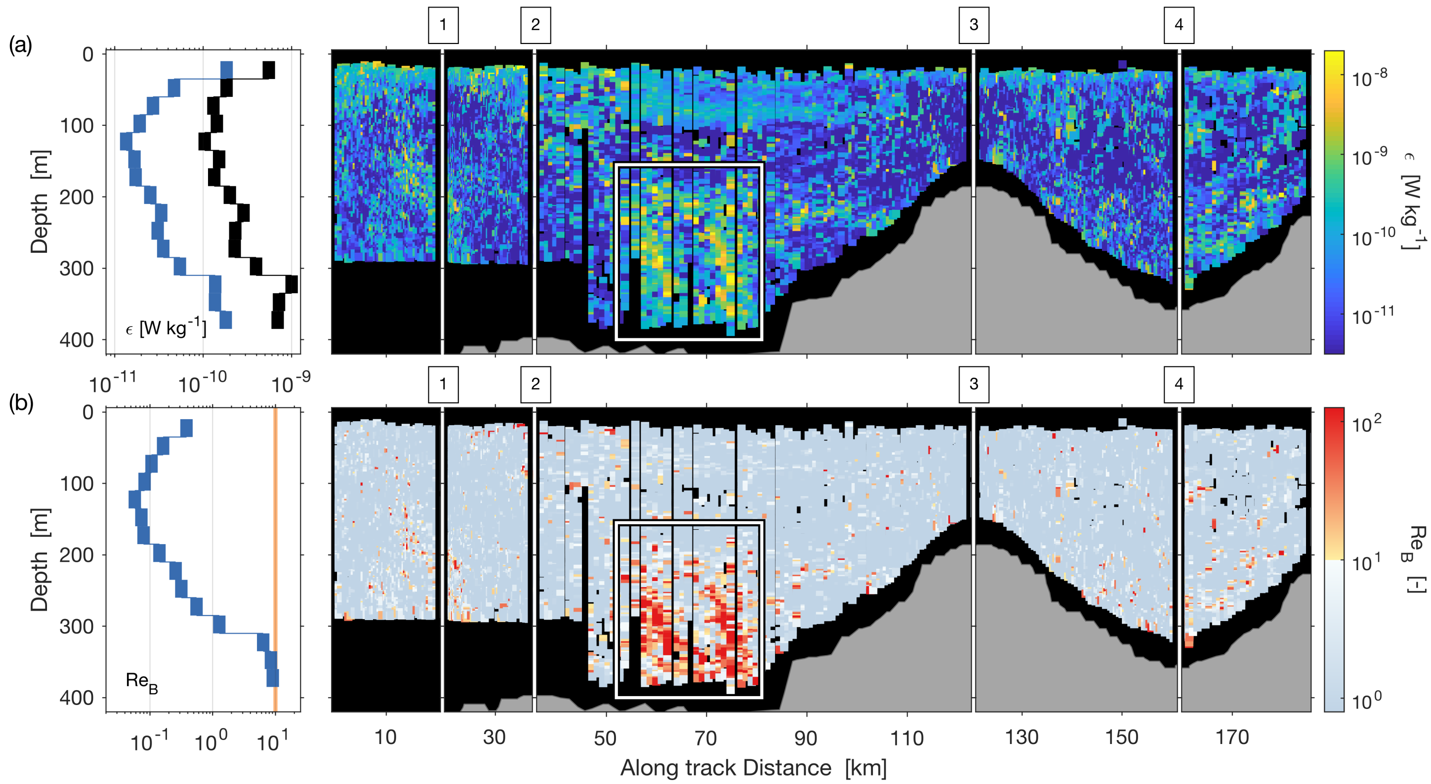

Figure 3.4 – Mean vertical profiles and horizontal cross sections of (a) ε, and (b) Re_B. Waypoints are indicated as in Figure 3.2. For each, the geometric mean profile is given in 25 m bins (blue); for ε, the arithmetic mean profile is also given (black). In both cross sections, the white rectangle between waypoints 2 and 3 identifies the patch of enhanced turbulence discussed in the text. In the Re_B cross section, red pixels indicate where a turbulent diapycnal flux is expected; grey pixels indicate a predicted absence of turbulent diapycnal mixing. The approximate critical value $Re_B^* = 10$ is indicated in the Re_B mean profile by the vertical yellow line.

	Arithmetic Mean	Geometric Mean	Median	IQR
All Data				
ε [10^{-11} W kg^{-1}]	49	2.8	2.3	0.3 – 16
K_ρ [10^{-8} m^2 s^{-1}]	450	–	−0.31	−1.1 – 0.18
Excluding Turbulent Patch				
ε [10^{-11} W kg^{-1}]	44	2.4	1.9	0.3 – 13
K_ρ [10^{-8} m^2 s^{-1}]	100	–	−0.29	−1.0 – 0.16
Turbulent Patch Only				
ε [10^{-11} W kg^{-1}]	110	15	18	2.7 – 79
K_ρ [10^{-8} m^2 s^{-1}]	4,600	–	−0.65	−1.5 – 810

Table 3.2 – Select statistics of ε and K_ρ observed in (top) all the data; (middle) all data except that within the turbulent patch; and (bottom) data only from within the turbulent patch. The turbulent patch is defined as the region inside the white rectangle in Figures 3.4 and 3.7, between s = 52–81 km on the horizontal axis.

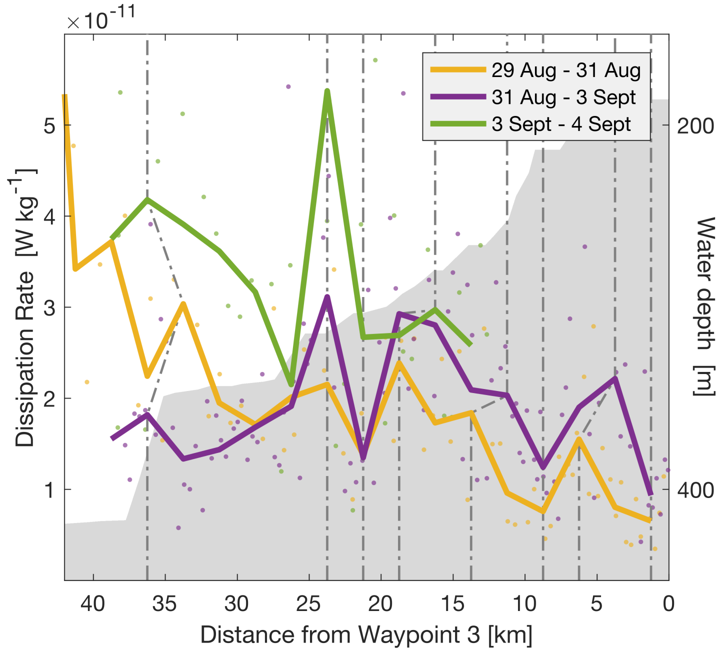

Figure 3.5 – The three repeat ε transects (left vertical axis) over the continental shelf slope. The horizontal axis is the distance from Waypoint 3 shown in Figure 3.1b. Thick lines are 2.5 km geometric mean bin-averages of ε; coloured markers in the background are individual geometric mean cast-averages. The quasi-vertical dash-dotted lines connect peaks and troughs that appear to be stationary between the three ε transects, as discussed in the text. The bathymetry is shown with grey shading in the background (right vertical axis) for reference.

3.4.2 The Influence of Stratification

Combining observations of ε with those of N^2 and the kinematic viscosity, ν, we construct estimates of the buoyancy Reynolds number, $Re_B = \varepsilon/\nu N^2$, which quantify the energetic capacity of the flow to develop vertical overturns that lead to diapycnal mixing (Figures 3.3b, 3.4b). The Re_B parameter is a measure of the relative magnitudes of turbulent kinetic energy, which tends to create mixing through vertical density overturns, and potential energy stored in the stratification, which inhibits vertical overturning. Evidence from laboratory, numerical, and field studies suggests that the Re_B parameter has a critical value near $Re_B^* = 10$ below which vertical overturns and diapycnal turbulent mixing are unlikely (Stillinger et al., 1983; Shih et al., 2005; Ivey et al., 2008; Bouffard and Boegman, 2013).

Imposing this Re_B^* criterion separates our data into two regimes, one where turbulent diapycnal mixing is expected ($Re_B \geq 10$), and one where it is not ($Re_B < 10$). Doing so, we find that turbulence in the flow is energetic enough to support enhanced diapycnal mixing in only 7% of the observations—these are the measurements to the right of the yellow vertical line in Figure 3.3b. Equivalently, we can say that we do not expect enhanced turbulent mixing in 93% of observations, suggesting that vertical fluxes of properties like temperature and density are set by molecular diffusion in this large subset of the data. The Re_B distribution, therefore, suggests that stratification plays a dominant role in modulating turbulent mixing in Amundsen Gulf, frequently inhibiting the development of turbulence.

Further, it is clear from the mean vertical profile and spatial cross section of the Re_B field (Figure 3.4b) that turbulent mixing is not homogeneously distributed in space. Rather, most of the mixing happens within 100 m of the seafloor in the isolated patch of enhanced ε that we observed at the edge of the shelf slope region (i.e. inside the white rectangles in Figure 3.4). Only here is Re_B commonly of O(10) or larger, with individual values occasionally reaching as large as O(10^3). The white rectangle representing the region of enhanced ε in Figure 3.4a encloses only 8% of the observations, but it encloses 41% of the occurrences where $Re_B \geq 10$ and 64% of those where $Re_B \geq 100$. Inside the rectangle, 37% of the observations indicate that $Re_B \geq 10$; in contrast, for all the data outside the rectangle, only 5% of the observations indicate that $Re_B \geq 10$.

3.4.3 Diffusivity Estimates

In the 7% of observations where $Re_B \geq 10$ (Section 3.4.2), we expect that turbulence drives a localized enhanced density flux. For these observations we calculate the rate of diapycnal density diffusion, K_ρ, using the canonical Osborn (1980) model for turbulent mixing:

$$K_\rho = \Gamma \frac{\varepsilon}{N^2}\,, \tag{3.3}$$

where Γ is a flux coefficient that we take to be 0.2, following Osborn's original (upper bound) estimate.

In the remaining 93% of observations, where $Re_B < 10$ and a turbulent density flux is unlikely, temperature and salinity are expected to diffuse by molecular diffusion. Assuming a linear approximation for the equation of state of seawater, the diffusivity of density in this case is given by

$$K_\rho = \frac{R_\rho\,\kappa_S^{\mathrm{mol}} - \kappa_T^{\mathrm{mol}}}{R_\rho - 1}\,, \tag{3.4}$$

where $\kappa_T^{\mathrm{mol}} = 1.4 \times 10^{-7}$ m^2 s^{-1} and $\kappa_S^{\mathrm{mol}} = 1.0 \times 10^{-9}$ m^2 s^{-1} are the molecular diffusion rates of temperature and salinity in seawater[1]. Since $\kappa_T^{\mathrm{mol}} = 140\kappa_S^{\mathrm{mol}}$, this expres-

[1]Equation 3.4 can be verified by substituting the K_ρ expression into a Fickian density flux formulation, $F_\rho = K_\rho \partial\rho/\partial z$, which returns the expected expression $F_\rho = \rho_0(\kappa_S \beta \partial S_A/\partial z - \kappa_T \alpha \partial T/\partial z)$, where F_ρ is the vertical density flux.

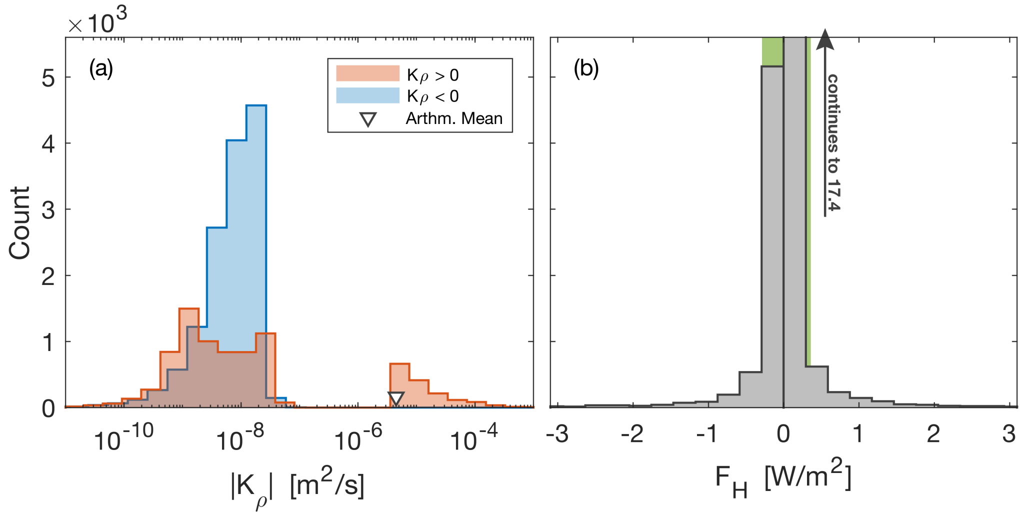

Figure 3.6 – Histograms of (a) the diapycnal mixing coefficient, K_ρ, of density and (b) the vertical heat flux, F_H. Positive K_ρ indicate down-gradient density diffusion; negative K_ρ indicate up-gradient density diffusion. For F_H, the green shaded area indicates the region between the 5th and 95th percentiles.

sion can be simplified to

$$K_\rho = \frac{(R_\rho - 140)}{R_\rho - 1}\,\kappa_S^{\text{mol}}. \tag{3.5}$$

The quantity R_ρ is the gradient density ratio, defined as

$$R_\rho \equiv \frac{\beta\,(\partial S_{\text{A}}/\partial z)}{\alpha\,(\partial T/\partial z)}\,, \tag{3.6}$$

where α and β are the coefficients for thermal expansion and haline contraction of seawater. Note that K_ρ here may be either positive or negative, depending on the sign and magnitude of R_ρ. Specifically, when $1 < R_\rho < 140$ (which it is in 67% of our observations where $Re_B < 10$), the density flux due to molecular diffusion of temperature and salinity is downward, in the direction of increasing density. Finally, note also that the water column becomes susceptible to double diffusion when $1 < R_\rho < 10$, a phenomenon that we have neglected here; we address possible effects resulting from double diffusion in Section 3.5.2.

A histogram of the diffusivity estimates, separated by up-gradient and down-gradient, is given in Figure 3.6a. The discontinuity between 8×10^{-8} and 3×10^{-6} m^2 s^{-1} reflects the distinction between turbulent and molecular diffusion, with all data to the right of the discontinuity expected to be turbulent and all data to the left expected to be molecular. The discontinuity is an artifact of the Osborn model's inability to describe the transition between turbulent and non-turbulent density fluxes (see Chapter 4). However, though striking in the histogram, the discontinuity in the histogram of our K_ρ estimates does not alter the broader interpretation of the mixing rates because bulk buoyancy transfor-

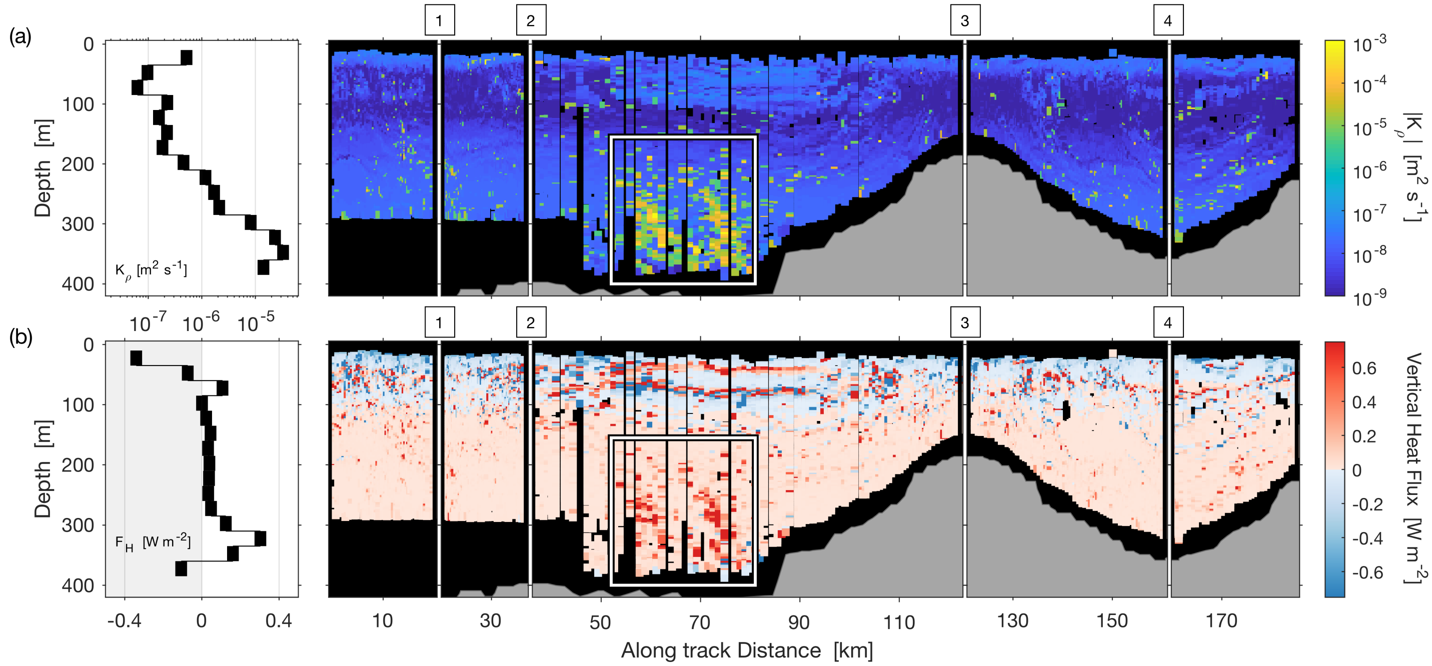

Figure 3.7 – Arithmetic mean vertical profiles, in 25-m bins, and horizontal cross sections of (a) the diapycnal mixing coefficient, K_ρ, of density and (b) the vertical heat flux, F_H. For the cross sections, the horizontal axis, waypoint markers, and white rectangle identifying the turbulent patch are as in Figure 3.4. The K_ρ cross section depicts the absolute value.

mations are disproportionately driven by the few turbulent, strongly energetic mixing events described in Section 3.4.2. Arithmetic K_ρ averages are largely unaffected by variability (or inaccuracies) in the smaller-orders of magnitude K_ρ estimates. Note that, for the same reason, negative K_ρ values are largely immaterial to the arithmetic mean diffusivities shown in Figures 3.6a and 3.7a; though somewhat unusual, the negative K_ρ estimates are small in magnitude relative to the few large (and positive) K_ρ estimates seen on the right-hand-side of Figure 3.6a which primarily determine the mean diffusivity.

The arithmetic mean of all K_ρ estimates is 4.5×10^{-6} m^2 s^{-1}, about 32 times larger than the molecular diffusivity of temperature and about 4500 times larger than the molecular diffusivity of salinity, highlighting the importance of the relatively small number of energetic mixing estimates in setting the mean mixing rate. The arithmetic mean is the 94th percentile of data. Note that if we used the Osborn model (Equation 3.3) without imposing an Re_B^* criterion to separate turbulent and non-turbulent estimates, the arithmetic mean of all K_ρ estimates would be 4.8×10^{-6} m^2 s^{-1}, a factor of only 1.1 times larger than the K_ρ average we present.

The disproportionate contribution of a few scattered but strongly turbulent mixing estimates is obvious when comparing the arithmetic mean profile of K_ρ with its horizontal cross section (Figure 3.7a), especially above 200 m depth. In this part of the water column, a very small number of turbulent mixing estimates—represented by scattered green and yellow pixels in the section—are superimposed without any recognizable pattern overtop of an otherwise non-turbulent background—represented by the dark blue. In the upper 200 m of the water column, only 3% of the observations indicate a turbulent density flux. However, the arithmetic mean profile is typically O(10^{-7}) m^2 s^{-1}, two orders of magnitude above the background molecular salinity diffusivity.

Below 200 m, the arithmetic average of K_ρ increases steadily and reaches a maximum of 3.3×10^{-5} m^2 s^{-1} between 335–360 m depth. This elevated mean-K_ρ signal is mostly dominated by the same energetic patch that we observed in the ε and Re_B sections (Figure 3.4). Inside this patch, where 37% of the observations indicate a turbulent signal (Section 3.4.2), the arithmetic mean K_ρ value is 4.6×10^{-5} m^2 s^{-1}; in comparison, outside the patch, where only 5% of the observations have a turbulent diffusivity signal, the arithmetic mean is 1.0×10^{-6} m^2 s^{-1}. Further metrics comparing K_ρ inside and outside the patch are presented in Table 3.2.

3.4.4 Vertical Heat Fluxes

We leverage the high resolution of the temperature microstructure measurements to estimate the diffusivity of temperature using the Osborn-Cox relation (Osborn and Cox, 1972):

$$K_T = \kappa_T^{\mathrm{mol}}(C+1) \quad , \tag{3.7}$$

where $\kappa_T^{\mathrm{mol}} = 1.4 \times 10^{-7}$ m^2 s^{-1} is the molecular diffusivity of temperature and C is the Cox number, defined

$$C \equiv \frac{3\left\langle (\partial T'/\partial x)^2 \right\rangle}{(\Delta T/\Delta z)^2} \quad , \tag{3.8}$$

which we calculate from the mean vertical background temperature gradient, $\Delta T/\Delta z$, and the microscale temperature gradient, $\partial T'/\partial x$, whose ensemble-average is assumed isotropic. Angle brackets indicate ensemble averaging over the same segments and subsegments used for the ε calculations (Section 3.2.2). The Cox number is a measure of the amount that turbulence has deformed a smooth background temperature structure and is proportional to the turbulent temperature diffusivity (Winters and D'Asaro, 1996). Note that K_T and K_ρ are not generally equivalent in our observations because temperature acts largely as a passive tracer.

From the K_T estimates, the vertical heat flux, F_H, is straightforward to obtain using the form for Fickian diffusion:

$$F_H = -\rho c_p K_T \frac{\Delta T}{\Delta z} \quad . \tag{3.9}$$

The factor $c_p = 4.1 \times 10^3$ J kg^{-1} K^{-1} is the specific heat capacity of seawater.

The heat flux estimates we obtain are almost exclusively small (Figure 3.6b): the absolute value of the flux, $|F_H|$, is less than 1 W m^{-2} in 96% of the observations, and the IQR of $|F_H|$ is 0.01–0.08 W m^{-2}. We find $|F_H| \geq 10$ W m^{-2} in only 0.6% of observations, and $|F_H| \geq 100$ W m^{-2} in only 0.02% of observations. The arithmetic mean heat flux through the warm halocline, separating the warm core of the AW and cold core of the PW, is only 0.03 W m^{-2}. This is small compared to the Arctic Ocean-wide mean heat loss of 6.7 W m^{-2} out of the AW (Turner, 2010).

There is, of course, substantial horizontal and vertical variability (Figure 3.7b), and the arithmetic mean upward heat flux reaches as high as 0.30 W m^{-2} in the AW layer because of the effects of the locally isolated high-energy patch (Section 3.4.1). However, even inside the patch, heat fluxes are modest: the arithmetic mean value of F_H here is 0.22 W m^{-2}, and F_H exceeds 10 W m^{-2} in only 0.30% of observations; it never exceeds 100 W m^{-2}. The generally-downward heat flux between the surface mixed layer and the cold core of the PW layer is likewise spatially variable, as seen in the spatial section in Figure 3.7b, with interspersed upward and downward fluxes. The arithmetic mean downward flux is -0.34 W m^{-2} at depths 10–35 m. There are more substantial heat fluxes out of the top and bottom of the warm core eddy which can be as large as O(100) W m^{-2} in a few isolated observations.

The heat fluxes we report here are generally comparable to, or smaller than, those seen in previously published observations for the region. In the central Canada Basin, where double diffusion often dominates the mixing, fluxes are typically observed to be O(0.1) W m^{-2} (e.g. Timmermans et al., 2008a; Shibley et al., 2017), and on the Beaufort shelf along the North American continent, heat fluxes are typically O(0.1) or O(1) W m^{-2} (Shaw et al., 2009; Chanona et al., 2018).

3.5 Discussion: Mixing Processes

3.5.1 Tidal Mixing

In addition to geographic variability (Section 3.4.1), the ε field has a systematic temporal signal that appears to be driven by the M2 tide. A combination of four factors points to the dominant role of the M2 tide in modulating the temporal turbulence variability: (*i*) a peak in the ε power spectrum at the M2 tidal frequency; (*ii*) a substantial tidal signal in the local currents; (*iii*) a high likelihood of local internal tide generation; and (*iv*) the known propensity for localized internal tide dissipation. We briefly outline each of these here.

In Figure 3.8a, we have constructed a power density spectrum of the ε observations, neglecting spatial variability and treating the glider measurements as a simple time series. The time series, shown in Figure 3.8b, is of geometrically depth-averaged ε observations deeper than 100 m, interpolated to a 15-minute grid and filtered to remove temporal variability on scales smaller than 2 hours. The spectrum is constructed with Welch's method using 4-day segments of data, 50% overlapped and Hamming-windowed. The most notable feature in the ε power spectrum is a rounded peak between frequencies 1.3–2.4 cpd, straddling both the M2 tidal frequency, 1.93 cpd, and the local inertial frequency, f = 1.90 cpd. The spectral peak indicates that the dominant mode of temporal variability in ε is linked to the M2 tide, inertial forcing, or some combination of both.

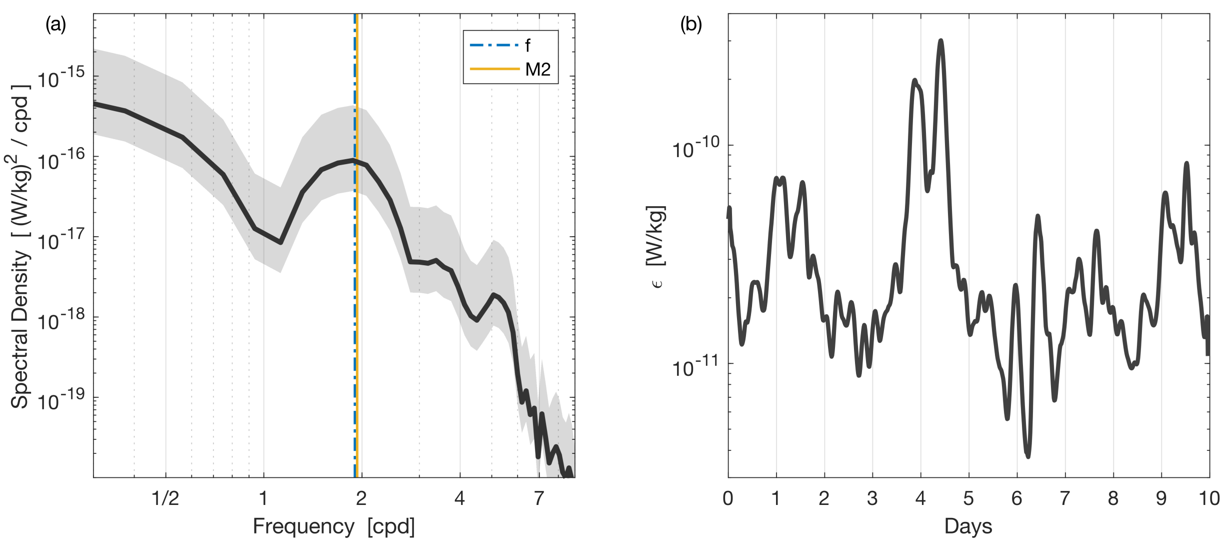

Figure 3.8 – (a) Power density spectrum of ε, constructed using Welch's method and 4 day segments of data. Grey shading indicates the 95% confidence interval. The M2 and inertial frequencies are indicated. (b) The ε time series used to construct the power density spectrum. The series is made from the geometric cast-averages of ε for all depths greater than 100 m and is interpolated to a 15 minute grid. Variability on scales smaller than 2 hours has been removed.

Two lines of reasoning suggest that the tides are more important than the winds in setting the ε variability seen in Figure 3.8. First, there is no analogous peak in the ε power spectrum for observations shallower than 100 m (not shown); the signal at the inertial and M2 frequencies is only prevalent in the deeper measurements, suggesting it is unlikely that the forcing originates at the surface (cf. Lincoln et al., 2016). Second, Acoustic Doppler Current Profiler measurements from a nearby mooring (ArcticNet, 2018, mooring CA08, Figure 3.1b) indicate that local current variability is strongly tidal. Power density spectra of eastward and northward current velocities, U and V, exhibit narrow peaks centred on the M2 frequency (Figure 3.9b), and the slow and steady modulation of the barotropic velocity amplitude (Figure 3.9a) in the dominant eastward component suggests that the current variability is indeed predominantly tidal, not wind-

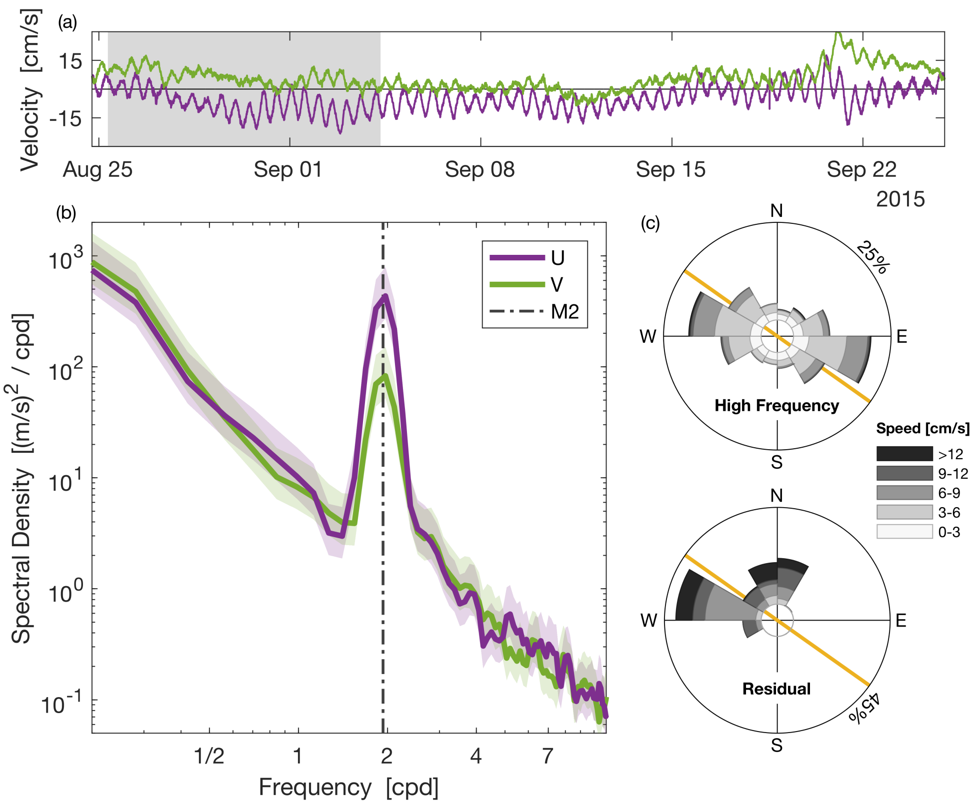

Figure 3.9 – (a) Depth-averaged current velocity components U and V, measured by ArcticNet mooring CA08 between depths 100–170 m. The grey shading indicates the period of the glider deployment. (b) Power density spectra of the above U and V records, with 95% confidence intervals. (c) Polar histograms with current speeds of the above U and V records, decomposed into high frequency and residual components. High frequencies are defined as those greater than 1.3 cpd and are dominated by the M2 tide. The approximate orientation of the Amundsen Gulf's major axis, azimuth 305°, is indicated in each histogram by the yellow line. The percentage on each histogram's perimeter is the tick label for the radial axis (Relative Occurrence).

driven.

The directionality of the barotropic tide further suggests that tidally forced mixing is an important process. Decomposing the currents into high frequency and residual flows using a scale separation of 1.3 cpd, we find that the high frequency flow (dominated by the tides, and accounting for 23% of the total variance) is predominantly aligned with the major axis of the Amundsen Gulf (Figure 3.9c). This alignment is significant because our measurements were taken near (∼40 km from) the Amundsen Gulf's sill and the adjacent complex topography offshore of the southern tip of Banks Island (Figure 3.1a). The directionality of the high frequency currents indicates that the barotropic tide modulates flow over the sill and adjacent topography at the dominant tidal frequency, making this a likely region for internal tide generation (Polzin et al., 1997; MacKinnon et al., 2017). Note that the current speed is strong only once per tidal cycle, not twice per tidal cycle as would be expected in a tidally dominated region, because the residual flow is stronger than the tidal flow (Figure 3.9c), preventing the net current vector from changing direction on each tidal cycle. Note also that the shelf slope north of nearby Cape Bathurst has previously been identified as a likely region of strong internal tide generation (Kulikov et al., 2004) and that observations linking tides and topography to mixing have been recently reported for the broader Arctic Ocean (Rippeth et al., 2015, 2017).

Finally, an important feature that distinguishes the internal tide here from those in lower latitudes is that an M2 internal tide generated in the Beaufort Sea is not expected to be able to propagate away to the interior of the Canada Basin. Linear wave theory does not allow free propagation of the M2 internal tide northward of 74.47°, and it has been previously suggested that an M2 internal tide generated in this region becomes resonantly trapped between the continent and the critical latitude (Kulikov et al., 2004). Ultimately, internal tides generated in the Beaufort Sea are expected to dissipate near their generation site (Morozov and Pisarev, 2002; Kulikov et al., 2010), supporting the idea that the temporal mixing variability we see in Amundsen Gulf is tidally modulated by a locally generated internal tide. See Kulikov et al. (2004) for an analysis of local baroclinic tide generation potential.

3.5.2 Double Diffusion

Even when energetics do not support a turbulent density flux (Section 3.4.2), enhanced vertical mixing can still result from double diffusive convection given the right temperature and salinity conditions (Radko, 2013). The susceptibility of a water column to double diffusion can be characterized by R_ρ, the gradient density ratio (Equation 3.6). Empirically, double diffusion is most commonly observed when $1 < R_\rho \leq 7$; it is also sometimes seen when $7 < R_\rho \leq 10$, but it is not typically observed when $R_\rho > 10$ (Kelley et al., 2003). In the central Canada Basin's warm halocline, R_ρ is typically 6.3 ± 1.4, and coherent double diffusive staircases are observed over horizontal scales exceeding 1000 km (Timmermans et al., 2008a; Shibley et al., 2017).

We calculate R_ρ from our measurements (Figure 3.10) using background gradients filtered to exclude vertical scales smaller than 5 m and find that $1 \leq R_\rho < 10$ in 21% of observations; 19% are in the range 7–10, and 2% are in the range 1–7. Instances where $R_\rho < 10$ are almost exclusively in a band near the top of the Atlantic Water layer: in the potential density band $\sigma = 28.5$–29.5 kg m^{-3}, corresponding approximately to the depth range ~200–335 m, 70% of R_ρ observations are in the range 1–10. There is also a notable number of small R_ρ values in the eddy, where 16% of R_ρ observations are in the range 1–10.

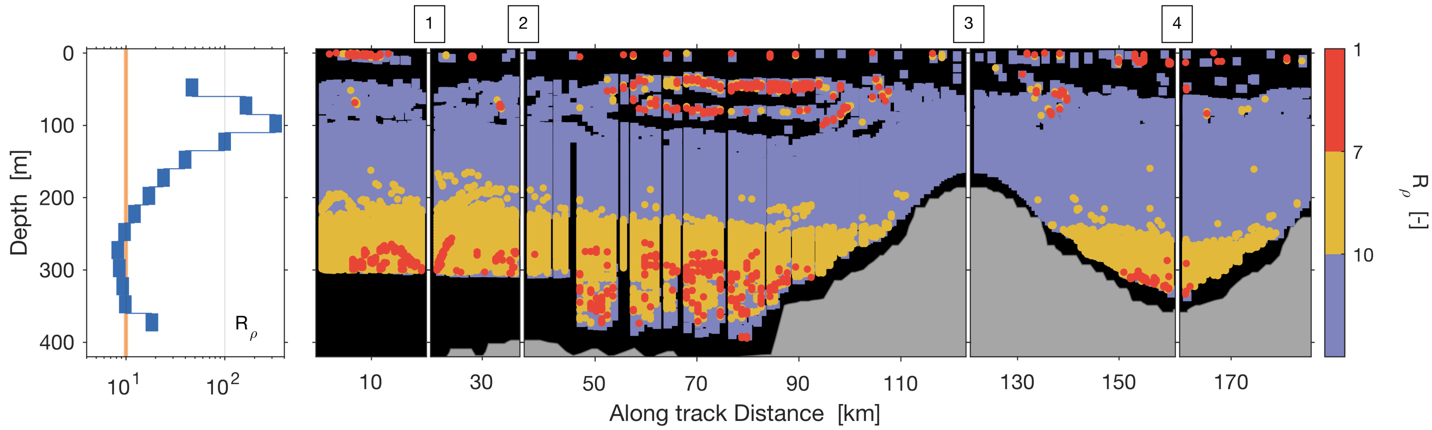

Figure 3.10 – Geometric mean vertical profile and horizontal cross section of the density ratio, R_ρ. In the cross section, data are discretized into three regimes: susceptible to double diffusion (red: $R_\rho \leq 7$), marginally susceptible (yellow: $7 < R_\rho \leq 10$), and not susceptible (purple: $R_\rho > 10$). The approximate critical value $R_\rho = 10$ is shown in the mean profile by the yellow vertical line.

Despite conditions near the top of the AW layer that suggest the density structure there is favourable to double diffusion, we do not find double diffusive staircases like those observed in the central Canada Basin's thermocline. There are sporadicly dispersed individual temperature steps that are likely related to double diffusive processes, but there are no pervasive double diffusive features in our observations. It appears, therefore, that double diffusion does not play a substantial role in the broader vertical transport of heat or density out of the thermocline in this region. This finding is somewhat surprising because it is often thought that the absence of a double diffusive staircase implies energetic turbulent mixing (e.g. Guthrie et al., 2017; Shibley and Timmermans, 2019); it remains unclear then why there is no double diffusive staircase in our observations, given that turbulent mixing estimates from our data set are typically weak.

3.5.3 Pacific Water Mesoscale and Smaller Features

One of the most striking features in our observations is the large variability in the temperature structure of the Pacific Water layer, visible in an enlarged view of the temperature cross section (Figure 3.11a). The most obvious feature here is the anticyclonic warm-core mesoscale eddy between $s = 52$–98 km and depths 40–100 m. In its core, at $\sim$50 m depth, the maximum temperature is $-0.1°$C, about 1.3°C warmer than the ambient water. It appears to have at least one outer tendril, transected by the glider twice at $s = 104$ and $s = 139$ km. Note that the glider needed about 1.5 days to transect the eddy; we do not know how quickly the eddy was moving over ground, but if we assume it was being advected by up to 15 cm s^{-1}, it could have translated up to 19 kilometres while being transected by the glider, indicating that the eddy's diameter was 46 ± 19 km.

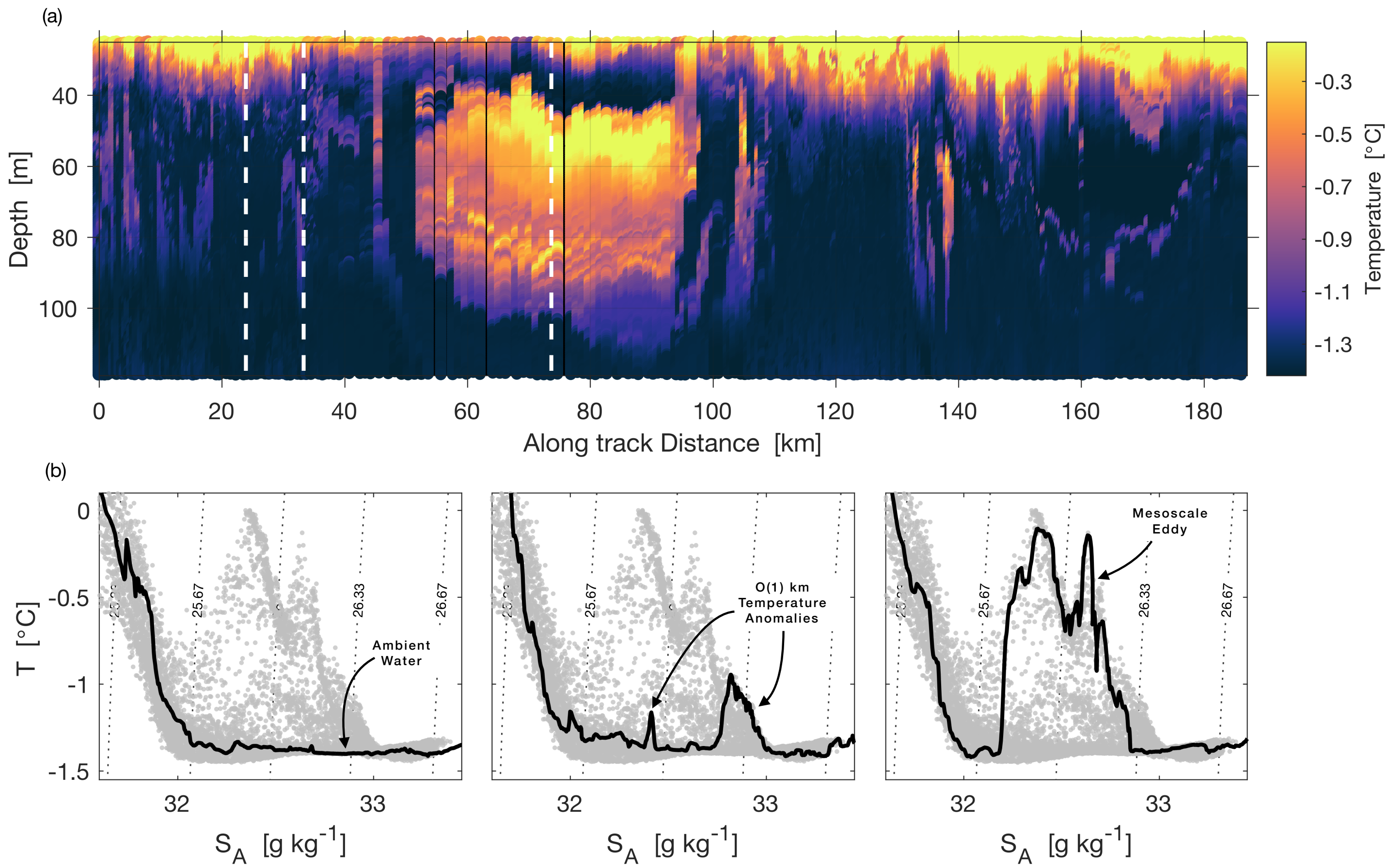

Figure 3.11 – (a) An enlarged view of the temperature cross section of the cold halocline and Pacific Water layers, highlighting the eddy as well as smaller, O(1) km, temperature anomalies. The dashed white lines correspond, from left to right, to the three T-S lines shown in the lower three panels. (b) T-S diagrams for the three vertical profiles indicated in the upper panel. Grey dots are all the data shown in the upper panel. Dotted lines are density contours.

The origin of the eddy is unknown, but its T-S characteristics (Figure 3.11b) suggest that it was not generated locally. Its large temperature anomaly suggests that its origin is in a locale where the Pacific Water layer outcrops to the surface, which occurs periodically at Cape Bathurst (Williams and Carmack, 2008; Sévigny et al., 2015) and at Mackenzie Canyon (Williams et al., 2006), and of course at the inflow of Pacific-origin water in the Chukchi Sea. Fine et al. (2018) estimated the lifespan of a mesoscale eddy on the Chukchi shelf to be 1–2 years, indicating that it is possible for any of these three locales to be a source region of the eddy we observe; assuming an eastward advection scale of $\sim$5 cm s^{-1} along the shelf-break boundary current (Williams and Carmack, 2015), an eddy generated in the Chukchi Sea would reach Amundsen Gulf in $\sim$250 days.

Irrespective of its origin, the eddy likely had a strong, and perhaps dominant, influence on the local heat budget of the PW layer. An idealized form of the eddy—a cylinder of radius 23 km, height 60 m, and mean temperature -0.65°C—would carry 310 PJ of heat relative to the ambient water. The arithmetic mean heat flux we observe out of the top of the eddy (in the band $\sigma = 25.7$–25.8 kg m^{-3}) is 1.6 W m^{-2}, and the arithmetic mean heat flux out of the bottom of the eddy (in the band $\sigma = 26.6$–26.7 kg m^{-3}) is -2.9 W m^{-2}, an order of magnitude larger than arithmetic mean fluxes estimated in the PW layer as a whole (Section 3.4.4). We do not have estimates of the lateral heat flux out of the flanks of the eddy, but Fine et al. (2018) found lateral fluxes due to intrusions 400–4000 times larger than vertical fluxes out of the eddy that they observed. If we use this result as a reference and speculate that the lateral flux out of our eddy is 900 W m^{-2} (i.e. 400 times as large as the mean flux out of the top and bottom), we can integrate the flux estimates over our idealized cylindrical eddy shape. Doing so, we find a total flux of 7.8 GW out of the sides of the eddy, and 7.5 GW out of the combined top and bottom boundaries of the eddy, resulting in an estimated total heat flux out of the eddy of 15.3 GW. It is important to note this calculation is highly speculative as there were important differences between the eddy we observed and that seen by Fine et al. (2018); nonetheless, using this calculation as a reference and if this flux remained constant, the heat in the eddy would dissipate within 238 days.

Equally striking as the eddy is the presence of substantial temperature variability on horizontal scales of O(1) km seen throughout the PW layer. This variability can be seen in Figure 3.11a as a series of light purple blotches superimposed on the ambient PW outside of the influence of the eddy. T-S characteristics of the smaller scale structures (Figure 3.11b) are distinct enough from those of the eddy that they are likely distinct features, not tendrils of the eddy. It is unclear how the smaller structures were created, but the presence of excess heat in the anomalies suggests a connection to the warmer near-surface waters. In light of recent results by Sévigny et al. (2015), who linked horizontal temperature structure above 100 m depth in Amundsen Gulf to submesoscale frontal formation and isopycnal outcropping at Cape Bathurst, it is possible that we are observing remnant features of nearby submesoscale dynamics. Given the otherwise weak heat fluxes and minimal turbulent mixing in the PW layer, these features are likely to play a meaningful role in the overall temperature budget of the layer.

3.6 Conclusions

Characterizing turbulent dissipation rates, diapycnal mixing rates, and vertical heat fluxes in Amundsen Gulf, we found that stratification is the dominant modulator of turbulent mixing in the region. Most commonly, the effects of turbulence were weak in relation to the gravitational stability from the density field, precluding the likelihood of turbulent diapycnal mixing; as a result, the mean diapycnal diffusivity for density was small compared to that typical of lower latitude oceans. However, turbulence appeared to be energetic enough to drive an enhanced buoyancy flux in a small number (7%) of the observations, and these had a disproportionate influence on the net mixing rate. These relatively few energetic events enhanced the arithmetic mean diffusivity of density by orders of magnitude over that which would result from pure molecular diffusion.

We found evidence that much of the overall variability in turbulence below the PW layer is driven by the M2 tide, adding to the recent understanding that tides appear to be a dominant forcing mechanism for turbulence and mixing in the Beaufort Sea (e.g. Rippeth et al., 2015). However, the resulting arithmetic mean heat flux from the warm AW layer is small and unlikely to be a leading order contributor to increased future sea ice melt (cf. Carmack et al., 2015). In the PW layer, the temperature variability was dominated by a warm mesoscale eddy which had the largest influence on the localized heat budget of this layer. This observation supports the notion that eddies are an important, and perhaps a leading order, contributor to the dynamics and heat budget of the near-surface Beaufort Sea (e.g. Zhao and Timmermans, 2015; Fine et al., 2018).

Chapter 4

Enhanced Heat Fluxes in a Marginally Turbulent Flow

4.1 Introduction

The aim of this study is to examine the characteristics of ocean mixing when turbulence is weak and stratification is strong. It was motivated when, in an attempt to characterize mixing rates and heat fluxes using a series of microstructure measurements in the southeastern Beaufort Sea (Chapter 3), we noticed that models for ocean mixing failed to accurately predict the turbulent-scale tracer variance we observed in our measurements. There continued to be notable micro-scale temperature gradients in conditions where numerical and laboratory studies previously found that turbulent mixing should be negligible. Finding few previous reports of field-based studies on the characteristics of turbulence in an analogous locale and mixing regime, and—in light of the increasing interest in Arctic Ocean mixing—recognizing the importance of correctly predicting enhanced tracer fluxes in weakly turbulent, strongly stratified environments, we determined to analyze these results in a dedicated study.

As outlined in a review by Ivey et al. (2008), enhanced diffusion of ocean tracers due to turbulent mixing must eventually revert to simple molecular diffusion as turbulence weakens. For shear-driven turbulence, which is often assumed to drive the majority of mixing in the ocean's interior, the buoyancy Reynolds number,

$$Re_B = \frac{\varepsilon}{\nu N^2}, \tag{4.1}$$

is used as a parameter to distinguish between molecular and turbulent diffusion regimes. Here, ε is the dissipation rate of turbulent kinetic energy, ν is the kinematic viscosity of

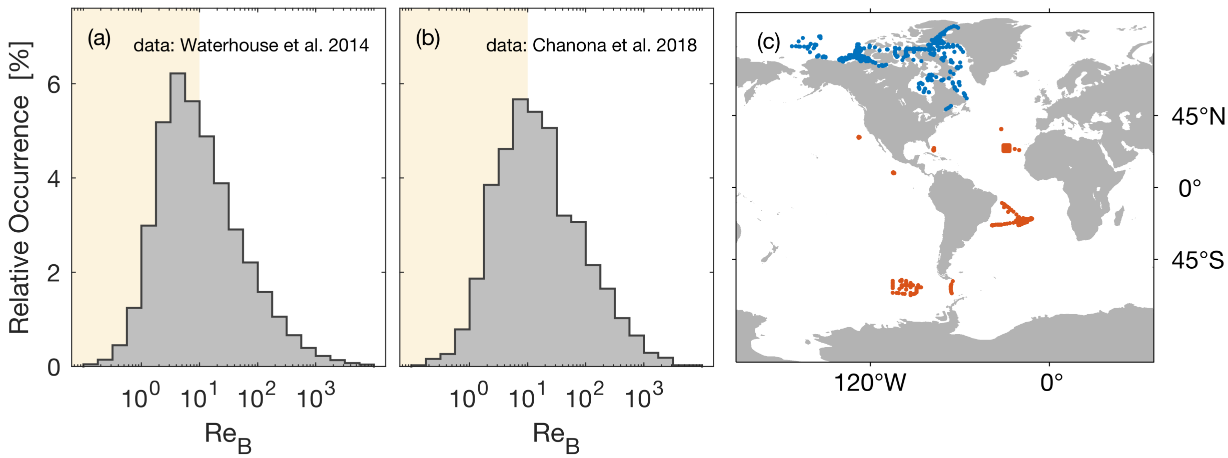

Figure 4.1 – (a) Distribution of Re_B from microstructure data collated in Waterhouse et al. (2014), between the surface mixed layer and 1000 m depth, for the following experiments: Fieberling, NATRE, BBTRE 1996, BBTRE 1997, GRAVILUCK, LADDER, TOTO, DIMES-West, DIMES-DP. (b) Distribution of halocline averaged Re_B from a finescale parameterization of ε using CTD data presented in Chanona et al. (2018). (c) Map showing the locations of the data used in the histograms; red indicates microstructure data presented in Waterhouse et al. (2014), and blue indicates finescale data presented in Chanona et al. (2018).

seawater, and N is the buoyancy frequency; the nondimensional parameter Re_B is therefore a measure of the competing effects of turbulence (which acts to destabilize a flow and drive enhanced tracer fluxes) and viscosity and stratification (which act to dampen turbulence through friction and buoyancy effects). Larger Re_B indicate more energetic turbulence; smaller Re_B indicate increasingly damped turbulence. Past numerical and laboratory experiments suggest that turbulent diffusion ceases when $Re_B = \mathrm{O}(10)$ (e.g. Stillinger et al., 1983; Itsweire et al., 1993; Shih et al., 2005). What we present in this study are observations of enhanced turbulent-scale tracer variance over a broad range of Re_B values, including ones of order unity and smaller. Throughout this study, when we write "small Re_B", we mean $Re_B < 10$.

The finding from laboratory and numerical studies that turbulent diffusion ceases for $Re_B < 10$ is difficult to reconcile with field-based estimates of ocean mixing because this regime appears to be characteristic of much of the global ocean pycnocline, indicating that weak turbulent mixing in relatively strong stratification may be of global scale significance. Diffusivity estimates from various ocean microstructure experiments in the Atlantic, Pacific, and Southern Oceans—as collated by Waterhouse et al. (2014)—clearly indicate that Re_B is frequently of O(10) or smaller in the pycnocline (Figure 4.1a). In this data, 55% of measurements indicate that $Re_B < 10$, and 5% indicate that $Re_B < 1$. Similarly, in the Canadian Arctic, diffusivity estimates presented by Chanona et al. (2018) indicate that 43% of the western Arctic shelf and shelf-slope waters are characterized by $Re_B < 10$, and 3% are characterized by $Re_B < 1$ (Figure 4.1b). Despite this apparent propensity for small Re_B in the global ocean, it remains unclear how to best characterize water mass transformations and tracer fluxes in these conditions, and investigators employ differing techniques. For example, in Chanona et al. (2018), mixing rates for $Re_B < 20$ are set to molecular values (a similar approach to ours in Chapter 3) to account for the laboratory and numerical results mentioned above, whereas in Waterhouse et al. (2014), mixing rates are calculated from the Osborn model indiscriminately of Re_B considerations.

In this study, we analyze three aspects of low-Re_B ocean mixing using the data set we collected in the Beaufort Sea, described in Chapters 2 and 3. First, we characterize the degree of turbulent tracer variance (i.e. the Cox number) as a function of Re_B over multiple turbulence regimes, as defined by Ivey et al. (2008); we demonstrate how tracer variance in our measurements decreases, but never vanishes, as Re_B becomes small. Second, we compare diffusivity estimates from the Osborn (1980) model to diffusivity estimates obtained from the observed tracer variance, demonstrating how the two diverge as Re_B becomes small, an effect that is at least partially due to the differential diffusion of temperature and salinity when turbulence is weak. Finally, we estimate the efficiency of turbulent mixing from our data (where this is justified, i.e. for $Re_B > 10$) and compare these results to the classic Osborn model.

4.2 Methods

4.2.1 Measurements and ε Estimates

Data for this study are derived from a series of ocean hydrography and turbulence measurements that we collected in the Amundsen Gulf region of the Beaufort Sea in August 2015. They were collected continuously over 10 days from 348 quasi-vertical water column profiles, using an autonomous ocean glider in water 185–425 m deep, and were previously described in Chapters 2 and 3. The glider measures conductivity, temperature, and pressure with a Seabird SBE-41 pumped CTD; it measures shear microstructure and temperature microstructure with two Rockland Scientific SPM-38 and two Rockland Scientific FP07 probes, respectively. It glides through the water column at a nominal angle of 26° from the horizontal.

We derive estimates of the turbulent kinetic energy (TKE) dissipation rate, ε, in consecutive half-overlapping 40-s segments of measurement. Each of the four microstructure channels yields an independent ε estimate: shear-derived ε estimates are calculated by integrating power spectra of the measured shear variance; temperature-derived ε estimates are obtained by fitting theoretical Batchelor spectra to observed temperature gradient variance power spectra. The four independent estimates are subjected to a se-

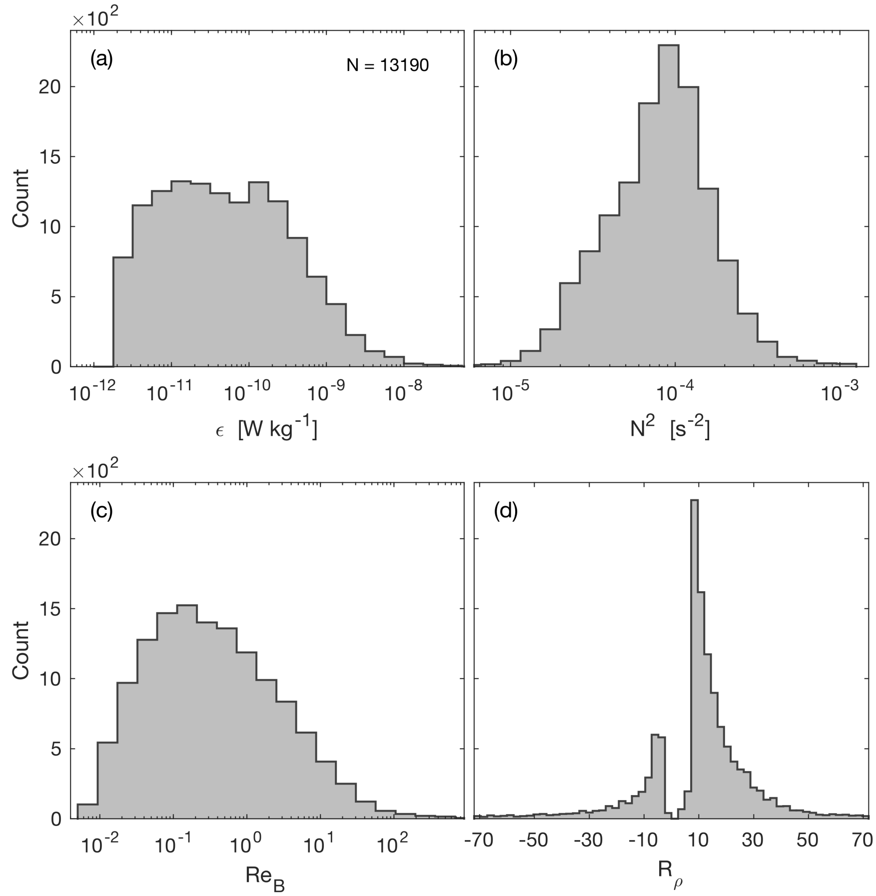

Figure 4.2 – Histograms for the measurements used in this study of (a) turbulent dissipation rate, ε, (b) squared buoyancy frequency, N^2, (c) buoyancy Reynolds number, Re_B, and (d) gradient density ratio, R_ρ. There are $\mathrm{N} = 13,190$ data.

ries of quality control routines to remove untrustworthy values and then combined into a single best ε estimate using the methodology described in Chapter 3. Details about measurement limitations, assumptions needed for the ε calculations, Fourier transform parameters, and the Batchelor-fitting algorithm are presented in Chapter 2; details about the quality control conditions are given in Appendix A.1.

Data for which no Cox number is available (Section 4.2.3) are discarded; data where ε is too small to estimate reliably (those set to zero in Chapter 3) are also discarded, leaving 13,190 estimates of ε for analysis. Remaining ε estimates vary between O(10^{-12}) and O(10^{-8}) W kg^{-1} (Figure 4.2a) and have a geometric mean of 5.1×10^{-11} W kg^{-1}, about an order of magnitude smaller than commonly observed in lower latitude open ocean environments (cf. Waterhouse et al., 2014). Stratification is strong throughout the measurements: the squared buoyancy frequency, N^2, is typically in the range 10^{-5} to 10^{-3} s^{-2} (Figure 4.2b), one to three orders of magnitude larger than is typical in the North Atlantic and North Pacific pycnoclines (Emery et al., 1984). Mean (standard deviation) temperature and salinity characteristics were $T = -0.68$ (0.50) °C and $S =$

33.6 (1.0) g kg^{-1}.

Combining estimates of ε and N^2, we calculate a buoyancy Reynolds number (Equation 4.1) for each data point. The combination of generally small ε and large N^2 lead to an Re_B distribution (Figure 4.2c) that is almost exclusively "small": of the 13,190 data, 12,396 (i.e. 94%) indicate $Re_B < 10$; only very few (82, or 0.6%) indicate $Re_B > 100$, the regime that Ivey et al. (2008) define as "energetic" turbulence.

4.2.2 Osborn Model

In the model proposed by Osborn (1980), the turbulent diapycnal density diffusivity is represented as

$$\kappa_\rho^{\mathrm{turb}} = \left(\frac{R_f}{1-R_f}\right)\frac{\varepsilon}{N^2} = \Gamma\frac{\varepsilon}{N^2} = \Gamma\,\nu Re_B\,, \tag{4.2}$$

where R_f is the efficiency of mixing (formally, the "flux Richardson number") and Γ is the dissipation flux coefficient. We evaluate $\kappa_\rho^{\mathrm{turb}}$ using the traditional upper-bound constant values $R_{f\mathrm{o}} = 0.17$ and $\Gamma_\mathrm{o} = 0.2$ proposed by Osborn on a theoretical basis and on the basis of then-current lab experiments. The Osborn model is developed from the turbulent kinetic energy equation for a stationary flow with zero flux divergence, assuming kinetic energy production at turbulent scales is balanced by a loss to dissipation (thermal energy) and a buoyancy flux (potential energy). In practice, it further depends on the assumptions of isotropy and homogeneity required to create the ε estimates (Chapter 2). The efficiency R_f can be interpreted as the fraction of turbulent energy production converted to a buoyancy flux.

When estimating mixing rates in Chapter 3, we followed the standard observational oceanography approach and assumed that the net diapycnal diffusivity of density, K_ρ, can be represented purely by the turbulent flux; i.e. we assumed $K_\rho \approx \kappa_\rho^{\mathrm{turb}}$. Then, based on recommendations by Ivey et al. (2008), we set K_ρ to the molecular diffusion rate of density—which we modelled as

$$\kappa_\rho^{\mathrm{mol}} = \frac{R_\rho\,\kappa_S^{\mathrm{mol}} - \kappa_T^{\mathrm{mol}}}{R_\rho - 1}\,, \tag{4.3}$$

under a linear equation of state assumption—when Re_B was less than 10. The parameters $\kappa_T^{\mathrm{mol}} = 1.4\times10^{-7}$ m^2 s^{-1} and $\kappa_S^{\mathrm{mol}} = 1.0\times10^{-9}$ m^2 s^{-1} are the molecular diffusion rates of temperature and salinity, respectively. The parameter R_ρ is the gradient density ratio,

$$R_\rho \equiv \frac{\beta\,(\partial S_\mathrm{A}/\partial z)}{\alpha\,(\partial T/\partial z)}\,, \tag{4.4}$$

which quantifies the relative contributions of salinity and temperature to the local density gradient (Figure 4.2). The factors α and β in Equation 4.4 are the coefficients for thermal expansion and haline contraction of seawater, respectively.

However, in the real ocean, the true density diffusivity is more accurately modelled as a superposition of the molecular and turbulent diffusion rates,

$$K_\rho = \kappa_\rho^{\text{mol}} + \kappa_\rho^{\text{turb}} \tag{4.5}$$

over the full Re_B parameter space, with a continuous transition between when $\kappa_\rho^{\text{turb}}$ or κ_ρ^{mol} is dominant. Because one of the goals of this present chapter is to assess the behaviour of the Osborn model in the small-Re_B part of the parameter space, we here calculate K_ρ using Equation 4.5 irrespective of a critical Re_B criterion. Fundamentally, this approach is more physical—and, as we will show in Section 4.3, better matches the observations—but it is encumbered by uncertainties in the Osborn model when Re_B is small, as we will discuss in Section 4.4.2. We will refer to Equation 4.5 as the modified Osborn model.

4.2.3 Temperature Variance Method: The Osborn-Cox Model

The net diathermal temperature diffusivity is

$$K_T = \kappa_T^{\text{mol}} + \kappa_T^{\text{turb}}, \tag{4.6}$$

where κ_T^{turb} is the turbulent component of the temperature diffusivity which is a function of the turbulent-scale temperature gradient variance (Winters and D'Asaro, 1996) and can be expressed as

$$\kappa_T^{\text{turb}} = \kappa_T^{\text{mol}} C. \tag{4.7}$$

This representation is known as the Osborn-Cox model (Osborn and Cox, 1972). Here, the factor C, the Cox number, is the ratio of turbulent gradient-variance to mean gradient-variance, which we calculate from the microstructure temperature measurements according to

$$C \equiv \frac{3\left\langle(\partial T'/\partial x)^2\right\rangle}{(\Delta T/\Delta z)^2}. \tag{4.8}$$

In the limit of no turbulence $C \to 0$. The factor of 3 assumes isotropic turbulence, angle brackets indicate ensemble averaging, x is the glider's along-path coordinate, and z is the vertical coordinate. We calculate the turbulent gradient-variance $\left\langle(\partial T'/\partial x)^2\right\rangle$ in detrended 40-s segments of measurement by averaging power spectra from 19 half-overlapping 4-s subsegments and integrating over all wavenumbers that have a measurable signal. The mean vertical gradient-variance $(\Delta T/\Delta z)^2$ is calculated over each 40-s segment. The spatial length of the 4-s subsegments effectively defines the largest turbulent length scale we consider and is dependent on the glider's instantaneous speed through water; the mean (standard deviation) spatial length of the 4-s subsegments is 1.19 (0.34) m. Note that the turbulent-scale and mean gradients need not be taken in the same direction since we assume turbulent gradients are statistically isotropic; the mean gradient, however, is not isotropic and must be taken in the vertical since we assume this the direction in which the mean gradient is largest. Equation 4.8 is ill-defined when the background temperature gradient approaches zero; consequently, we calculate C only when $|\Delta T/\Delta z| \geq 2 \times 10^{-3}$ °C m^{-1}.

Unlike ε, the Cox number is a quantity that we can observe directly using the temperature measurements. It can be interpreted geometrically as a measure of how much a turbulent flow field has strained a mean background gradient, and it does not rely on the stationarity and non-divergence assumptions required to relate ε to the microstructure measurements in the Osborn model (Winters and D'Asaro, 1996). Likewise, Equation 4.7 is independent of assumptions about the efficiency of mixing or the dynamics of the flow; it states only that the turbulent diffusion rate of the temperature tracer is proportional to the degree of turbulent-scale strain in the temperature field. Consequently, we expect the theoretical framework behind the temperature variance approach to be physically tractable for all Re_B and encumbered only by the assumption of isotropic gradients, which increases the uncertainty in C when turbulence is modified by stratification.

It is important to note that temperature is largely passive in the conditions observed here: mean thermal expansion and haline contraction coefficients for our data are $\alpha = 3.7 \times 10^{-5}$ °C^{-1} and $\beta = 7.8 \times 10^{-4}$ (g/kg)$^{-1}$ respectively, indicating that density is to first order set by salinity. As a consequence, temperature and density are not expected to diffuse at the same rate when turbulence is too weak to fully mask the two-order of magnitude difference between the molecular diffusivities of temperature and salinity. Note also that, by substituting Equation 4.7 into Equation 4.6,

$$C + 1 = \frac{K_T}{\kappa_T^{\mathrm{mol}}} \equiv K^* ; \tag{4.9}$$

that is, $C+1$ characterizes the net temperature diffusivity (turbulent + molecular) scaled by the molecular diffusivity and can therefore be interpreted as the degree of turbulent diffusivity enhancement. We henceforth refer to this nondimensional diffusivity as K^*.

4.2.4 Idealized Turbulence: Isotropy

The estimation of ε (and therefore Re_B, $\kappa_\rho^{\mathrm{turb}}$, and Γ) and the application of the Temperature Variance Method (Section 4.2.3) assume spatially homogeneous turbulence that is statistically stationary in time and spatially isotropic. None of these assumptions are truly met for measurements in the real ocean (Gregg, 1987, Section 7), adding uncertainty to all oceanic mixing estimates, but the isotropy assumption (which is required because we measure 2 of 9 shear components, and 1 of 3 of temperature gradient components) proves to be particularly problematic because it effectively requires that dissipation-scale eddies are immune to the buoyancy effects that arise from density stratification, which becomes increasingly untrue as stratification strengthens and turbulence weakens. Field measurements by Gargett et al. (1984) found that buoyancy effects modify turbulence at dissipative scales for $Re_B < 200$. For context, 94.1% of data in Figure 4.1a, 90.9% of data in Figure 4.1b, and 99.7% of data in Figure 4.2c are smaller than this criterion.

The degree of uncertainty associated with the departure from isotropy is unclear, but it generally appears to be within the bounds of "typical" uncertainties associated with oceanic turbulence measurements, which are often about a factor of 2–3 for statistical quantities and a factor of 5–10 for individual measurements. Field measurements of multiple shear components by Yamazaki and Osborn (1990) indicate that errors in ε estimates due to anisotropy are negligible for $Re_B > 20$ and are limited to less than 35% at smaller Re_B (the smallest value they report is $Re_B = 2$). Numerical simulations by Itsweire et al. (1993) indicate that errors in ε are within a factor of 2–4 in the range $50 < Re_B < 650$, and ones by Smyth and Moum (2000) indicate that anisotropy is negligible for $Re_B > 100$. A theoretical analysis by Rehmann and Hwang (2005) suggests that errors in ε due to anisotropy when $Re_B < \mathrm{O}(10)$ are limited to $\pm 33\%$ for unsheared turbulence and increases to a factor of 3 for sheared turbulence. In our own measurements (along an angled profile), we find no statistical distinction between the two measured shear components, indicating that errors due to anisotropy when comparing these two components is smaller than the scatter of the individual data, approximately a factor of 5 (Appendix A.1).

4.2.5 Other Diffusivity Models

Besides comparing K_T estimates to the modified Osborn model, we further compare with more recent models by Shih et al. (2005) and Bouffard and Boegman (2013), hereafter SKIF and BB. These are modified versions of the Osborn model that aim to account for variability in the characteristics of turbulent mixing when turbulence is either very weak or very strong. However, the traditional Osborn model remains the most commonly employed method for field measurements (cf. Gregg et al., 2018).

In the SKIF model, which is developed from direct numerical simulations, mixing is broken up into three regimes—molecular, intermediate, and energetic—using Re_B as a criterion to distinguish the regimes. In the intermediate regime, defined for the range $Re_B = 7$–100, diffusivity is represented by the traditional Osborn model (Equation 4.2), neglecting molecular diffusion. In the energetic regime, defined for $Re_B > 100$, diffusivity is represented by $K_\rho = 2\nu Re_B^{1/2}$. In the molecular regime, defined for $Re_B < 7$, diffusivity is represented by molecular diffusion only: $K_\rho = \kappa_\rho^{\mathrm{mol}}$.

The BB model, based on an empirical fit to results from multiple laboratory and numerical studies, is identical to the SKIF model but adds a transitional "buoyancy controlled" regime between the molecular and intermediate regimes. This regime is dependent on Prandtl number, Pr, and is bounded by $10^{2/3}Pr^{-1/2} < Re_B < (3\ln\sqrt{Pr})^2$; the purpose of including this regime in the model is to remedy the discontinuity that arises in the SKIF model between the molecular and intermediate regimes, at $Re_B = 7$. The BB model's diffusivity in this regime is represented by $K_\rho = (0.1\nu/Pr^{1/4})Re_B^{3/2}$. Note, we use $Pr = \nu/\kappa_T \approx 10$ for the Prandtl number definition, indicating that the buoyancy controlled regime is in the range $1.5 < Re_B < 11.9$.

4.2.6 Mixing Efficiency

For turbulent mixing, the efficiency of mixing, also known as the flux Richardson number, R_f, is the ratio of buoyancy flux (i.e. potential energy change) to turbulent kinetic energy production. The efficiency must, by definition, vary between 0 and 1. It is related to the flux coefficient in the Osborn model by

$$R_f = \frac{\Gamma}{1+\Gamma}. \tag{4.10}$$

If turbulent mixing is energetic enough that $\kappa_\rho^{\mathrm{turb}}$ and κ_T^{turb} are equal, and if molecular diffusion can be neglected, we can equate expressions (4.2) and (4.7) and write the flux coefficient as

$$\Gamma = \frac{\kappa_T^{\mathrm{mol}} C N^2}{\varepsilon}. \tag{4.11}$$

Expression 4.11 is valid if there is no differential diffusion of salinity and temperature (Gargett, 2003). There is no clearly defined regime transition below which differential diffusion becomes locally important to mixing, but based on results given in Ivey et al. (2008) and Jackson and Rehmann (2014), we calculate Γ and R_f only when $Re_B > 10$. Below this cutoff value, it is unlikely that Equation 4.11 is physically meaningful because the effects of molecular temperature and salinity diffusion are expected to be of first order importance to density transformations. Of our 13,190 data points, 794 satisfy the condition that $Re_B > 10$.

4.3 Results

4.3.1 Diffusivity Estimates

We present the nondimensionalized temperature diffusivity estimates derived from the Temperature Variance Method, K^*, as a function of Re_B in Figure 4.3a. Mode, arithmetic mean, and geometric mean values are shown in logarithmically-spaced bins along the Re_B axis. Predictions from Osborn (modified), SKIF, and BB models—all normalized by κ_T^{mol} to facilitate comparison with K^*—are also shown. As anticipated, the primary trend in the temperature diffusivity observations is that K^* increases with increasing Re_B, indicating greater turbulent diffusivity enhancement when turbulence is more intense and weaker enhancement—trending towards $K^* \to 1$ as $Re_B \to 0$ from the right—when turbulence is less intense. The modified Osborn model predicts the measurements most accurately and agrees with the mode and geometric mean values within a factor of 3 across all Re_B bins, tending to underestimate the measurements at $Re_B \geq 5$ and overestimate them at smaller Re_B. The mode value tracks the modified Osborn predictions most closely across Re_B bins and agrees with the model by better than a factor of 2 in all but three of the bins.

The observed trend that K^* most commonly approaches unity as turbulence weakens is not surprising; we expect that net diffusion reverts to molecular diffusion in the absence of turbulence. The more interesting part of Figure 4.3a is the large scatter that exists in K^*, especially in weak turbulence, because it indicates that substantially enhanced heat fluxes are, on average, possible even when turbulence is very weak and stratification is strong. The scatter in K^*—more specifically, the long tail in the distribution of K^* at any given Re_B—works to drive up the average heat flux from the idealized models by at least an order of magnitude across all observed Re_B. Even in the lowest bin, centred on $Re_B = 1.5 \times 10^{-2}$, the temperature diffusivity averaged across all data in the bin is enhanced by a factor of 11 over the molecular diffusion coefficient κ_T^{mol}.

The net diffusivities of density and temperature, estimated from the modified Osborn model (Equation 4.5) and the temperature-variance method (Equation 4.6), respectively, diverge systematically with decreasing Re_B. This trend can be seen in Figure 4.3b, where we plot the ratio K_T/K_ρ as a function of Re_B. In the most energetic observations, when $Re_B > 100$, the agreement between the two methods is a factor of 2.2 (geometric mean value), indicating that the diffusivity prediction from the modified Osborn model matches the observed temperature diffusion rate reasonably well. The best agreement occurs at the bin centred on $Re_B = 7.5$, where the two estimates agree within a factor of 1.1 (geometric mean values). However, as Re_B decreases further, the disagreement between the two diffusivity estimates increases: at $Re_B = 1$, the geometric mean ratio

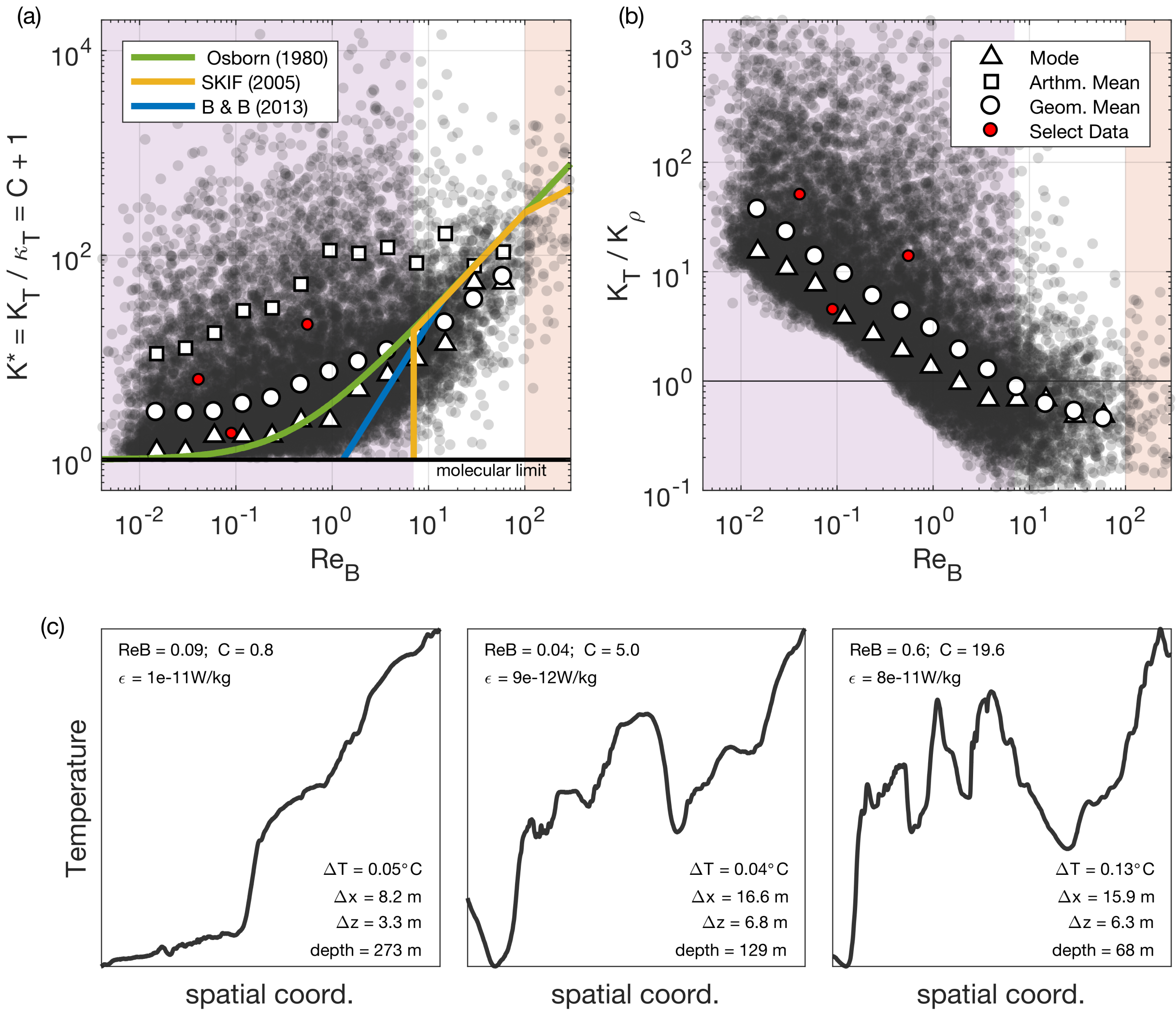

Figure 4.3 – (a) Scatterplot of the nondimensionalized net temperature diffusivity, K_T/κ_T, as a function of buoyancy Reynolds number, Re_B. White symbols indicate mode, arithmetic mean, and geometric mean in logarithmically spaced Re_B bins. Models from Osborn (1980, modified), Shih et al. (2005), and Bouffard and Boegman (2013) are shown for reference, all normalized by κ_T^{mol} to facilitate comparison with K^*. The three red data points are select—but in no way remarkable—points for which the raw temperature microstructure records are shown below. The three turbulence regimes proposed by Ivey et al. (2008)—molecular, transitional, and energetic—are indicated by the background shading—purple, white, and orange, respectively. (b) The ratio of the net temperature diffusivity (Equation 4.6) to the net diffusivity calculated from the modified Osborn model (Equation 4.5). Symbols as in panel a, excepting the arithmetic mean which is omitted here because it is not informative. (c) The microstructure temperature records used to calculate the three select data points (red) in panels a and b. Each record represents 40 s of measurement, spanning an along-path distance Δx, a vertical distance Δz, and a temperature difference ΔT between the first and last measurements. For each 40-s segment of measurement, one temperature gradient spectrum is calculated by averaging spectra from 19 half-overlapping 4-s subsegments (Section 4.2.3).

between the two is 3.0; at $Re_B = 0.1$, the geometric mean ratio is 9.5; and at $Re_B = 0.01$, the geometric mean ratio is 37. The physical interpretation is that the Osborn model becomes increasingly unsuccessful at predicting the observed temperature diffusivity as Re_B becomes small. That said, it is important to recognize that K_ρ and K_T should not generally be expected to be equal as turbulence weakens because temperature and salinity diffuse at differing rates when molecular diffusion is important. The implications of this point, together with the appropriate interpretation of the results seen in Figure 4.3b, are discussed further in Section 4.4.2.

The red markers in Figures 4.3a and 4.3b are three selected data points for which the measured 40-s microstructure temperature records are shown (Figure 4.3c). The parameters ε, Re_B, and C are indicated in each respective panel for these three records. The increase in temperature gradient variance from left to right is obvious to the eye as C increases from O(0.1) to O(1) to O(10), but gradient variance is notably visible in all three panels. The three examples are representative of nearby data in the Re_B–K^* space and are not otherwise remarkable. They are presented in order to exemplify what representative temperature structure looks like in the raw measurements when Re_B is O(0.1) or O(0.01) and to highlight that the temperature variance we observe in this small-Re_B regime is a real signal, not instrument noise or data processing artifact. Note, the microstructure temperature probes used for the measurements have a time response of $\sim$0.01 s and are sensitive to better than 10^{-4} °C, scales much smaller than those relevant to the gradients in Figure 4.3c.

4.3.2 Mixing Efficiency

A histogram of the flux coefficient estimates we infer from the subset of measurements where $Re_B > 10$ is shown in Figure 4.4a. These vary between $\Gamma = 0.001$–99, though 90% are in the range 0.01–0.71; the interquartile range is 0.05–0.19. The geometric mean value is 0.09, and the median value is 0.10, indicating that typical values from our data set are about a factor of 2 smaller than the canonical upper bound value $\Gamma_o = 0.2$ proposed by Osborn (1980).

We observe no statistically significant dependence of Γ on Re_B in the range $Re_B = 10$–100, but there is a clear trend towards decreasing Γ in the range $Re_B = 100$–1000. To identify this behaviour, we calculate median and geometric mean values of Γ in logarithmically-spaced bins of Re_B (Figure 4.4b). For $Re_B < 100$, the binned geometric mean values are in the range 0.08–0.09 with no clear trend and geometric standard error factors less than 1.5. The two bins centred on $Re_B = 240$ and $Re_B = 520$ indicate geometric mean Γ values of 0.06 and 0.02 respectively. The uncertainty in the sample mean increases with larger Re_B because there are fewer data points here, and in the largest bin

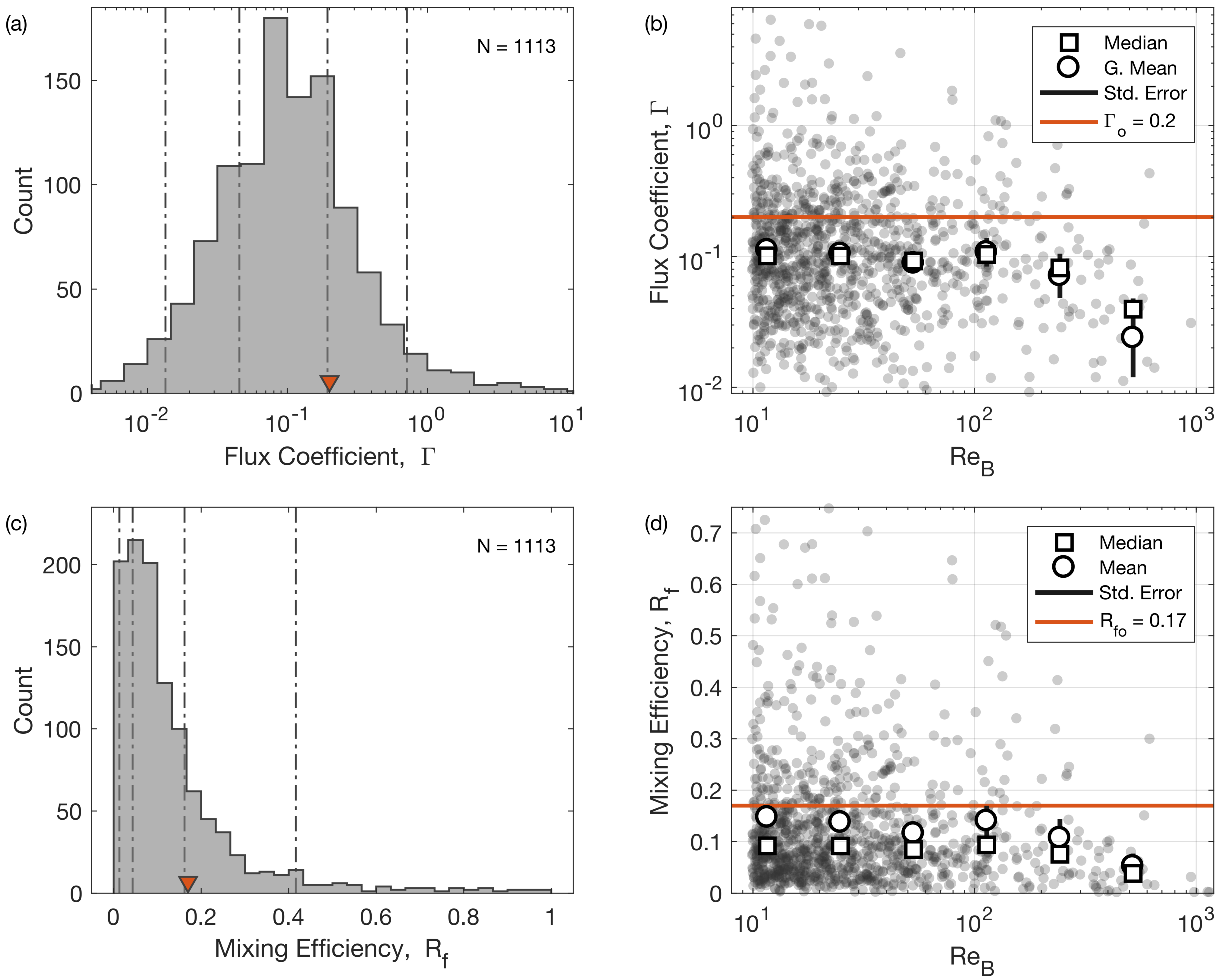

Figure 4.4 – (a) Histogram of flux coefficient estimates for the subset of data where $Re_B > 10$. Dash-dotted lines indicate percentiles 5, 25, 75, and 95. The red triangle indicates the canonical value proposed by Osborn (1980). N indicates the number of data points. (b) Flux coefficient plotted as a function of Re_B. Large open-faced symbols are the median and geometric mean values in geometrically-spaced bins. Error bars indicate the geometric standard error in the mean, calculated from two geometric standard deviations. (c) As in panel a, but for mixing efficiency, R_f. (d) As in panel b, but for R_f and with arithmetic mean values and standard errors in place of geometric ones.

(at $Re_B = 520$), the geometric standard deviation factor is 2.0.

Our estimates of the mixing efficiency, R_f, vary between 0.00 and 1.00 (Figure 4.4c). The central 90% of data is in the range 0.01–0.42, and the interquartile range is 0.04–0.16. Our estimates are smaller than the canonical value $R_{fo} = 0.17$ in 77% of the data. The mode and median values are 0.05 and 0.09, respectively, and the arithmetic mean is 0.13.

As with the Γ estimates, median and mean values of R_f in bins of Re_B indicate that there is no statistically significant trend in R_f when $Re_B \leq 100$ (Figure 4.4d); in this subset, the binned mean values of R_f are in the narrow range 0.12–0.15, with standard error of

0.03 or less. For $Re_B > 100$, there is a statistically significant trend towards less efficient mixing as Re_B increases, and in the highest bin ($Re_B = 520$), the mixing efficiency is 0.05 ± 0.02.

4.4 Summary and Discussion

In Section 4.3, we presented results from our case study of mixing characteristics in the weakly turbulent, strongly stratified Beaufort Sea. These can be summarized into three key findings:

- We frequently observed substantial turbulent-scale (O(1)–O(100) cm) temperature diffusivity enhancement in a low-Re_B regime where models of shear-driven turbulent mixing based on laboratory and numerical studies have previously suggested that tracer fluxes should be strictly molecular.
- The commonly employed Osborn model, even when modified to account for molecular diffusion, does not accurately predict temperature diffusivities in our observations. The degree by which it underestimates K_T increases systematically with decreasing Re_B and is as large as a factor of $\sim$40 for the smallest observed Re_B values.
- Mixing efficiency estimates from our data in intermediate and energetic regimes are highly variable and span the full range from 0 to 1; however, in general they appear to be about a factor of 2 smaller than the canonical value $R_{f\text{o}} = 0.17$ when $10 < Re_B \leq 100$, and they decrease further at larger Re_B.

In this section, we discuss each of these three findings in turn, addressing implications that arise from our results, uncertainties in the methods, and some recommendations for future study.

4.4.1 Enhanced Heat Fluxes

From a shear-driven turbulence point-of-view, the turbulent temperature gradient variance we frequently observed at very small Re_B is unexpected, as highlighted by the difference between the mean K^* estimates and the predictions from the Osborn, SKIF, and BB models (Figure 4.3a). The observed micro-scale structure was unexpected not only because laboratory and numerical studies have found that shear-driven turbulent mixing typically ceases below $Re_B \approx 10$, but also because Re_B values below unity are difficult to interpret dynamically. The length scales of the largest and smallest eddies in stratified turbulence are given by the Ozmidov and Kolmogorov length scales, $L_O = (\varepsilon/N^3)^{1/2}$ and $L_K = (\nu^3/\varepsilon)^{1/4}$, the ratio of which is proportional to Re_B:

$$Re_B = \frac{\varepsilon}{\nu N^2} = \left(\frac{L_O}{L_K}\right)^{4/3}. \tag{4.12}$$

An Re_B value less than unity suggests the absence of a classical cascade of energy from large to small turbulent eddies. Interpreted energetically, it suggests that there is insufficient kinetic energy in the turbulent flow field to create a density overturn through the given background stratification. It seems unlikely, then, that the turbulent-scale gradients we observed in this study can be described by the idealized model of shear-driven, isotropic turbulence (Section 4.2.4).

A number of mechanisms outside of shear-driven, isotropic turbulence may be responsible for the enhanced temperature gradient variance (and associated heat fluxes) seen in our measurements. The most obvious mechanism that may contribute to the enhanced heat fluxes is double diffusion, since large portions of the Beaufort Sea thermocline are well known to be susceptible to double diffusion (Timmermans et al., 2008a). We did not observe an obvious double diffusive staircase in our measurements (Chapter 3), but the gradient density ratio, R_ρ, is conducive to double diffusive convection in at least a portion of the observations (Figure 4.2). Focusing on a low-Re_B subset of the data, we find that $1 < R_\rho < 10$ in 21% of data for which $Re_B < 0.1$. This characterization indicates that double diffusion may play an important role in creating the observed gradient variance, but it also clearly suggests that double diffusion is not the sole dominant mechanism contributing to the enhanced heat fluxes.

Another possibility is that at least a portion of the enhanced gradient variance we observe at small Re_B is a remnant feature of some previous, more energetic, turbulence event. A simple scaling argument confirms that the timescale needed for molecular diffusion to naturally smooth the observed gradients is large enough that this could be a realistic possibility. For example, in the middle panel of Figure 4.3c, where $C = 5$ and the dissipation rate of temperature variance is $\chi = 2\kappa_T C\,(\Delta T/\Delta z)^2 = 6.5\times10^{-11}$ K^2 s^{-1}, the timescale $\mathcal{T}$ for diffusion to destroy a turbulent temperature anomaly of O(0.01) K is about $\mathcal{T} = \Delta T^2/\chi = 328$ days. However, again, it seem unlikely that all the temperature structure we observe is a remnant from some previous, more energetic turbulence event because we would not expect that a remnant temperature-gradient signal would decrease systematically with Re_B, as we see it does in Figure 4.3a. The systematic nature of this trend, rather, is consistent with a dynamic process relating C and Re_B, suggesting that the creation and sustenance of microstructure gradients becomes less pronounced when turbulence is weaker.

A final possible mechanism that may contribute to the observed enhanced gradient variance at small Re_B is shear-driven turbulence similar to that considered by the Osborn model, but not isotropic; the concept is one of anisotropic turbulent eddies that are actively dissipating energy but are vertically squashed by stratification. Such eddies have previously been coined "pancake" eddies because buoyancy constraints result in turbulence dynamics that are more pronounced in isopycnal directions than in the diapycnal one (e.g. Riley and Lelong, 2000; Lindborg and Fedina, 2009). One problem with this theory is that we do not actually observe anisotropy from the two perpendicular shear components that we measure (see Appendix A.1, Figure A.1), but this may be because the shear measurements begin to lose their reliability when dissipation rates are smaller than 10^{-10} W kg^{-1} (Chapter 2).

In reality, it is probably most likely that no single mechanism is responsible for the enhanced heat fluxes at small Re_B, but that they are created by some combination of the mechanisms described here.

4.4.2 Applicability of the Osborn Model

In Figure 4.3, we found good agreement between the direct K_T estimates (Equation 4.6) and the modified Osborn model's K_ρ estimates (Equation 4.5) when $Re_B > 10$. However, as Re_B becomes smaller, the modified Osborn model is no longer able to predict K_T, and the K_ρ and K_T estimates typically diverge by a factor of $\sim$37 (geometric mean) when $Re_B = \mathrm{O}(0.01)$. There are at least two distinct reasons for this divergence, one physical and one an artifact of the Osborn model, the effects of which are convoluted in the final K_T/K_ρ results.

The first consideration is that, physically, we should not expect K_T and K_ρ to be equal when turbulence is weak. When turbulence is strong, the turbulent components of K_T and K_ρ are equal and dominant over their molecular analogues, and temperature and density diffuse at the same rate. However, in the limit of no turbulence, $K_T \to \kappa_T^{\mathrm{mol}}$ and $K_\rho \to \kappa_\rho^{\mathrm{mol}}$, and (from Equation 4.3) the ratio K_T/K_ρ approaches

$$\frac{\kappa_T^{\mathrm{mol}}}{\kappa_\rho^{\mathrm{mol}}} = \frac{\kappa_T^{\mathrm{mol}}(R_\rho - 1)}{R_\rho\, \kappa_S^{\mathrm{mol}} - \kappa_T^{\mathrm{mol}}} = \frac{140\,(R_\rho - 1)}{R_\rho - 140}. \tag{4.13}$$

For the R_ρ regime represented by our data, the magnitude of $\kappa_T^{\mathrm{mol}}/\kappa_\rho^{\mathrm{mol}}$ is typically in the range 5 – 72 (central 90%; median value 13), suggesting that a significant component of the signal seen in Figure 4.3b at low Re_B is caused by the effects of differential diffusion of temperature and salinity. Previous studies, from the laboratory and from numerical simulations, appear to see the onset of differential diffusion at $Re_B \approx 100$ (Gregg et al., 2018), indicating that nearly all our measurements may be susceptible to the effects of differential diffusion (Figure 4.2c).

The second consideration is that the physical basis underlying the Osborn model becomes increasingly intractable as Re_B becomes small. This fact is in part due to the breakdown of isotropy, discussed in Section 4.4.1, and in part due to the assumption that the efficiency of diapycnal mixing remains constant in very weak turbulence. This latter point especially is concerning because it seems unlikely that a significant fraction of turbulent kinetic energy is converted to a buoyancy flux when stratification inhibits the overturning of a dissipation-scale eddy (i.e. when $Re_B < 1$). However, it remains unclear what the best representation for the mixing efficiency is in this regime, and there appears to be no consensus for a justifiable alternative to using $R_{fo} = 0.17$ when interpreting field measurements generally (Gregg et al., 2018).

Synthesizing these two points, we conclude that the application of the modified Osborn model to our data (Figure 4.3b) largely replicates the trend one would expect to see for the transition between turbulence and laminar flow. In the limit of energetic turbulence ($Re_B > 100$), diffusion rates of temperature and density are equal. In the limit of damped turbulence ($Re_B \ll 1$), differential diffusion rates of temperature and salinity cause the ratio K_T/K_ρ to diverge systematically. However, the exact behaviour of K_T/K_ρ in our data is also almost certainly influenced by uncertainties in the theoretical framework of the Osborn model which, unfortunately, preclude us from suggesting a functional form for the behaviour of differential diffusion in our data. It is, however, clear that $\kappa_\rho^{\mathrm{turb}}$, as estimated by the Osborn model (Equation 4.2), should not be used to predict heat fluxes or other passive tracer fluxes in low-Re_B regimes like the Beaufort Sea without accounting for the potential effects of differential diffusion or comparison to results from directly measured micro-scale temperature gradients. It should be limited to making predictions of density diffusivity.

4.4.3 Mixing Efficiency in High Stratification

Estimating the efficiency of mixing for turbulence in the ocean is precarious business, as highlighted in review articles by Ivey et al. (2008) and, more recently, Gregg et al. (2018). Not only are the many assumptions that lead to Equation 4.11—isotropic, homogeneous, stationary flow; negligible differential diffusion; all measurements normal to microstructure gradients—unrealistically constrained for field measurements, but there is also a large degree of natural variability in R_f depending on the stage of a turbulent billow and, potentially, the mechanisms driving turbulence. The definitions for "mixing efficiency" are not the same across numerical, laboratory, and field studies, making comparisons difficult, and there is little convergence between results. Even among observational studies there is little agreement: the 14 previous studies reviewed by Gregg et al. (2018) typically found Γ in the range 0.1–0.3, leading the authors to suggest continued use of $\Gamma_o = 0.2$ until a better consensus emerges.

The large variability in our Γ and R_f data is likely due to a combination of the natural variability and the errors and uncertainties described above. However, the trends seen in Figure 4.4 appear to be robust and there are enough data that the uncertainty in the sample mean in each Re_B-bin, at least, is generally small. Our finding that $\Gamma \approx 0.1$ in most of our data is, therefore, either physical and the result of atypical mixing characteristics, or it is an artifact that arises from a systematic bias in our techniques. The uncertainties in estimating Γ certainly allow for the possibility that there is a systematic bias, but we cannot isolate this effect in our measurements, if it is present. We do know, however, that our measurements are distinguished from previous estimates of Γ by locale and stratification conditions. Many previous studies about mixing efficiency do not report Re_B—the ones that do mostly report $Re_B \sim \mathrm{O}(10^2)$ or $Re_B \sim \mathrm{O}(10^3)$—but it appears that nearly all previous oceanic estimates of Γ come from mid- or low latitudes, where N^2 tends to be an order of magnitude or more smaller than in the Beaufort Sea. One northern study, by Peterson and Fer (2014), using measurements from Faroe Bank, did report Γ in similar Re_B conditions to those we report here and, unlike us, found larger than expected mixing efficiencies when Re_B was small: the authors reported $\Gamma \approx 0.6$ in the range $Re_B = 5$–100. Still, compared to the overwhelming majority of observational stratified turbulence studies, our situation is unique, and so it is important that future studies continue to examine mixing characteristics in Arctic-like conditions because accurate estimates of Arctic Ocean mixing are an important strategic component for modelling present and future climate change in northern latitudes (Carmack et al., 2015). Specifically, we recommend future observational studies in the Arctic report R_f and Γ alongside Re_B, where possible, in order to build a record of mixing efficiency estimates in similar strongly stratified, weakly turbulent environments.

Chapter 5

Conclusion

5.1 Goals and Representativeness of the Thesis

In Section 1.2, I defined the objectives of this thesis under three categories:

i. measuring turbulence when turbulence is weak and stratification is strong,
ii. characterizing turbulent mixing in the Arctic Ocean's Amundsen Gulf, and
iii. understanding enhanced heat fluxes in strongly stratified, weakly turbulent environments.

In the following section, I synthesize the results of my research to respond to the questions I initially posed for each of these categories, in turn.

Before doing so, however, it is worth pausing briefly to reflect on how the results of my work do—and do not—translate to the broader fields of Arctic oceanography and turbulent ocean mixing. After all, the results presented here stem from measurements taken in a particular region of the Beaufort Sea, at a particular time of the year, over a span of only 10 days, and a word on their representativeness is needed.

I anticipate that Chapter 2 is generalizable to glider-based microstructure measurements in all regions where turbulence is weak and stratification dominates the turbulent dynamics. The methods and insights I propose are in no way unique to the Beaufort Sea and require only that the measurements be taken in a similar parameter space.

Chapter 3 is about ocean mixing in Amundsen Gulf in summer; it does not speak to ocean mixing in the Beaufort Sea or the wider Arctic Ocean more generally, nor does it address seasonal or interannual variability of ocean mixing. That said, I also anticipate that many of the key features that determine the physical mixing characteristics here are important at other times of the year and in other locales. For example, it is unlikely that there is substantial seasonal variability in the Atlantic-derived layers since the time scale for Atlantic Water to reach the Beaufort Sea is on the order of years, and seasonal signals that may have existed in this water mass when it was in the North Atlantic have largely diffused by the time it arrives at Amundsen Gulf (Rudels, 2015). Similarly, the dominant role of stratification over turbulence in setting vertical mixing translates to much of the western Arctic (e.g. Chanona et al., 2018), and recent work indicates that tidal flow is a dominant driver for turbulent mixing across the Arctic Ocean generally (Rippeth et al., 2015). Therefore, I think my results here may be viewed as a "high-resolution snapshot" that cannot generalize in all relevant circumstances but do reflect many relevant features of ocean mixing across the western Arctic.

The representativeness of Chapter 4 is probably the most challenging to ascertain. On one hand, the results in this chapter are presented in a way that is decoupled from the locale of the measurements, and my hope is that they spur further investigation in more generalized settings. However, fundamentally, the results we deduced from those measurements cannot in good conscience be divorced from the study site in which they were taken since we do not know what mechanisms created the enhanced temperature variance we observed. In light of that uncertainty, I think it is safest to defer a judgement on the representability of the results of Chapter 4 to other ocean sites until future studies can reproduce—or provide a rebuttal to—the conclusions I drew here.

5.1.1 Observing weak turbulence in strong stratification

a. *Do sensor limitations hinder the ability to formulate meaningful ε estimates in these conditions?*

   Yes, they do, especially for the shear probes, whose measurements are liable to be influenced by a noise floor below which no meaningful shear signal can be detected. We found that as much as 70% of the shear-derived ε estimates were influenced by the noise floor of the shear probes. For the temperature measurements, we did not find that a sensor limitation hindered our ability to formulate meaningful ε estimates in weak turbulence, though it is known that in strong turbulence the measurement quality suffers from slow response times (e.g. Gregg, 1999).

b. *In what conditions and to what extent do sensor limitations impact the ability to measure ε? And, what is the impact of those limitations on the interpretation of the measurements?*

The quality of our shear measurements was limited by the intensity of the turbulence. We found that shear-derived estimates of ε were useful to values as small as 3×10^{-11} W kg^{-1}, which we defined as the noise floor of the shear-based measurement. In our observations, 58% of the measurements appeared to be below this threshold. A more conservative approach to choosing a noise floor would be to consider the threshold where sensor limitations first begin to statistically skew the distribution of the ε estimates. We found this threshold to be 1×10^{-10} W kg^{-1}; as many as 70% of our measurements were below this threshold.

The arithmetic mean of a large sample of shear-based ε estimates from a coastal or otherwise energetic site in the ocean is probably affected only weakly by errors in small ε values because the arithmetic mean will be dominated by the few large ε values on the right-hand-side of the sample distribution (assuming the distribution spans many orders of magnitude). However, the disproportionate importance of the large ε values becomes less dominant as ε becomes less variable, and it seems likely that arithmetic mean ε calculations will be skewed for data from near quiescent environments like e.g. the abyssal ocean or deep stratified lakes. Geometric average calculations, which characterize the central tendency of a distribution, will be skewed heavily if ε is generally small, e.g. by up to two orders of magnitude in the measurements presented in this thesis.

c. *How are uncertainties in ε estimates impacted when turbulence is weak and stratification is strong and the assumptions of isotropic, homogeneous, steadily forced turbulence becomes increasingly intractable?*

Power spectra of temperature gradients and velocity shear deviate systematically from their reference shapes with decreasing Re_B, presumably in large part due to the breakdown of the isotropy, homogeneity, and stationarity assumptions. Uncertainty in ε estimates increases gradually as result. We determined that our ε estimates (from temperature measurements) were useful and physically meaningful for $\varepsilon > 2 \times 10^{-12}$ W kg^{-1} which corresponds, approximately, to $Re_B \geq \mathrm{O}(10^{-2})$ in our measurements.

5.1.2 Turbulent mixing in the Arctic Ocean's Amundsen Gulf

a. *What are the turbulence and mixing characteristics in the Amundsen Gulf region of the Beaufort Sea? Can we develop statistical metrics of ε and turbulent diffusivity, K_ρ, and describe their spatial and temporal variability?*

   Turbulence and turbulent mixing in Amundsen Gulf are typically weak and dominated by buoyancy effects resulting from stratification. A typical dissipation rate, given by the geometric mean of the whole data set, is $\varepsilon = 2.8 \times 10^{-11}$ W kg^{-1}. The arithmetic mean diffusivity from all the data is $K_\rho = 4.5 \times 10^{-6}$ m^2 s^{-1}. Buoyancy Reynolds number considerations indicate that a turbulent density flux is not expected in 93% of the observations because density stratification prohibits diapycnal overturning. Variability in ε spans 5 orders of magnitude; variability in K_ρ spans 3 orders of magnitude, not accounting for the large subset of measurements where diffusion is expected to be molecular. Turbulence appears to be surface- and bottom enhanced and varies most strongly at the tidal M2 frequency.

b. *What is the magnitude of vertical heat fluxes associated with turbulent mixing in Amundsen Gulf? Is it significant when compared to mean heat budget estimates of the region and in light of recent increases in sea ice loss?*

   Vertical heat fluxes are typically small, especially through the Warm Halocline layer overlying the warm Atlantic Water layer, sequestering the heat in that lower layer. The mean flux through the Warm Halocline is 0.03 W m^{-2}, negligible in comparison to the Arctic Ocean-wide mean of 6.7 W m^{-2}. Heat fluxes are enhanced where turbulence is more energetic and in the vicinity of a warm-core mesoscale eddy seen in the observations. The magnitude of the heat flux is greater than 10 W m^{-2} in 0.6% of observations.

c. *What physical mechanisms are responsible for the observed turbulence and mixing characteristics in this region?*

   To first order, it appears that turbulent mixing in the deeper Warm Halocline and Atlantic Water layers is modulated in time by barotropic tidal flow over nearby complex topography. Surprisingly, double diffusion does not appear to be a dominant contributor to mixing through the Warm Halocline. In the Pacific Water layer and Cold Halocline, the presence of a warm core mesoscale eddy dominated local heat fluxes. Diapycnal density mixing remained generally low in these layers during our measurements, due primarily to the presence of very strong stratification.

5.1.3 Enhanced heat fluxes in strongly stratified, weakly turbulent environments

a. *Can we observe the transition between turbulent and molecular diffusion in the real ocean when turbulence weakens and stratification remains strong?*

It appears that we can. Our measurements indicate a strong relationship between the degree of turbulent diffusivity enhancement, K^*, and the buoyancy Reynolds number, Re_B. We observed a continuous transition between dominantly turbulent temperature diffusivity ($K^* > 100$) and near-molecular temperature diffusivity ($K^* = \mathrm{O}(1)$) as Re_B decreases from O(100), through unity, to O(10^{-2}).

b. *How do predictions of turbulent mixing from models compare to our observations of tracer variance when turbulence is weak and stratification is strong?*

The Osborn, SKIF, and BB models predict the observed diffusivity well when turbulence is reasonably energetic, i.e. in the range $Re_B = 10$–100. At lower Re_B, the SKIF and BB models predict pure molecular diffusion for parts of the Re_B parameter space where observations indicate a turbulent diffusivity with $K^* = \mathrm{O}(10)$. Part of the reason for this discrepancy is that the SKIF and BB models preclude a smooth transition between turbulent and molecular fluxes. The Osborn model more accurately predicts this transition and the observed diffusivities at low Re_B, if Osborn's original formulation for the turbulent flux is superimposed onto a molecular component (i.e. as in Equation 4.5). However, predictions of density diffusivity from the Osborn model diverge from the observed temperature diffusivity by a factor of ~ 37 at small Re_B; this divergence is most likely due to the onset of differential diffusion of salinity and temperature, which is not encapsulated by the Osborn model.

c. *How efficient is turbulent mixing in our observations, and how does this efficiency compare to the canonical value of 20%?*

We were able to estimate the efficiency of mixing when $Re_B > 10$, and found values for R_f and Γ that generally were a factor of ~ 2 smaller than the canonical values proposed by Osborn (1980). Observed median values were $R_f = 0.09$ and $\Gamma = 0.10$. There was little trend with Re_B in the range $Re_B = 10$–100; there appeared to be a decreasing trend for $Re_B > 100$, but fewer data in this regime increased the statistical uncertainty.

5.2 The Bigger Picture: Looking Ahead

It is my sincere hope that the research I've presented in this PhD thesis will one day contribute to a comprehensive understanding of how ocean mixing in the Beaufort Sea contributes to modulating Arctic climate and ecology, and that that knowledge will be incorporated into governance policies that will preserve the integrity of the region's ecosystems for future generations. This aim, the conservation of Arctic ecosystems and their biodiversity, is the underlying driver that motivated me to do this work and oceanography in the Arctic, more generally. And even though my research is, admittedly, a small contribution towards that end goal, I feel it is important to maintain sight of the larger motivation and to propose how my results might inform future research that will bring that underlying goal closer to reality. I will try to carry out that final task of my thesis here by outlining in what ways I hope my own work will fit into the larger scope of Arctic oceanography in the future.

The immediate goal of studying mixing in the Arctic Ocean is to generate an understanding of how, and by what mechanisms, tracers such as heat, oxygen, and nutrients are distributed throughout its basins. The applications of that understanding are far reaching, even if they are still a work in progress, and they are almost always tied to predictive capabilities and the effects of modern climate change: predicting where and how quickly perennial sea ice is lost (Carmack et al., 2015); predicting changes to stratification conditions in the Canada Basin (Davis et al., 2016); predicting changes to community composition and ecological dynamics, especially in light of a changing flaw lead system (Barber et al., 2010). In each case, there is a community-wide goal to develop models that can describe the present state and make accurate predictions about future changes, usually with an eye to informing responsible governance.

Models of mixing for the Arctic Ocean—present or future—must always be informed by measurements of the environment to remain grounded in reality. This necessity is the fundamental reason the science community invests in field campaigns in the Arctic despite the extreme costs and logistic difficulties of working in this challenging and remote environment. In some ways the investment is a losing battle because there is too much ocean and there are too few resources to sample sufficiently, but rapid development of autonomous platforms like gliders, Argo profilers[1], or ice-tethered profilers[2] (ITPs) are closing this gap. This area of progress is one of the most basic, but also most fundamental, ones in which I hope my work will inspire future Arctic oceanography, by demonstrating the feasibility and practicality of glider-based turbulence measurements

[1] see http://www.argo.ucsd.edu

[2] see https://www.whoi.edu/website/itp/overview

despite the harshness and remoteness of the environment. On Canada's eastern coast, the Ocean Tracking Network has within the last decade developed an unprecedented program to continuously sample the Scotian Shelf using a fleet of autonomous gliders, similar to the one used in this study. A similarly ambitious program of autonomous sampling is presently being developed on the west coast of Canada through the Pacific Robotic Ocean Observing Facility, again with the help of a new fleet of ocean gliders. In light of these precedents, it is not a stretch, then, to imagine a near future where a similar fleet of autonomous ocean gliders operates along Canada's northern coastal ocean as well, and if the experience of my work documented here contributes to that development, it will be a satisfying and worthwhile contribution indeed.

The other area in which I picture my research making an important contribution is with regards to the question of scaling up. Turbulence measurements are important because they give us the most direct estimates of mixing we can obtain in the real ocean, and the results of my thesis should be immediately applicable to future investigators wanting to measure turbulence in the Arctic Ocean. Questions about measurement limitation, regional mixing mechanisms, and stratified mixing models are considerations of first order importance for such work, and I hope my research presented here will help to inform many future high latitude turbulence studies. However, notwithstanding their importance, turbulence measurements are admittedly cumbersome—even from an autonomous platform—because they require sensors that are highly specialized, expensive, subject to low-frequency drift in their calibration, and prone to breaking. In addition, the very high temporal resolution needed to interpret turbulence measurements are energy-intensive in the field, resulting in reduced operating endurance, and the measurements produce vast datasets that are difficult to store and manage[3].

For these reasons, I imagine that future basin-scale maps of turbulent mixing observations in the Arctic will not be based on direct turbulence measurements, but on parameterizations using coarser-scale CTD measurements that are collected more easily in larger number and with larger geographic scope. In many cases the measurements from which mixing rates can be inferred on large scales already exist because of observing programs like the Woods Hole Oceanographic Institution's ITP program or ArcticNet's Amundsen Science Program, and the actual task of parameterizing mixing rates from those measurements has already begun. Chanona et al. (2018) recently published a study using a fine scale parameterization of internal wave signals to estimate mixing rates on the Beaufort Sea's coastal margin and in the Canadian Arctic Archipelago, and I know that a similar approach is being applied to Arctic Ocean-wide ITP measurements

[3]For example, the 10 days of measurements from a single glider used in this thesis produced 6 GB of binary data; once processed and converted to a useable format, the data required about 75 GB of storage.

as I write this. The approach has already been successfully applied to estimate global patterns of mixing for the rest of the world ocean by Whalen et al. (2012). Such parameterizations of turbulence based on coarser scale measurements are useful because they help us to quickly scale up our knowledge of mixing rates and infer large scale patterns of water mass transformations and heat fluxes. They are, however, parameterizations, and they need to be tested and calibrated against more direct estimates of mixing, where these are available. This is a topic for which I can see my results, especially those in Chapter 3, being especially useful because direct mixing rate estimates with statistically significant metrics are so rare in the Arctic. I hope that the large record of direct turbulence measurements I have established here, though regionally isolated, can be used to ground-truth parameterizations that can more easily scale up to basin scales and be used to address questions relevant to the scales of global climate. Answering such questions is a community effort, of course, and if my work contributes to it, it will be a contribution of which I will be proud.

Bibliography

W. N. Adger, J. Barnett, K. Brown, N. Marshall, and K. O'Brien. Cultural dimensions of climate change impacts and adaptation. *Nature Climate Change*, 3:112–117, Feb. 2013.

M. H. Alford. Redistribution of energy available for ocean mixing by long-range propagation of internal waves. *Nature*, 423(6936):159, May 2003.

ArcticNet. Amundsen Science Mooring Data Collection. Long-Term Ocean Observatory (LTOO) oceanographic mooring data collected in the Canadian Arctic Beaufort Sea. Processed Data. Soon archived at `www.polardata.ca`, Canadian Cryospheric Information Network, Waterloo, Canada, 2018. Accessed from `amundsen.data@as.ulaval.ca` on 28 Aug 2018.

N. C. Asselin, D. G. Barber, I. Stirling, S. H. Ferguson, and P. R. Richard. Beluga (Delphinapterus leucas) habitat selection in the eastern Beaufort Sea in spring, 1975–1979. *Polar Biology*, 34:1973–1988, Apr. 2011.

M. A. Baker and C. H. Gibson. Sampling Turbulence in the Stratified Ocean: Statistical Consequences of Strong Intermittency. *Journal of Physical Oceanography*, 19:1817–1836, May 1987.

D. G. Barber, M. G. Asplin, Y. Gratton, J. V. Lukovich, R. J. Galley, R. L. Raddatz, and D. Leitch. The International polar year (IPY) circumpolar flaw lead (CFL) system study: Overview and the physical system. *Atmosphere-Ocean*, 48:225–243, 2010.

G. K. Batchelor. Small-scale variation of convected quantities like temperature in turbulent fluid: Part 1. General discussion and the case of small conductivity. *Journal of Fluid Mechanics*, 5:113–133, Jan. 1959.

F. Berkes and D. Jolly. Adapting to Climate Change: Social-Ecological Resilience in a Canadian Western Arctic Community. *Conservation Ecology*, 5:18, Aug. 2001.

D. Bouffard and L. Boegman. A diapycnal diffusivity model for stratified environmental flows. *Dynamics of Atmospheres and Oceans*, 61-62:14–34, 2013.

D. Bourgault, C. Hamel, F. Cyr, J. É. Tremblay, P. S. Galbraith, D. Dumont, and Y. Gratton. Turbulent nitrate fluxes in the Amundsen Gulf during ice-covered conditions. *Geophysical Research Letters*, 38, Aug. 2011.

E. Carmack and R. W. MacDonald. Oceanography of the Canadian Shelf of the Beaufort Sea: A Setting for Marine Life. *Arctic*, 55:29–45, Apr. 2002.

E. Carmack, R. W. MacDonald, and J. E. Papadakis. Water mass structure and boundaries in the Mackenzie shelf estuary. *Journal of Geophysical Research*, 94: 18043–18055, May 1989.

E. Carmack, I. Polyakov, L. Padman, I. Fer, E. Hunke, J. Hutchings, J. Jackson, D. Kelley, R. Kwok, C. Layton, H. Melling, D. Perovich, O. Persson, B. Ruddick, M. L. Timmermans, J. Toole, T. Ross, S. Vavrus, and P. Winsor. Toward Quantifying the Increasing Role of Oceanic Heat in Sea Ice Loss in the New Arctic. *Bulletin of the American Meteorological Society*, 96:2079–2105, Dec. 2015.

M. Chanona, S. N. Waterman, and Y. Gratton. Variability of internal wave-driven mixing and stratification in the Canadian Arctic Ocean. *Journal of Geophysical Research: Oceans*, pages 1–45, Nov. 2018.

D. Cressey. Arctic melt opens Northwest passage. *Nature*, 449:267–267, Sept. 2007.

P. E. D. Davis, C. Lique, H. L. Johnson, and J. D. Guthrie. Competing Effects of Elevated Vertical Mixing and Increased Freshwater Input on the Stratification and Sea Ice Cover in a Changing Arctic Ocean. *Journal of Physical Oceanography*, 46: 1531–1553, May 2016.

D. L. Dickson and H. G. Gilchrist. Status of Marine Birds of the Southeastern Beaufort Sea. *Arctic*, 55:46–58, Nov. 2002.

T. M. Dillon and D. R. Caldwell. The Batchelor Spectrum and Dissipation in the Upper Ocean. *Journal of Geophysical Research: Oceans*, 85:1910–1916, Apr. 1980.

H. V. Dosser and L. Rainville. Dynamics of the Changing Near-Inertial Internal Wave Field in the Arctic Ocean. *Journal of Physical Oceanography*, 46(2):395–415, Feb. 2016.

H. V. Dosser, L. Rainville, and J. M. Toole. Near-Inertial Internal Wave Field in the Canada Basin from Ice-Tethered Profilers. *Journal of Physical Oceanography*, 44: 413–426, Feb. 2014.

W. J. Emery, W. G. Lee, and L. Magaard. Geographic and Seasonal Distributions of Brunt–Väisälä Frequency and Rossby Radii in the North Pacific and North Atlantic. *Journal of Physical Oceanography*, 14:294–317, Feb. 1984.

I. Fer. Near-Inertial Mixing in the Central Arctic Ocean. *Journal of Physical Oceanography*, 44:2031–2049, Aug. 2014.

I. Fer, A. K. Peterson, and J. E. Ullgren. Microstructure Measurements from an Underwater Glider in the Turbulent Faroe Bank Channel Overflow. *Journal of Atmospheric and Oceanic Technology*, 31:1128–1150, 2014.

E. C. Fine, J. A. MacKinnon, M. H. Alford, and J. B. Mickett. Microstructure Observations of Turbulent Heat Fluxes in a Warm-Core Canada Basin Eddy. *Journal of Physical Oceanography*, 48:2397–2418, Oct. 2018.

J. Ford, T. Pearce, B. Smit, J. Wandel, and M. Allurut. Reducing Vulnerability to Climate Change in the Arctic: The Case of Nunavut, Canada on JSTOR. *Arctic*, 2007.

J. D. Ford, B. Smit, and J. Wandel. Vulnerability to climate change in the Arctic: A case study from Arctic Bay, Canada. *Global Environmental Change*, 16:145–160, May 2006.

A. E. Gargett. Differential diffusion: an oceanographic primer. *Progress in Oceanography*, 56:559–570, Mar. 2003.

A. E. Gargett, T. R. Osborn, and P. W. Nasmyth. Local isotropy and the decay of turbulence in a stratified fluid. *Journal of Fluid Mechanics*, 144:231–280, July 1984.

C. Garrett and E. Kunze. Internal Tide Generation in the Deep Ocean. *Annual Review of Fluid Mechanics*, 39:57–87, Jan. 2007.

M. Geoffroy, D. Robert, G. Darnis, and L. Fortier. The aggregation of polar cod (Boreogadus saida) in the deep Atlantic layer of ice-covered Amundsen Gulf (Beaufort Sea) in winter. *Polar biology*, 34:1959–1971, May 2011.

C. H. Gibson. Fossil Turbulence and Intermittency in Sampling Oceanic Mixing Processes. *Journal of Geophysical Research*, 92:5383–5404, 1987.

L. Goodman, E. R. Levine, and R. G. Lueck. On Measuring the Terms of the Turbulent Kinetic Energy Budget from an AUV. *Journal of Atmospheric and Oceanic Technology*, 23:977–990, July 2006.

M. C. Gregg. Diapycnal mixing in the thermocline: A review. *Journal of Geophysical Research*, 92:5249–5286, May 1987.

M. C. Gregg. Uncertainties and Limitations in Measuring ε and χ_T. *Journal of Atmospheric and Oceanic Technology*, 16:1483–1490, Nov. 1999.

M. C. Gregg, M. H. Alford, H. Kontoyiannis, V. Zervakis, and D. Winkel. Mixing over the steep side of the Cycladic Plateau in the Aegean Sea. *Journal of Marine Systems*, 89:30–47, Jan. 2012.

M. C. Gregg, E. A. D'Asaro, J. J. Riley, and E. Kunze. Mixing Efficiency in the Ocean. *Annual Review of Marine Science*, 10:443–473, Jan. 2018.

J. D. Guthrie, J. H. Morison, and I. Fer. Revisiting internal waves and mixing in the Arctic Ocean. *Journal of Geophysical Research: Oceans*, 118:3966–3977, Aug. 2013.

J. D. Guthrie, I. Fer, and J. H. Morison. Thermohaline staircases in the Amundsen Basin: Possible disruption by shear and mixing. *Journal of Geophysical Research: Oceans*, 122:7767–7782, Oct. 2017.

L. A. Harwood and I. Stirling. Distribution of ringed seals in the southeastern Beaufort Sea during late summer. *Canadian Journal of Zoology*, 70:891–900, May 1992.

L. A. Harwood, P. Norton, B. Day, and P. A. Hall. The Harvest of Beluga Whales in Canada's Western Arctic: Hunter-Based Monitoring of the Size and Composition of the Catch. *Arctic*, 55:10–20, Nov. 2002.

P. L. Holtermann, R. Prien, M. Naumann, V. Mohrholz, and L. Umlauf. Deepwater dynamics and mixing processes during a major inflow event in the central Baltic Sea. *Journal of Geophysical Research: Oceans*, 122:6648–6667, Aug. 2017.

E. C. Itsweire, D. A. Briggs, J. H. Ferziger, and J. R. Koseff. Turbulence in Stratified Shear Flows: Implications for Interpreting Shear-induced Mixing in the Ocean. *Journal of Physical Oceanography*, 23:1508–1522, 1993.

G. N. Ivey, K. B. Winters, and J. R. Koseff. Density Stratification, Turbulence, but How Much Mixing? *Annual Review of Fluid Mechanics*, 40:169–184, Jan. 2008.

P. R. Jackson and C. R. Rehmann. Experiments on Differential Scalar Mixing in Turbulence in a Sheared, Stratified Flow. *Journal of Physical Oceanography*, 2014.

M. Jakobsson, L. Mayer, B. Coakley, J. A. Dowdeswell, S. Forbes, B. Fridman, H. Hodnesdal, R. Noormets, R. Pedersen, M. Rebesco, H. W. Schenke, Y. Zarayskaya, D. Accettella, A. Armstrong, R. M. Anderson, P. Bienhoff, A. Camerlenghi, I. Church, M. Edwards, J. V. Gardner, J. K. Hall, B. Hell, O. Hestvik, Y. Kristoffersen, C. Marcussen, R. Mohammad, D. Mosher, S. V. Nghiem, M. T. Pedrosa, P. G. Travaglini, and P. Weatherall. The International Bathymetric Chart of the Arctic Ocean (IBCAO) Version 3.0. *Geophysical Research Letters*, 39, June 2012.

M. O. Jeffries, J. E. Overland, and D. K. Perovich. The Arctic shifts to a new normal. *Physics Today*, 66:35–7, 2013.

D. E. Kelley, H. J. S. Fernando, A. E. Gargett, J. Tanny, and E. Özsoy. The diffusive regime of double-diffusive convection. *Progress in Oceanography*, 56:461–481, Mar. 2003.

V. C. Khon, I. I. Mokhov, M. Latif, V. A. Semenov, and W. Park. Perspectives of Northern Sea Route and Northwest Passage in the twenty-first century. *Climatic Change*, 100:757–768, 2010.

T. B. L. Kirkwood. Geometric Means and Measures of Dispersion. *Biometrics*, 35: 908–909, Aug. 1979.

O. Kocsis, H. Prandke, A. Stips, A. Simon, and A. Wüest. Comparison of dissipation of turbulent kinetic energy determined from shear and temperature microstructure. *Journal of Marine Systems*, 21:67–84, June 1999.

A. N. Kolmogorov. The Local Structure of Turbulence in Incompressible Viscous Fluid for Very Large Reynolds Numbers. *Dokl. Akad. Nauk. SSSR*, 30, 1941.

Z. Kowalik and J. B. Matthews. The M2 Tide in the Beaufort and Chukchi Seas. *Journal of Physical Oceanography*, 12:743–746, July 1982.

R. H. Kraichnan. Small-Scale Structure of a Scalar Field Convected by Turbulence. *Physics of Fluids*, 11:945–10, 1968.

E. A. Kulikov, A. B. Rabinovich, and E. Carmack. Barotropic and baroclinic tidal currents on the Mackenzie shelf break in the southeastern Beaufort Sea. *Journal of Geophysical Research*, 109:C05020, May 2004.

E. A. Kulikov, A. B. Rabinovich, and E. Carmack. Variability of baroclinic tidal currents on the Mackenzie Shelf, the Southeastern Beaufort Sea. *Continental Shelf Research*, 30:656–667, Apr. 2010.

B. J. Lincoln, T. P. Rippeth, Y.-D. Lenn, M.-L. Timmermans, W. J. Williams, and S. Bacon. Wind-driven mixing at intermediate depths in an ice-free Arctic Ocean. *Geophysical Research Letters*, 43:9749–9756, Sept. 2016.

E. Lindborg and E. Fedina. Vertical turbulent diffusion in stably stratified flows. *Geophysical Research Letters*, 36:2560–5, Jan. 2009.

R. G. Lueck. *RSI Technical Note 028 Calculating the Rate of Dissipation of Turbulent Kinetic Energy*. Rockland Scientific International, May 2016. Available online at http://rocklandscientific.com/support/knowledge-base/technical-notes/.

R. G. Lueck, F. Wolk, and H. Yamazaki. Oceanic Velocity Microstructure Measurements in the 20th Century. *Journal of Oceanography*, 58:153–174, 2002.

D. A. Luketina and J. Imberger. Determining Turbulent Kinetic Energy Dissipation from Batchelor Curve Fitting. *Journal of Atmospheric and Oceanic Technology*, 18: 100–113, Jan. 2001.

R. Lumpkin and K. Speer. Global Ocean Meridional Overturning. *Journal of Physical Oceanography*, 37:2550–2562, Oct. 2007.

J. MacKinnon. Oceanography: Mountain waves in the deep ocean. *Nature*, 501: 321–322, Sept. 2013.

J. A. MacKinnon, Z. Zhao, C. B. Whalen, A. F. Waterhouse, D. S. Trossman, O. M. Sun, L. C. St Laurent, H. L. Simmons, K. Polzin, R. Pinkel, A. Pickering, N. J. Norton, J. D. Nash, R. Musgrave, L. M. Merchant, A. V. Melet, B. Mater, S. Legg, W. G. Large, E. Kunze, J. M. Klymak, M. Jochum, S. R. Jayne, R. W. Hallberg, S. M. Griffies, S. Diggs, G. Danabasoglu, E. P. Chassignet, M. C. Buijsman, F. O. Bryan, B. P. Briegleb, A. Barna, B. K. Arbic, J. K. Ansong, and M. H. Alford. Climate Process Team on Internal Wave–Driven Ocean Mixing. *Bulletin of the American Meteorological Society*, 98:2429–2454, Nov. 2017.

T. J. McDougall and P. M. Barker. *Getting started with TEOS-10 and the Gibbs Seawater (GSW) Oceanographic Toolbox*. SCOR/IAPSO WG127, May 2011. ISBN 978-0-646-55621-5.

J. McGarrity and H. Gloystein. Northwest passage crossed by first cargo ship, the nordic orion, heralding new era of arctic commercial activity. *National Post*, September 2013. Available online at http://go.nature.com/jyN5dU.

R. McGhee. *Beluga hunters: An archaeological reconstruction of the history and culture of the Mackenzie Delta Kittegaryumiut*. Hull, Quebec: Canadian Museum of Civilization, 1988.

L. Merckelbach, D. Smeed, and G. Griffiths. Vertical Water Velocities from Underwater Gliders. *Journal of Atmospheric and Oceanic Technology*, 27:547–563, Mar. 2010.

L. Merckelbach, A. Berger, G. Krahmann, M. Dengler, and J. R. Carpenter. A Dynamic Flight Model for Slocum Gliders and Implications for Turbulence Microstructure Measurements. *Journal of Atmospheric and Oceanic Technology*, 36:281–296, Feb. 2019.

A. W. Miller and G. M. Ruiz. Arctic shipping and marine invaders. *Nature Publishing Group*, 4:413–416, June 2014.

E. Morozov and S. V. Pisarev. Internal tides at the arctic latitudes (Numerical experiments). *Oceanology*, 42:165–173, 2002.

W. Munk and C. Wunsch. Abyssal recipes II: energetics of tidal and wind mixing. *Deep Sea Research Part I: Oceanographic Research Papers*, 45:1977–2010, Dec. 1998.

P. W. Nasmyth. *Oceanic turbulence*. PhD thesis, University of British Columbia, British Columbia, Canada, 1970.

M. Nikurashin and R. Ferrari. Overturning circulation driven by breaking internal waves in the deep ocean. *Geophysical Research Letters*, 40:3133–3137, June 2013.

N. S. Oakey. Determination of the Rate of Dissipation of Turbulent Energy from Simultaneous Temperature and Velocity Shear Microstructure Measurements. *Journal of Physical Oceanography*, 12:256–271, Mar. 1982.

T. R. Osborn. Vertical Profiling of Velocity Microstructure. *Journal of Physical Oceanography*, 4:109–115, Jan. 1974.

T. R. Osborn. Estimates of the Local Rate of Vertical Diffusion from Dissipation Measurements. *Journal of Physical Oceanography*, 10:83–89, Jan. 1980.

T. R. Osborn and C. S. Cox. Oceanic fine structure. *Geophysical Fluid Dynamics*, 3: 321–345, Jan. 1972.

T. R. Osborn and W. R. Crawford. An Airfoil Probe for Measuring Turbulent Velocity Fluctuations in Water. In *Air-Sea Interaction*, pages 369–386. Springer, Boston, MA, Boston, MA, 1980.

L. Padman and T. M. Dillon. Vertical Heat Fluxes Through the Beaufort Sea Thermohaline Staircase. *Journal of Geophysical Research*, 92:10799–10806, Sept. 1987.

M. R. Palmer, G. R. Stephenson, M. E. Inall, C. Balfour, A. Düsterhus, and J. A. M. Green. Turbulence and mixing by internal waves in the Celtic Sea determined from ocean glider microstructure measurements. *Journal of Marine Systems*, 144:57–69, Apr. 2015.

A. K. Peterson and I. Fer. Dissipation measurements using temperature microstructure from an underwater glider. *Methods in Oceanography*, 10:44–69, Sept. 2014.

I. K. Peterson, S. J. Prinsenberg, and J. S. Holladay. Observations of sea ice thickness, surface roughness and ice motion in Amundsen Gulf. *Journal of Geophysical Research*, 113:1170–14, June 2008.

A. J. Plueddemann and J. T. Farrar. Observations and models of the energy flux from the wind to mixed-layer inertial currents. *Deep-Sea Research Part II*, 53(1-2):5–30, Jan. 2006.

K. L. Polzin, J. M. Toole, J. R. Ledwell, and R. W. Schmitt. Spatial Variability of Turbulent Mixing in the Abyssal Ocean. *Science*, 276:93–96, Apr. 1997.

K. L. Polzin, A. C. Naveira Garabato, T. N. Huussen, B. M. Sloyan, and S. N. Waterman. Finescale parameterizations of turbulent dissipation. *Journal of Geophysical Research: Oceans*, 119:1383–1419, Feb. 2014.

E. Post, M. C. Forchhammer, M. S. Bret-Harte, T. V. Callaghan, T. R. Christensen, B. Elberling, A. D. Fox, O. Gilg, D. S. Hik, T. T. Høye, R. A. Ims, E. Jeppesen, D. R. Klein, J. Madsen, A. D. McGuire, S. Rysgaard, D. E. Schindler, I. Stirling, M. P. Tamstorf, N. J. C. Tyler, R. van der Wal, J. Welker, P. A. Wookey, N. M. Schmidt, and P. Aastrup. Ecological Dynamics Across the Arctic Associated with Recent Climate Change. *Science*, 325:1355–1358, Sept. 2009.

T. D. Prowse, C. Furgal, R. Chouinard, H. Melling, D. Milburn, and S. L. Smith. Implications of Climate Change for Economic Development in Northern Canada: Energy, Resource, and Transportation Sectors. *AMBIO: A Journal of the Human Environment*, 38:272–281, July 2009.

T. Radko. *Double-Diffusive Convection*. Cambridge University Press, 2013. doi: 10.1017/CBO9781139034173.

L. Rainville and P. Winsor. Mixing across the Arctic Ocean: Microstructure observations during the Beringia 2005 Expedition. *Geophysical Research Letters*, 35, Apr. 2008.

L. Rainville and R. A. Woodgate. Observations of internal wave generation in the seasonally ice-free Arctic. *Geophysical Research Letters*, 36, Dec. 2009.

L. Rainville, C. Lee, and R. Woodgate. Impact of Wind-Driven Mixing in the Arctic Ocean. *Oceanography*, 24:136–145, Sept. 2011.

C. R. Rehmann and J. H. Hwang. Small-Scale Structure of Strongly Stratified Turbulence. *Journal of Physical Oceanography*, 35:151–164, Feb. 2005.

W. E. Ricker. Linear Regressions in Fishery Research. *Journal Fisheries Research Board of Canada*, 30:409–434, Jan. 1973.

J. J. Riley and M.-P. Lelong. Fluid Motions in the Presence of Strong Stable Stratification. *Annual Review of Fluid Mechanics*, 32:613–657, Nov. 2000.

T. P. Rippeth, B. J. Lincoln, Y.-D. Lenn, J. A. M. Green, A. Sundfjord, and S. Bacon. Tide-mediated warming of Arctic halocline by Atlantic heat fluxes over rough topography. *Nature Geoscience*, 8:191–194, Feb. 2015.

T. P. Rippeth, V. Vlasenko, N. Stashchuk, B. D. Scannell, J. A. M. Green, B. J. Lincoln, and S. Bacon. Tidal Conversion and Mixing Poleward of the Critical Latitude (an Arctic Case Study). *Geophysical Research Letters*, 67:705–9, Dec. 2017.

B. Ruddick, A. Anis, and K. Thompson. Maximum Likelihood Spectral Fitting: The Batchelor Spectrum. *Journal of Atmospheric and Oceanic Technology*, 17: 1541–1555, Nov. 2000.

B. Rudels. Arctic Ocean circulation, processes and water masses: A description of observations and ideas with focus on the period prior to the International Polar Year 2007–2009. *Progress in Oceanography*, 132:22–67, Mar. 2015.

D. L. Rudnick. Ocean Research Enabled by Underwater Gliders. *Annual Review of Marine Science*, 8:519–541, Jan. 2016.

J. L. Sarmiento, N. Gruber, M. A. Brzezinski, and J. P. Dunne. High-latitude controls of thermocline nutrients and low latitude biological productivity. *Nature*, 427:56–60, 2004.

B. Scheifele, R. Pawlowicz, T. Sommer, and A. Wüest. Double Diffusion in Saline Powell Lake, British Columbia. *Journal of Physical Oceanography*, 44:2893–2908, Nov. 2014.

B. Scheifele, S. N. Waterman, L. Merckelbach, and J. R. Carpenter. Measuring the Dissipation Rate of Turbulent Kinetic Energy in Strongly Stratified, Low-Energy Environments: A Case Study From the Arctic Ocean. *Journal of Geophysical Research: Oceans*, 19:1817–22, Aug. 2018.

L. K. P. Schultze, L. M. Merckelbach, and J. R. Carpenter. Turbulence and Mixing in a Shallow Shelf Sea From Underwater Gliders. *Journal of Geophysical Research: Oceans*, 122:9092–9109, 2017.

M. C. Serreze and R. G. Barry. Processes and impacts of Arctic amplification: A research synthesis. *Global and Planetary Change*, 77:85–96, May 2011.

C. Sévigny, Y. Gratton, and P. S. Galbraith. Frontal structures associated with coastal upwelling and ice-edge subduction events in southern Beaufort Sea during the Canadian Arctic Shelf Exchange Study. *Journal of Geophysical Research: Oceans*, 120:2523–2539, Apr. 2015.

W. J. Shaw and T. P. Stanton. Vertical diffusivity of the Western Arctic Ocean halocline. *Journal of Geophysical Research: Oceans*, 119:5017–5038, Aug. 2014.

W. J. Shaw, T. P. Stanton, M. G. McPhee, J. H. Morison, and D. G. Martinson. Role of the upper ocean in the energy budget of Arctic sea ice during SHEBA. *Journal of Geophysical Research*, 114:C06012, June 2009.

N. C. Shibley and M. L. Timmermans. The Formation of Double-Diffusive Layers in a Weakly Turbulent Environment. *Journal of Geophysical Research: Oceans*, 121: 457–14, Mar. 2019.

N. C. Shibley, M. L. Timmermans, J. R. Carpenter, and J. M. Toole. Spatial variability of the Arctic Ocean's double-diffusive staircase. *Journal of Geophysical Research: Oceans*, 122:980–994, 2017.

L. H. Shih, J. R. Koseff, G. N. Ivey, and J. H. Ferziger. Parameterization of turbulent fluxes and scales using homogeneous sheared stably stratified turbulence simulations. *Journal of Fluid Mechanics*, 525:193–214, Feb. 2005.

E. L. Shroyer. Turbulent Kinetic Energy Dissipation in Barrow Canyon. *Journal of Physical Oceanography*, 42:1012–1021, June 2012.

E. L. Shroyer, J. D. Nash, A. F. Waterhouse, and J. N. Moum. Measuring Ocean Turbulence. In *Observing the Oceans in Real Time*, pages 99–122. Springer International Publishing, 2017.

W. Smyth. Dissipation-range geometry and scalar spectra in sheared stratified turbulence. *Journal of Fluid Mechanics*, 401:209–242, Dec. 1999.

W. Smyth and J. N. Moum. Anisotropy of turbulence in stably stratified mixing layers. *Physics of Fluids*, 12:1343–1362, June 2000.

T. Sommer, J. R. Carpenter, M. Schmid, R. G. Lueck, M. Schurter, and A. Wüest. Interface structure and flux laws in a natural double-diffusive layering. *Journal of Geophysical Research: Oceans*, 118:1–15, Nov. 2013a.

T. Sommer, J. R. Carpenter, M. Schmid, R. G. Lueck, and A. Wüest. Revisiting Microstructure Sensor Responses with Implications for Double-Diffusive Fluxes. *Journal of Atmospheric and Oceanic Technology*, 30:1907–1923, Aug. 2013b.

L. St Laurent and S. Merrifield. Measurements of Near-Surface Turbulence and Mixing from Autonomous Ocean Gliders. *Oceanography*, 30:116–125, June 2017.

J. V. Steinbuck, M. T. Stacey, and S. G. Monismith. An Evaluation of χ_T Estimation Techniques: Implications for Batchelor Fitting and ε. *Journal of Atmospheric and Oceanic Technology*, 26:1652–1662, Jan. 2009.

D. C. Stillinger, K. N. Helland, and C. W. Van Atta. Experiments on the transition of homogeneous turbulence to internal waves in a stratified fluid. *Journal of Fluid Mechanics*, 131:91–122, June 1983.

I. Stirling. The Biological Importance of Polynyas in the Canadian Arctic . *Arctic*, 33: 303–315, Jan. 1980.

I. Stirling. Polar bears and seals in the eastern Beaufort Sea and Amundsen Gulf: a synthesis of population trends and ecological relationships over three decades. *Arctic*, 55:59–76, 2002.

G. I. Taylor. Statistical Theory of Turbulence. *Proceedings of the Royal Society of London. Series A, Mathematical and Physical Scienes*, 151:421–444, July 1935.

M. L. Timmermans, J. Toole, R. Krishfield, and P. Winsor. Ice-Tethered Profiler observations of the double-diffusive staircase in the Canada Basin thermocline. *Journal of Geophysical Research*, 113:C00A02, Jan. 2008a.

M. L. Timmermans, J. Toole, A. Proshutinsky, R. Krishfield, and A. Plueddemann. Eddies in the Canada Basin, Arctic Ocean, Observed from Ice-Tethered Profilers. *Journal of Physical Oceanography*, 38:133–145, Feb. 2008b.

J.-É. Tremblay, Y. Gratton, J. Fauchot, and N. M. Price. Climatic and oceanic forcing of new, net, and diatom production in the North Water. *Deep Sea Research Part II: Topical Studies in Oceanography*, 49:4927–4946, Jan. 2002.

J. S. Turner. The Melting of Ice in the Arctic Ocean: The Influence of Double-Diffusive Transport of Heat from Below. *Deep Sea Research*, 40:249–256, Mar. 2010.

A. F. Waterhouse, J. A. MacKinnon, J. D. Nash, M. H. Alford, E. Kunze, H. L. Simmons, K. L. Polzin, L. C. S. Laurent, O. M. Sun, R. Pinkel, L. D. Talley, C. B. Whalen, T. N. Huussen, G. S. Carter, I. Fer, S. N. Waterman, A. C. N. Garabato, T. B. Sanford, and C. M. Lee. Global Patterns of Diapycnal Mixing from Measurements of the Turbulent Dissipation Rate. *Journal of Physical Oceanography*, 44:1854–1872, July 2014.

C. B. Whalen, L. D. Talley, and J. A. MacKinnon. Spatial and temporal variability of global ocean mixing inferred from Argo profiles. *Geophysical Research Letters*, 39 (18):2643–6, Sept. 2012.

W. J. Williams and E. Carmack. Combined effect of wind-forcing and isobath divergence on upwelling at Cape Bathurst, Beaufort Sea. *Journal of marine research*, 66:1–19, Feb. 2008.

W. J. Williams and E. Carmack. The interior shelves of the Arctic Ocean: Physical oceanographic setting, climatology and effects of sea-ice retreat on cross-shelf exchange. *Progress in Oceanography*, 139:24–41, Dec. 2015.

W. J. Williams, E. Carmack, K. Shimada, H. Melling, K. Aagaard, R. W. Macdonald, and R. Grant Ingram. Joint effects of wind and ice motion in forcing upwelling in Mackenzie Trough, Beaufort Sea. *Continental Shelf Research*, 26:2352–2366, Dec. 2006.

K. B. Winters and E. A. D'Asaro. Diascalar flux and the rate of fluid mixing. *Journal of Fluid Mechanics*, 317:179–193, 1996.

F. Wolk, H. Yamazaki, L. Seuront, and R. G. Lueck. A New Free-Fall Profiler for Measuring Biophysical Microstructure. *Journal of Atmospheric and Oceanic Technology*, 19:780–793, Apr. 2002.

F. Wolk, R. G. Lueck, and L. St Laurent. Turbulence Measurements from a Glider. *13th Workshop on Physical Processes in Natural Waters, Proceedings*, July 2009.

H. Yamazaki and R. Lueck. Why Oceanic Dissipation Rates Are Not Lognormal. *Journal of Physical Oceanography*, 20:1907–1918, Dec. 1990.

H. Yamazaki and T. Osborn. Dissipation Estimates for Stratified Turbulence. *Journal of Geophysical Research: Oceans*, 95:9739–9744, June 1990.

M. Zhao and M.-L. Timmermans. Vertical scales and dynamics of eddies in the Arctic Ocean's Canada Basin. *Journal of Geophysical Research: Oceans*, 120:8195–8209, Dec. 2015.

Appendix

A.1 Quality Control Measures for Dissipation Rate Estimates

Here we describe the quality control procedures we apply to the measurements to identify dissipation rate estimates deemed untrustworthy. These are removed before the analysis described in Section 2.4.

Before implementing quantitative quality control measures, we remove any obviously contaminated measurements by hand. These include all measurements after Aug 27 from one of the two shear probes because the probe appears to have been damaged at this point and thereafter no longer measured a sensible signal. We then begin systematic quality control measures with 45,571 independent ε_U estimates and 63,507 independent ε_T estimates. Note that the estimates from the two distinct shear or two distinct temperature probes are not yet averaged at this stage (see Sections 2.3.2 and 2.3.3).

Table A.1 – Quality control parameters, as defined in the text. Percentages are the fraction of measurements flagged by each condition.

	ε_U	ε_T
N before QC	45,571	63,507
QC1	9.8%	10.3%
QC2	13.6%	13.2%
QC3	2.7%	17.0%
QC4	3.5%	4.1%
QC5-U	13.2%	—
QC6-T	—	5.6%
QC7-T	—	4.6%
One or more	22.3%	33.9%
N after QC	35,395	41,955

Individual estimates of ε_U and ε_T are flagged untrustworthy and removed if they satisfy one or more of the following conditions:

QC1 The magnitude of the glider's acceleration $|d\mathcal{U}/dt|$ is above the tenth percentile ($|d\mathcal{U}/dt| > 4.6 \times 10^{-4}$ m/s^2). This is a heuristic measure, but it satisfactorily isolates measurements where the glider appears to be changing speed over the span of one ε estimate. The data processing assumes $\mathcal{U}$ is constant over the span of an ε estimate.

QC2 The glider is within 15 m of an inflection point. When the glider inflects, the angle of attack and the estimate of $\mathcal{U}$ are uncertain and mechanical vibrations from the glider contaminate measurements.

QC3 Estimates from two identical probes differ by greater than a factor of 10. For shear, the higher estimate is removed. For temperature, both estimates are removed.

QC4 The ratio $\mathcal{U}/(\varepsilon/N)^{1/2}$ is less than 5. This is the ratio between the glider's velocity and an estimate of the turbulent flow velocities (Fer et al., 2014) and may indicate when Taylor's frozen turbulence hypothesis is violated.

In addition, ε_U measurements are flagged and removed if

QC5-U The maximum of the nondimensionalized shear spectrum Φ^*, defined in Section 2.5.2, is greater than twice the peak of the nondimensionalized Nasmyth spectrum. This isolates shear spectra obviously contaminated at low wavenumbers.

In addition, ε_T measurements are flagged and removed if

QC6-T The sum of the correction terms χ_{lw} and χ_{hw} (see Equation 2.7) is greater than the "observed" term χ_{obs}.

QC7-T There are fewer than 6 distinct wavenumbers available in the closed interval $[k_l, k_u]$. This ensures a reasonable minimum number of spectral points to which to fit a Batchelor spectrum.

Cumulatively, quality assessment conditions flag and remove 22.3% of individual ε_U measurements and 33.9% of individual ε_T measurements. The percentage of measurements flagged by each individual condition is given in Table A.1.

Beyond these conditions, confidence in the measurements may be indicated by the level of agreement between duplicate measurements of ε_U and ε_T. This comparison is favourable: after the quality assessment procedures, 96% of 6,820 coincident sets of ε_U measurements agree within a factor of 5, and the agreement is comparable over the full range of ε_U. Note that a factor of 5 is typically considered reasonable agreement for individual microstructure measurements which often scatter within an order of magnitude and can vary by more than 10 decades in the ocean. The comparison is slightly more variable but still favourable for ε_T, where 87.3% of 20,378 coincident sets agree

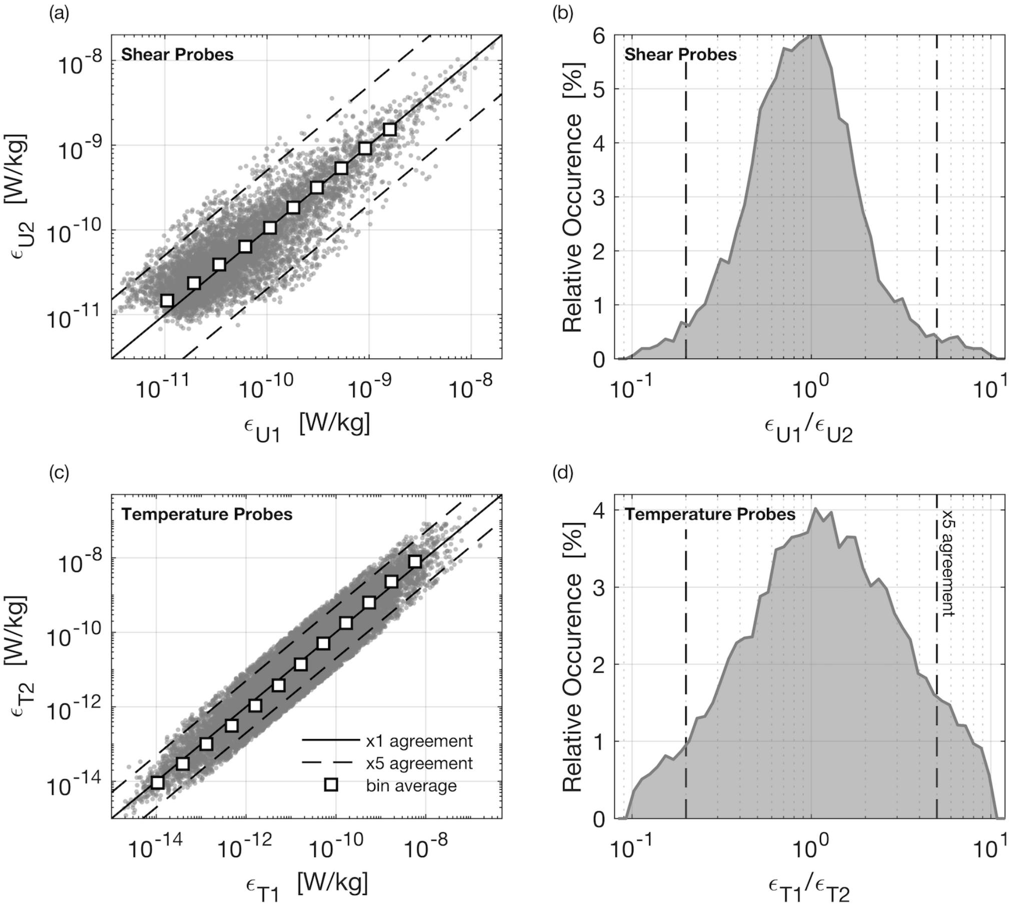

Figure A.1 – Comparison of results from individual (a,b) shear probes and (c,d) temperature probes. Bin averages are calculated as in Figure 2.6. Agreement within a factor of 5 is indicated in all panels by the dashed lines.

within a factor of 5 and there is likewise no trend with ε_T.

The comparisons are imaged in Figure A.1, where subscripts 1 and 2 are arbitrarily designated to measurements from distinct probes. Bin averages are calculated as in Figure 2.6.

Following the quality control procedures described here, we average (using an arithmetic mean) results for each of the two distinct sets of measurements, as described in Sections 2.3.2 and 2.3.3. This leaves $28,575$ ε_U and $21,577$ ε_T estimates for analysis.

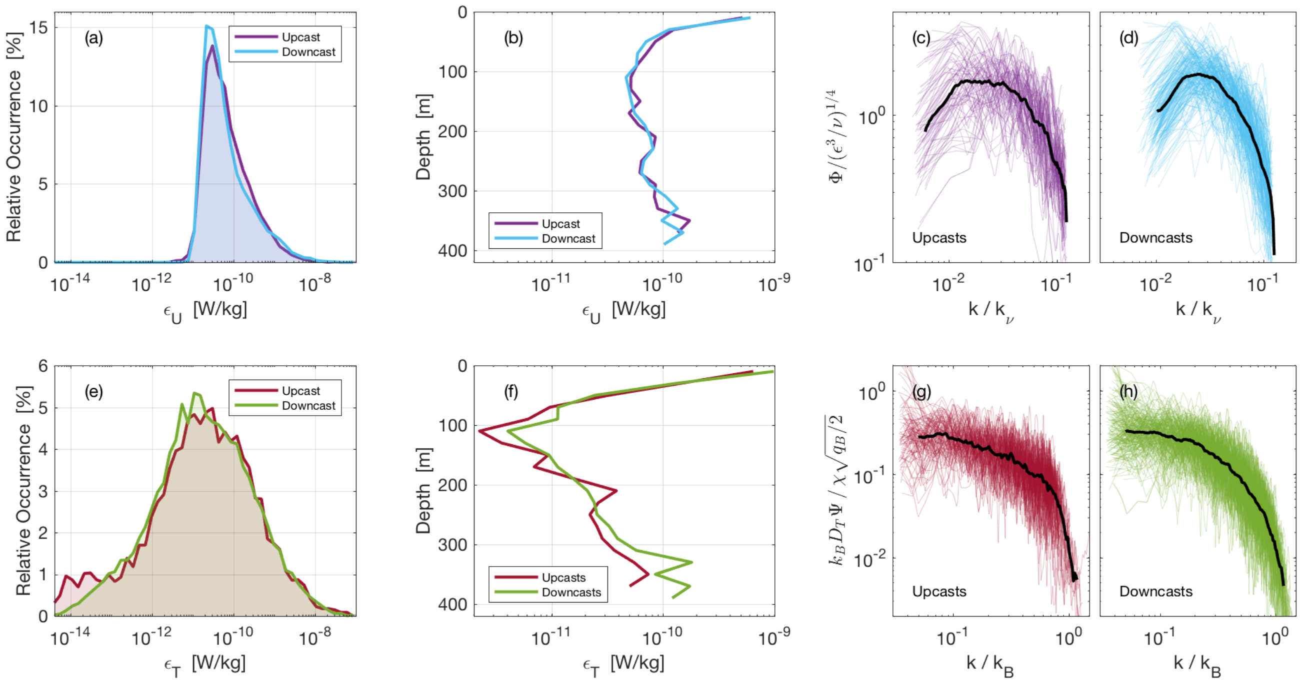

Figure A.2 – Overview of select results, separated by upcast and downcast. For each of ε_U and ε_T, we show the histograms (a,e), averaged vertical profiles (b,f), and selected spectra (c–d,g–h) separated in this manner. The spectra shown are those corresponding to dissipation rates within a factor of 1.1 of 10^{-9} W/kg. Thick black lines depict the median of the selected spectra at each wavenumber.

A.2 Comparison of Results from Upcasts and Downcasts

The stratification conditions in the Amundsen Gulf resulted in much faster glider speeds on upcasts than on downcasts (Table 2.1). Because dissipation rate calculations are very sensitive to the estimated glider speed $\mathcal{U}$ (Osborn and Crawford, 1980; Gregg, 1999; Lueck, 2016), this discrepancy can be leveraged to further inform our confidence in the measurements and data processing methods. In the absence of systematic errors in the data processing, we would expect to see no systematic difference in the results derived separately from upcasts and downcasts despite the nearly factor of 2 difference in $\mathcal{U}$.

We observe little to no difference between dissipation rate estimates when the results are separated by upcast and downcast. Figure A.2 presents an overview of the ε_U and ε_T results separated in this manner. The two histograms of ε_U (panel a) have nearly indistinguishable characteristics: for example, the medians are 5×10^{-11} W/kg and 4×10^{-11} W/kg for up- and downcasts respectively, and the respective geometric standard deviation factors are 3.5 and 3.7. Similarly, the two averaged vertical profiles of ε_U (panel b) are nearly identical in magnitude everywhere; they typically agree within a factor of 1.2 and always within a factor of 1.8. Shear spectra are likewise similar between up- and downcasts, as highlighted in the selected spectra shown in panels (c,d). Median spectra are generally alike in shape with a marginally wider spectral peak for the upcast median spectrum.

There is slightly more discrepancy between up- and downcasts in the ε_T results, though the overall agreement is still encouraging and the discrepancy does not impact the results or conclusions of the study. The histogram comparison (panel e) is generally favourable: the median is 2×10^{-11} W/kg for both distributions, and the geometric standard deviation factors are 23.4 and 16.2 for upcasts and downcasts respectively. The upcast distribution is wider because of a small unexpected increase in the number of ε_T values below 1×10^{-13} W/kg. As discussed in Section 2.5.2, there is extensive uncertainty associated with values of ε_T smaller than 2×10^{-12} W/kg, and so it is unclear how much meaning can be assigned to this feature of the distribution. The mean profiles (panel f) demonstrate adequate agreement, typically within a factor of 2 and always within a factor of 3.5, in line with typical uncertainties from microstructure measurements. The shape of the two median temperature gradient spectra (panels g,h) compare favourably with only a slightly less rounded rolloff to the Batchelor scale for the upcast spectrum.

A.3 Nasmyth and Batchelor Spectra

The Nasmyth spectrum, Φ_N, is an empirically derived form for the one-dimensional power spectrum of velocity shear in an unstratified turbulent flow and is based on measurements collected in a strongly turbulent tidal channel in coastal British Columbia (Nasmyth, 1970). It describes both the inertial subrange of the shear spectrum, predicted by Kolmogorov (1941), and the viscous subrange where viscosity begins to influence the motion of turbulent eddies. The results of Nasmyth were tabulated by Oakey (1982), and a mathematical fit was later proposed by Wolk et al. (2002). We use a modified form of that expression, described by Lueck (2016), which can be written nondimensionally as $\Phi_N^* = 8.05\widetilde{k}^{1/3} / \left(1 + (20.6\widetilde{k})^{3.715}\right)$, where $\widetilde{k} = k(\nu^3/\varepsilon)^{1/4}$ and the spectrum is nondimensionalized using $\Phi_N^* = \Phi_N / (\varepsilon_U^3/\nu)^{1/4}$.

The Batchelor spectrum is a theoretical one-dimensional power spectrum describing the wavenumber distribution of a passive tracer's gradients in an unstratified turbulent flow (Batchelor, 1959); its integral is proportional to the rate, χ, at which the tracer gradients are smoothed by molecular diffusion. The spectrum is an analytic solution to the advection-diffusion equation driven by turbulent strain and the large-scale tracer gradient. In one dimension, it may be written as:

$$\Psi_\mathrm{B} = \frac{\chi\sqrt{q_B/2}}{k_B\,\kappa_T^\mathrm{mol}}\left(a\exp\left(\frac{a^2}{2}\right) - a^2\sqrt{\frac{\pi}{2}}\,\mathrm{erfc}\left(\frac{a}{\sqrt{2}}\right)\right) \tag{A.1}$$

where

$$a = (k/k_B)\sqrt{2q_B}\,. \tag{A.2}$$

The factor q_B is a dimensionless constant related to the average least principal rate of strain; it represents the timescale by which compressive strain sharpens scalar gradients (Smyth, 1999). The value of q_B is uncertain, and experiments by Oakey (1982) suggest the range 2.2–5.2, though typically $q_B = 3.4$ (e.g. Ruddick et al., 2000) or $q_B = 3.7$ (e.g. Peterson and Fer, 2014) are used. A percentage error in q_B is expected to lead to twice the percentage error in ε_T (Dillon and Caldwell, 1980). We used $q_B = 3.4$ in our analysis but also processed all the temperature measurements using $q_B = 3.7$, and the difference in results was small: using $q_B = 3.7$, we found for ε_T a mode of 1.5×10^{-11} W/kg, a geometric mean of 1.9×10^{-11} W/kg, and a geometric standard deviation factor of 18.3 (compare with Table 2.2).

Note that the Kraichnan spectrum (Kraichnan, 1968) would be an adequate alternative for the fitting procedure described in Section 2.3.3. Peterson and Fer (2014) compared the results of fitting observed temperature gradient spectra to Batchelor and Kraichnan spectra and found no significant difference in the final ε_T results.